A green spark in electronics

Electrochemical innovations for a sustainable printed circuit board industry

Biemolt, J.

Publication date
2021

Document Version
Final published version

A Green Spark in Electronics

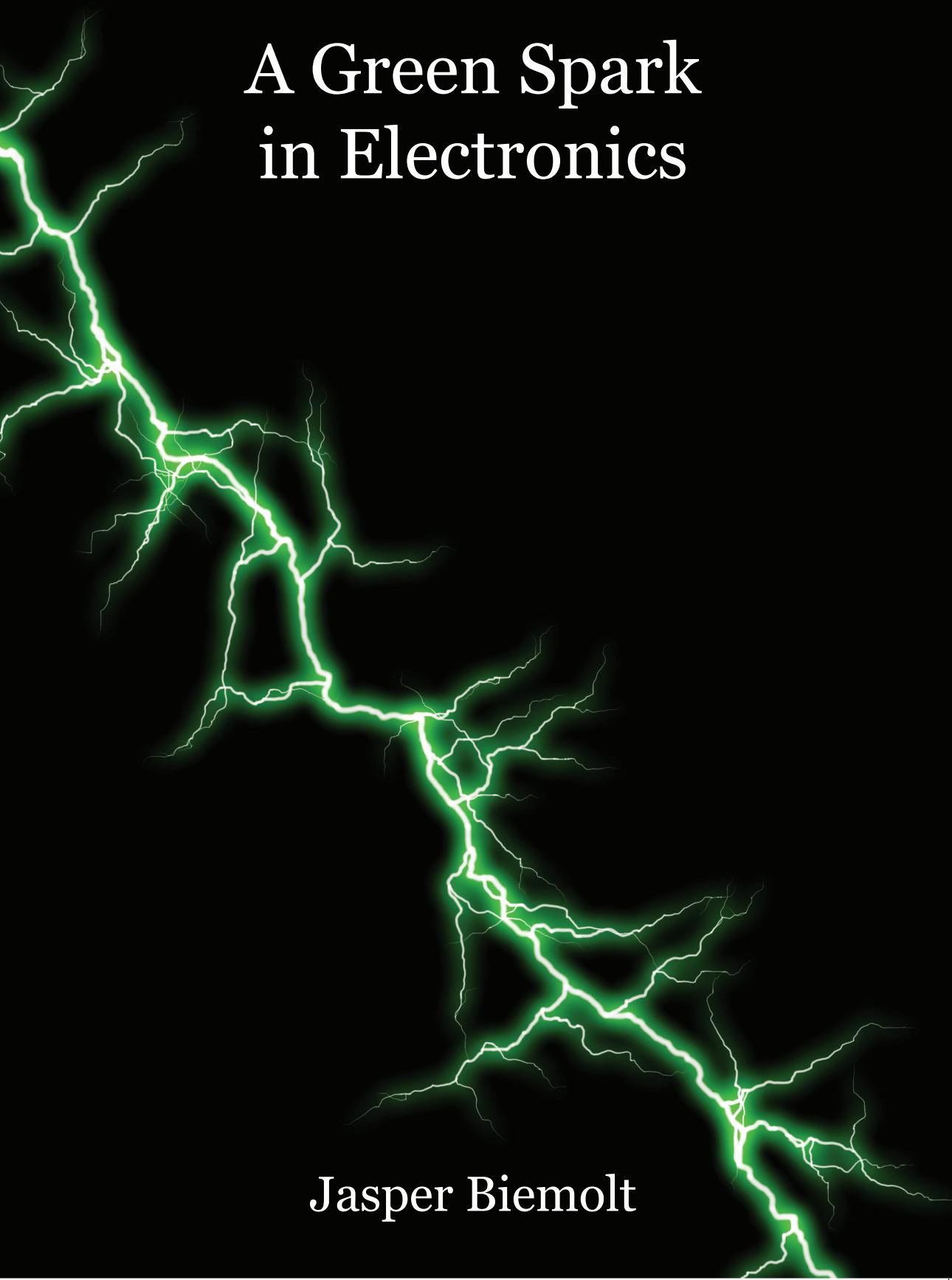

Jasper Biemolt

A Green Spark in Electronics

Electrochemical Innovations for a Sustainable Printed Circuit Board Industry

Cover design	Jasper Biemolt
ISBN	978-94-6421-532-8
Printing	Ipskamp printing
Electronic version	http://dare.uva.nl/

A Green Spark in Electronics

Electrochemical Innovations for a Sustainable Printed Circuit Board Industry

ACADEMISCH PROEFSCHRIFT

ter verkrijgen van de graad van doctor

aan de Universiteit van Amsterdam

op gezag van de rector Magnificus

prof. Dr. Ir. K.I.J. Maex

ten overstaan van een door het College voor Promoties ingestelde commissie

in het openbaar te verdedigen in de Agnietenkapel

op woensdag 1 December 2021, te 16.00 uur

door

Jasper Biemolt

geboren te Almere

Promotiecommissie:

Promotor:	prof. dr. Gadi Rothenberg	Universiteit van Amsterdam
Copromotor:	dr. Ning Yan	Universiteit van Amsterdam

Overige leden:	prof. dr. Bas de Bruin	Universiteit van Amsterdam
	prof. dr. Bob van der Zwaan	Universiteit van Amsterdam
	prof. dr. Jan H. van Maarseveen	Universiteit van Amsterdam
	prof. dr. Sander Woutersen	Universiteit van Amsterdam
	prof. dr. Xian-Zhu Fu	Shenzhen University
	prof. dr. Evgeny Pidko	TU Delft

Faculteit der Natuurwetenschappen, Wiskunde en Informatica

The research presented in this thesis was carried out in the Van 't Hoff Institute for Molecular Sciences of the University of Amsterdam and is part of the Sustainable Chemistry research Priority Area. Financial support was provided by the Netherlands Organization for Scientific Research (NWO) NWO-GDST Advanced Materials program (project No. 729.001.022).

“For me, I am driven by two main philosophies: know more today about the world than I knew yesterday and lessen the suffering of others. You'd be surprised how far that gets you.”

– Neil deGrasse Tyson

Table of Contents

Chapter 1.	The Tools that Define Us and the Need for Sustainability	1
Chapter 2.	Treating Organic Pollutants – Influence of Nitrogen-Doped Carbon Morphology and Surface on ORR	25
Chapter 3.	Treating Organic Pollutants – Electrochemical H2O2 Generation via a Nitrogen-Doped Carbon	57
Chapter 4.	Waste Prevention – a Palladium and Cuprous Oxide Nanocluster Assembly for Electroless Copper Deposition	87
Chapter 5.	An Anion-Exchange Membrane Fuel Cell Containing Only Abundant and Affordable Materials	113
Summary		135
Samenvatting		139
List of publications		145
Author contributions		147
Acknowledgements		149

Chapter 1

The Tools that Define Us and the Need for Sustainability

Humans are defined by complex thinking. This sets us apart from other animals. Some would suggest another difference is the use of tools. Yet both Jane Goodall and Charles Darwin showed tool usages among primates, making this characteristic less special.[1,2] Nor is this behavior limited to primates, as other mammals and corvids show similar abilities.[3,4] Rather, the difference lies in the design and complexity of humanity's tools.

The special place tools hold for humanity is also reflected by our naming of time periods. For example, the bronze age is defined by the development of bronze tools. Similarly, the industrial age saw the rise of complex machinery and mass production. The latter period shifted from biological systems – either our own bodies or animals – to supply work, to physics-based mechanical work. Wind, water and steam powered machinery helped mass production and provided consumers with new life altering tools. This revolution was quickly followed by the next step. In the late 19th century, electricity was already discovered, but unlocked its full potential with the invention of the electrical motor. This special resource can produce, besides work, also light and sound. This sparked creativity, with many new inventions such as the lightbulb.

Such a lightbulb also hung in the room where one of the greatest ideas of the 20th century was conceived. This idea determined the next evolutionary step for tools. In 1904, Menlo Park, New Jersey, Thomas Edison and Frank Sprague discussed electrical inventions and their greatest problem. For electrical tools depended on loose wires to transport electricity between components. The more complex the device, the more components and the bigger the mess of wires.[5] Their discussion yielded a simple yet ingenious idea. Instead of **loose** wires, **support** them on a substrate. The idea of conductive graphite/silver tracks adhered on a linen/paper surface, was not pursued further. Between 1926 and 1935 others filed patents on similar ideas, yet none were commercialized.[6]

Paul Eisler, born three years after Edison and Sprague had their discussion, graduated in engineering at the Vienna University of Technology in 1930. After various jobs, he started working at Vorwärts, a social-democratic publisher. Here he saw the printing press, a widespread and mature technology at the time. Inspired, he saw herein the solution to the wire problem encountered during his engineering degree. Automating wire printing on a substrate avoids loose wires and is excellent for large scale production. In 1936 he printed a complex circuit on an insulating board, marking the birth of the Printed Circuit Board (PCB). The technology was further matured during WW II.[7]

After 1945, PCBs evolved beyond Eisler's chaotic spaghetti of printed wires into the carefully designed tracks used today. The original wooden substrates were replaced by epoxy resins, also fixing the electrical components in place for a streamlined interior. This reduced the size of many tools developed in the 20th century. For example, the room-sized ENIAC used loose wires, but nowadays, everything possible with the ENIAC is possible on a small computer chip.[8] Similarly, the brick-sized Motorola DynaTAC is much larger than today's smartphones.[9]

PCBs and PCB-based tools are fundamentally connected to our daily lives. We use them on every occasion and even use multiple PCB based tools at the same time (as I type this thesis on my laptop, a mobile phone next to it plays music and a tablet displays a funny video of a talking dog). This makes the market highly profitable, with a value of $65 billion in 2019 (about the same as the GDP of Ghana).[10] The increasing "consumer addiction" also results in a projected compound annual growth of 3.2% between 2020 and 2025.[11] Three key sectors drive this annual growth. Firstly, the communication industry continues its growth and connected rise in PCB demand. More than half the world population is already connected via mobile phones, needing continues replacement. The second drive comes from other consumer electronics, such as household appliances. These increase in complexity, have new device intercommunication (the so-called 'internet of things') and thus require more PCBs. Lastly, similar developments are made in the car industry, with multiple intercommunicating systems. These provide increased safety and convenience, and can be improved further into self-driving cars (even further pushing the need for PCBs).

Making PCBs

A growing market needs a robust production process. The process mirrors the complexity of the PCBs, with carefully designed tracks and multiple layers to overcome limitations working in a 2D plane. The manufacturing process is shown in Figure 1.1 and explained in the following steps.[5]

Step 1: Design. PCBs come in many varieties, with different applications needing different designs. A design is made with efficient space and material usage.

Step 2: Panel cleaning. The non-conductive green epoxy glass panel is cleaned to removes any oil, grease and dust particulates.

Step 3: Copper lamination. A thin foil of copper (35 microns) is laminated on this epoxy glass panel (1.6 mm). Again, organics, particulates and formed oxides/sulfides are cleaned from the surface.

Step 4: Photoresist addition. A photo-active pre-polymer layer is coated on the copper layer.

Step 5: Photo-film application. The negative of the design (step 1) is printed on a translucent plastic sheet and placed on the substrate.

Step 6: UV radiation. UV-light is eradiated and exposed pre-polymer hardens through UV-polymerization, yielding the design as a hardened polymer.

Step 7: Photoresist removal. Unreacted pre-polymer is removed, exposing the undesired copper.

Step 8: Copper removal. Exposed copper is etched away, while the hardened polymer protects the copper underneath.

Step 9: Photopolymer removal. The copper design is uncovered by removing the hardened polymer.

Step 10: Layering and bonding. Complex PCBs need multiple boards to be stacked, with tracks crossing the layers to form a 3D space. Multiple layers – steps 1 to 9 – are stacked and bonded to form a single PCB.

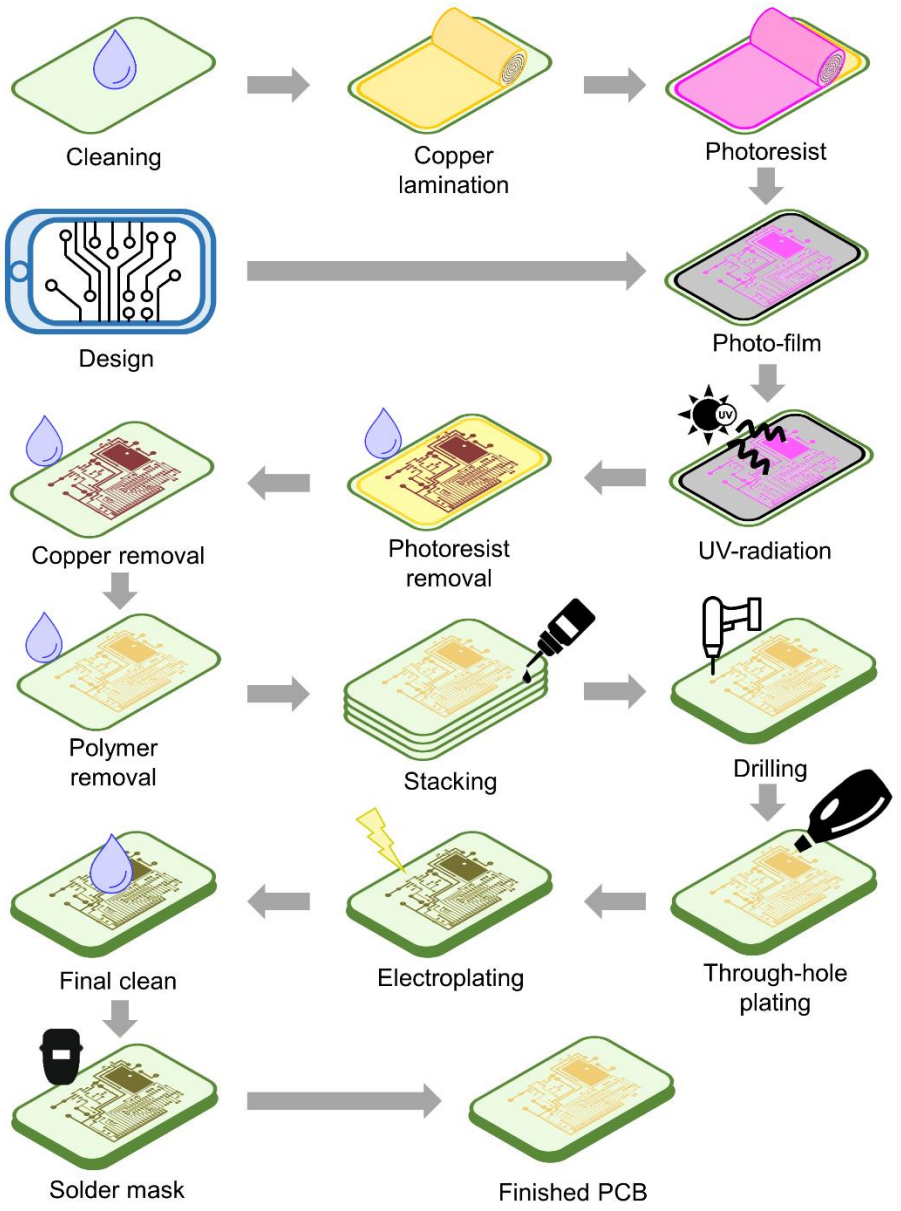

Figure 1.1. *The manufacturing process of a printed circuit board broken down in individual steps.*

Step 11: Drilling. Small holes are drilled for later mounting of the electrical components.

Step 12: Through-hole plating. Copper is chemically plated in the holes (which lack copper) via electroless copper deposition.

Step 13: Final plating. Track quality is improved by additional copper electroplating, with a secondary tin layer to prevent oxidation.

Step 14: Final etching. The tin protects the conductive copper tracks and a final acidic clean is used to remove leftover exposed copper on the PCB.

Step 15: Solder mask. To enhance the soldering of the components, a solder mask is applied.

This robust process already supplies PCBs for decades, but is long and complex. The complexity also hides another problem. A PCB layer starts fully covered with copper (step 3) and ends with only copper tracks (step 9). In theory, this already produces large amounts of copper waste. However, the design transfer is achieved using a polymer layer, with the polymer nor being present in the final product. In short, the process is highly wasteful. Still, this is the preferred method as it is the cheapest method to make high-quality PCBs.

Waste in any form results in pollution and unsustainable behavior and thus must be resolved. For the PCB industry, diminishing the PCB demand by changing people's behavior and cure the PCB addiction is an option. But this halts progress and as scientists, we enable progress not halting it. Consequently, our goal is to minimize the ecological impact of the PCB industry.

At the core this means diminish the amount of waste, which translates in either prevention or treatment. In the latter, pollutants are captured and stored, or converted into 'harmless' products before release in the environment. For prevention, the formation of waste is stopped entirely. Waste prevention is thus the most promising, with waste treatment also involving operating expenditures (OPEX). The OPEX is much lower with waste prevention as raw material is saved (saving production costs). However, waste prevention in the PCB industry requires a complete overhaul of the production process. This requires large capital expenditures (CAPEX) , while waste treatment only require extensions of the existing process (and thus a low CAPEX).

Waste treatment – removing the waste from waste water

Waste treatment is often seen as a necessary evil. No company likes spending money on something other than their final product. It is also a PR nightmare, as unsuccessful waste treatment receives negative attention, while successful treatment gets no attention at all. Even from an environmental point, waste treatment is the inferior option. Still, the high cost of waste prevention is often too high a risk to take. Thus, research into waste treatment is necessary to minimize the environmental impact of the PCB industry.

The first step in successful waste treatment is determining the types of waste coming from the PCB process . Figure 1.2 shows the waste streams connected to every step in PCB manufacturing. Grey steps produce neglectable amounts of waste, yellow steps generate indirect or low-contaminant waste and orange steps generate large amounts of waste. For example, the first cleaning step is yellow since it only removes traces of grease and particulates. Electroplating is shown in yellow, as the waste from the plating bath is an indirect waste stream. The plating bath is multiuse and does not generate waste every single time. Photoresist removal is shown as orange, as every PCB has the large amounts of polymer that is washed away.

Interestingly, the majority of the PCB waste streams is liquid, involving organic or aqueous media with dissolved species. For waste treatment, separating components allow for better treatment. In polluted organic solvents, undissolved species are physically removed (filters or gravimetric), while evaporating the organic solvent leaves the dissolved residue. The organic solvents can be reused (if pure enough), while the solid waste can be treated further, safely disposed of or even recycled. Aqueous systems are much more dangerous and difficult to treat. As the pollutants are soluble in water, they easily enter the ecosystem. Water solubility also enables uptake in cells, yielding a higher change for interrupting biological processes (poisoning). The evaporation strategy is not viable for aqueous systems, due to the high heat capacity of water ($4.18\ J\ g^{-1}\ K^{-1}$). Thus water evaporation requires too much energy for economic and sustainable viability. Thus, treating the dissolved species in the aqueous waste requires a different approach.

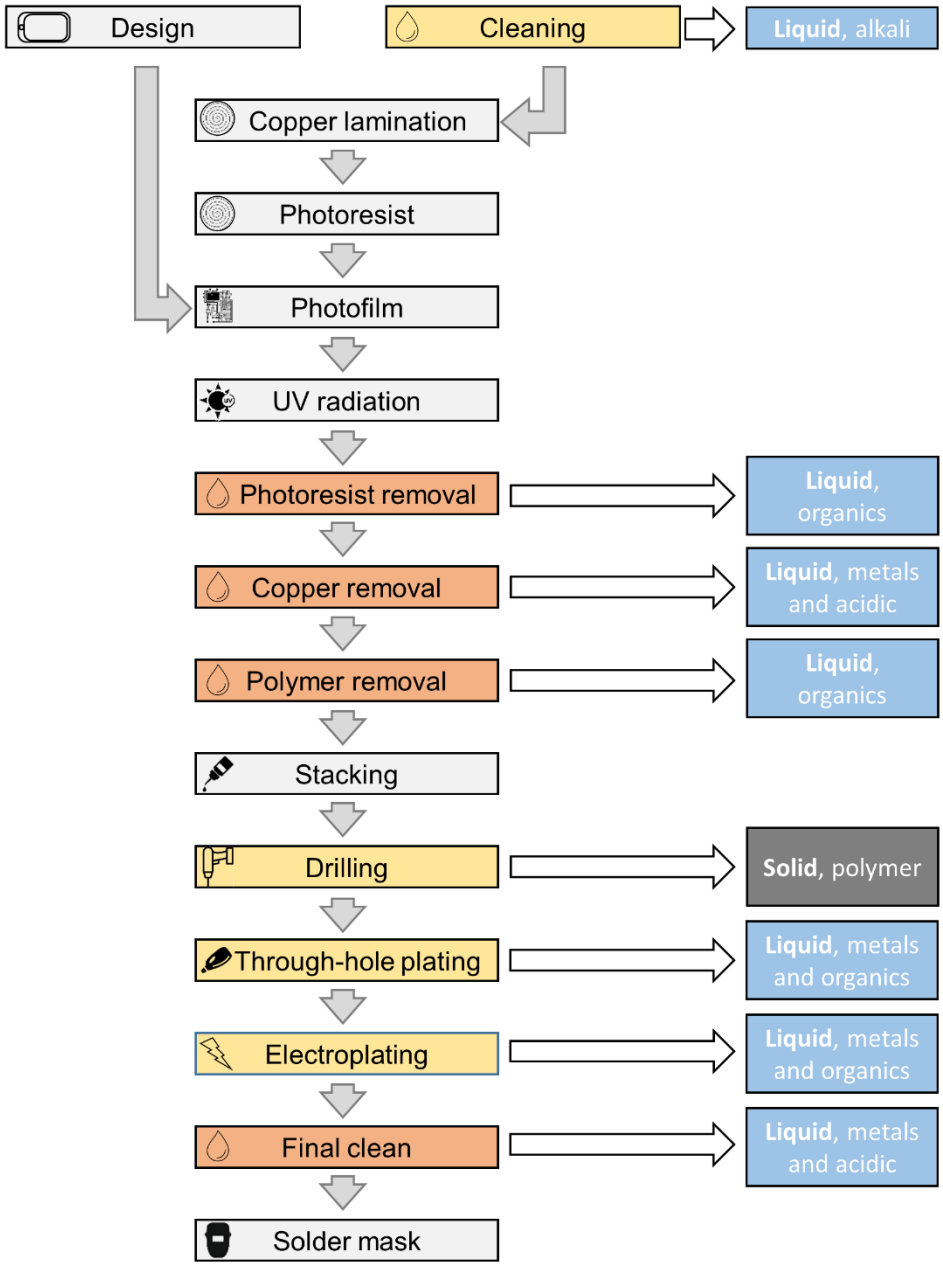

***Figure 1.2**. The waste streams associated with each step of the PCB manufacturing process. In light grey steps without waste, in yellow steps with low or indirect waste and in orange steps with high direct waste.*

There are robust and matured treatment procedures for most dissolved contaminants in aqueous media. For example, acidic waste is simply neutralized by adding lime (CaOH), lye (NaOH) or even limestone ($CaCO_3$).[12] Similarly, alkaline waste is neutralized by adding muriatic acid (HCl). From all contaminants, organic pollutants are an increasingly growing problem. Any untreated organic pollutants have both direct toxicities to and indirect toxicities marine life. As the pollutants are soluble in water, they can easily enter cells and disrupt biological systems (poisoning and direct toxicity). An instance of indirect toxicity is the conversion of pollutants by bacteria, which disrupt the local oxygen balance and pH.[13] Alternatively, dyes can adsorb sunlight, inhibiting plant, algae or bacterial growth.[14,15] The currently treatment uses microorganisms to convert the pollutants into safe products. This method is highly effective and cheap, but only works on biodegradable molecules. Nowadays many synthesized molecules are non-biodegradable as they do not resemble natural molecules.

Thus, the current technique is unsuited for future long-term waste water treatment. Figure 1.3 shows six alternatives for treating organic pollutants. Besides the traditional microorganism treatment, membrane filtration – also referred to as micro- or ultrafiltration – and adsorption are currently used as secondary cleaning methods. These options remove the last remaining low concentrations of pollutants out of the waste water. Implementing these techniques is quite simple and only requires small modifications to existing processes.

In **membrane filtration**, membranes with small enough pores catch the organics, which can be then disposed of as solids.[16] Conditions such as pH and dissolved anions/cations affect the permeation, especially for 'larger' organics, and need to be well controlled during operation. **Adsorption** functions similarly, but traps the organics via either physisorption or chemisorption within the adsorbent.[17] As long as the adsorption is strong (e.g. high adsorption energy) removal efficiencies are high. However, the adsorbent has a maximum adsorption capacity, either needing replacement or reactivation after prolonged use. Especially reactivation can be difficult as you have to overcome the high adsorption energy.

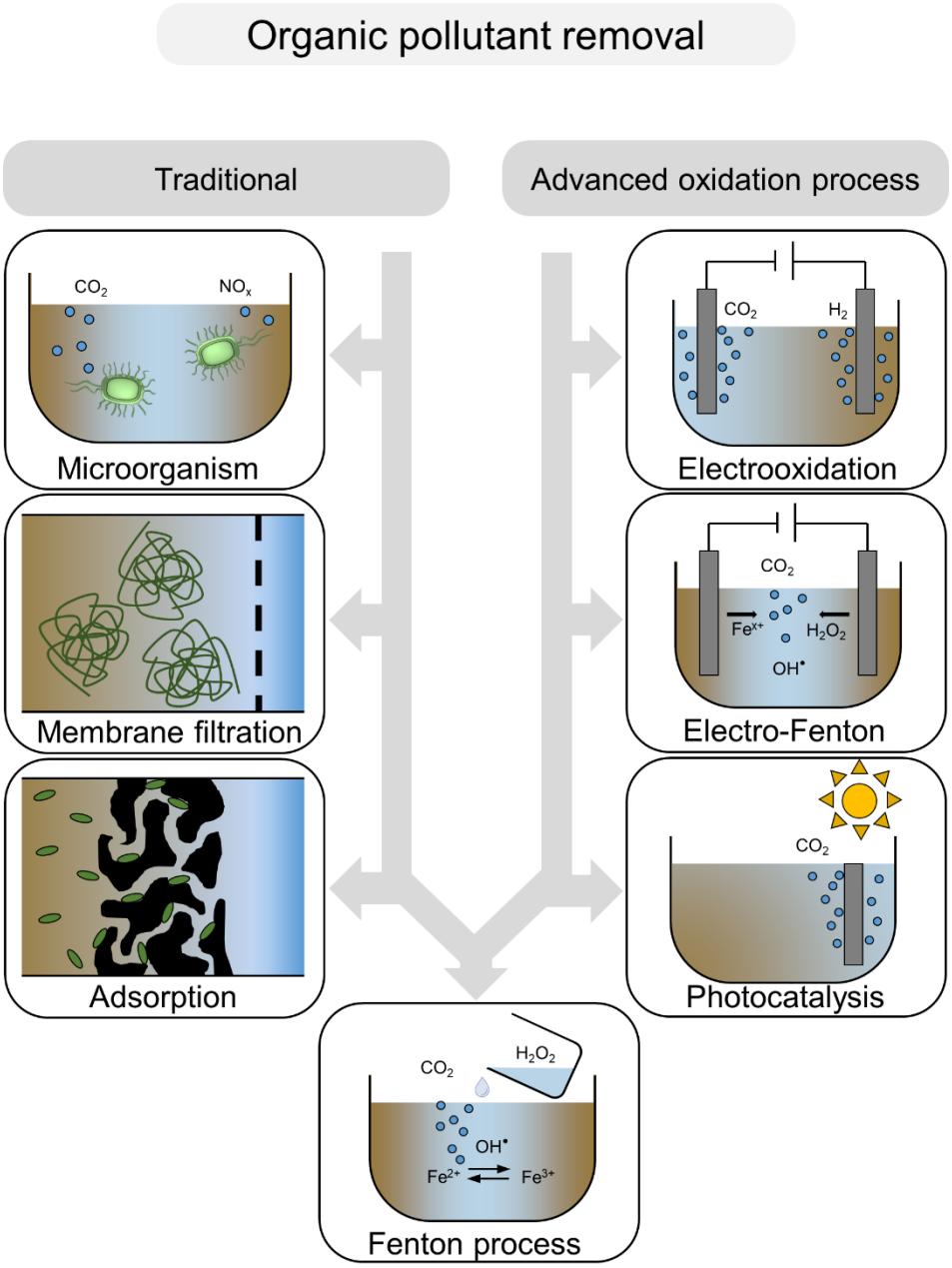

***Figure 1.3**. The different options when treating organics in waste water, divided into either traditional or advanced oxidation. Includes both the use of microorganism, membrane filtration, adsorption, the Fenton process, photocatalysis, the electro-Fenton process and electro-oxidation.*

Both membrane filtration and adsorption do not convert waste, but rather collected. This requires halting the treatment process, collecting the waste and further treatment before disposal or recycling of the solids. For a continuous system, the pollutants must be converted in the aqueous stream. This requires strong oxidizing conditions to mineralize the stable non-biodegradable pollutants into elemental oxides – e.g. CO_2, NO_x, SO_x – which are relatively safe. Most of these oxidizing agents are inherently toxic, shifting, not solving, the problem.

Direct mineralization, without chemical oxidants, is possible through either **electro-oxidation** or **photocatalysis**. Both methods generate a potential either via electricity or sunlight. Reactivity can differ, but for the sake of ease we treat them in this section as similar. In both cases, the energy of the electrons (electric potential) drives the oxidation and thus do not require any additives. They check the boxes regarding sustainability with the share of renewable electricity rapidly increasing and sunlight being an excellent renewable source. The treatment can occur in two distinct ways: either direct or indirect pollutant oxidation.[18–20]

For **direct oxidation**, the potential is directly used to overcome the oxidation energy barrier of the contaminant.[21,22] This varies depending on the chemical structure of the pollutant. Only highly functionalized molecules oxidize at low potentials. More robust pollutants need severely high potentials, which give a high energy cost (high OPEX), limit the stability (lifetime) of the electrodes and is outside the possible potential range of water. Another problem is that partial mineralization can poison the catalytic surface.[23,24] The scientific challenge (e.g. making an electrode/photocatalyst which oxidizes many different pollutants) is highly interesting, but better options are already available.

Indirect oxidation is more favorable as it occurs via the formation of oxidizing species on the catalyst surface. The technique is non-specific as the potential has to match the generation of the oxidizing species. Without additives the easiest to form oxidizing species is hydroxyl radicals, formed via the partial oxidation of water (eq 1.1). However, the partial water oxidation is in competition with its full oxidation to oxygen (eq 1.2). This competition lowers electrical efficiencies, but catalyst design can shift the selectivity towards hydroxyl radical formation. Other oxidizing species can be electrochemically produced from additives (Cl_2, ClO_4^-), but again safety/environmental impact during disposal of these is questionable.

$$* + H_2O \rightarrow H^+ + * OH^{\cdot} + e^- \quad (1.1)$$

$$2H_2O \rightarrow O_2 + 4e^- + H^+ \quad (1.2)$$

Since the controlled partial oxidation of water is difficult, other sources of hydroxyl radicals are required. Their instability make *ex situ* formation and transporting nearly impossible. Hydroxyl radicals must be generated *in situ*, similar to the indirect oxidation method. Another *in situ* approach is their generation through the **Fenton process**.[25,26] Hydroxide radicals (eq 1.3) and hydroperoxyl radicals (eq 1.4) are produced from hydrogen peroxide with iron catalysis, but this catalytic cycle is broken due to the slow kinetics of eq 1.4. Thus, a continuous addition of Fe^{2+} into the treatment stream is required.

$$Fe^{2+} + H_2O_2 \rightarrow Fe^{3+} + OH^- + OH^{\cdot} \quad (1.3)$$

$$Fe^{3+} + H_2O_2 \rightarrow Fe^{2+} + H^+ + OOH^{\cdot} \quad (1.4)$$

Hydroxide and hydroperoxyl radicals are strong enough to decompose many organic pollutants.[27] However, hydrogen peroxide has some sustainability issues. The anthraquinone process used for its synthesis is energy intensive and produces large quantities of waste by itself. Furthermore, the process is only economically viable at the immense annual production rate of 40,000 to 330,00 ton.[28] Thus, transportation to the treatment site (which generates pollution) is a huge problem for the Fenton process. The favorable aspect here is that the Fenton process only requires engineering for optimization (no exotic catalysts or materials development).

Alternatively, *in situ* hydrogen peroxide production through electrochemistry is a sustainable option. Oxygen is reduced via the oxygen reduction reaction (ORR) into hydrogen peroxide (eq 1.5), with electrons being supplied by a sacrificial iron electrode. This iron electrode slowly releases iron cations (eq 1.6), the iron catalyst required for the Fenton process. This **electro-Fenton process** is highly effective and can be altered to operate according to different needs.[29–31]

Periodically replacing the sacrificial electrode hinders a continuous process. Alternatively, electrons can be supplied via the hydrogen oxidation reaction (HOR) (eq 1.7), while the iron catalyst is continuously fed into the waste stream. This does require a continuous supply of hydrogen (but does supply energy as a type of fuel cell). Electrons can also be supplied via the oxygen

evolution reaction (eq 1.2). This yields a process similar to an electrolyzer, only needing an electrical and iron catalyst input. Thus, the electro-Fenton based systems can be tailored to local supply and demand.

$$O_2 + 2H^+ + 2e^- \rightarrow H_2O_2 \quad (1.5)$$

$$Fe^0 \rightarrow Fe^{2+} + 2e^- \quad \text{or} \quad Fe^0 \rightarrow Fe^{3+} + 3e^- \quad (1.6)$$

$$H_2 \rightarrow 2e^- + 2H^+ \quad (1.7)$$

Still, every configuration needs a hydrogen peroxide selective ORR electrode. This is difficult as there is a competition between the two ORR products, water or hydrogen peroxide. Hydrogen peroxide is produced via a $2e^-$ pathway (eq 1.8 & 1.9 for acidic & alkaline conditions), requiring a theoretical potential of 0.7 V vs RHE. Water is produced via the $4e^-$ pathway (eq 1.10 for acidic & 1.11 for alkaline conditions) with a theoretical potential of 1.23 V vs RHE. The higher reduction potential indicates that water production is the thermodynamically favored reaction.[32,33] Another problem is the ease of further reducing hydrogen peroxide to water ($2e^-$+$2e^-$ pathway, eq 1.12 & 1.13) with a theoretical potential of 1.76 V vs RHE.[34,35]

$$O_2 + 2H^+ + 2e^- \rightarrow H_2O_2 \qquad E^0 = 0.7\ V_{RHE} \quad (1.8)$$

$$O_2 + 2H_2O + 2e^- \rightarrow H_2O_2 + 2OH^- \quad (1.9)$$

$$O_2 + 4H^+ + 4e^- \rightarrow 2H_2O \qquad E^0 = 1.23\ V_{RHE} \quad (1.10)$$

$$O_2 + 2H_2O + 4e^- \rightarrow 4OH^- \quad (1.11)$$

$$H_2O_2 + 2H^+ + 2e^- \rightarrow 2H_2O \qquad E^0 = 1.76\ V_{RHE} \quad (1.12)$$

$$H_2O_2 + 2e^- \rightarrow 2OH^- \quad (1.13)$$

The above reactions seem simple, but they comprise of multiple single electron transfer steps. Understanding these steps is the key aspect to design ORR electrocatalysts.[36] ORR is always initiated by the adsorption of O_2, forming the *OOH intermediate (eq 1.14 & 1.15). During the $4e^-$ pathway (towards water), the second electron transfer reduces *OOH further to O* (eq 1.16 & 1.17). Subsequently, *O is reduced to *OH (eq 1.18 & 1.19), which forms either H_2O (eq 1.20, acidic conditions) or OH^- (eq 1.21, alkaline conditions). Alternatively, the *OOH intermediate can also be reduced to hydrogen peroxide via the $2e^-$ pathway (eq 1.22 & 1.23).

Acidic conditions		Alkaline conditions	
$O_2 + * + H^+ + e^- \rightarrow {}^*OOH$	(1.14)	$O_2 + * + H_2O + e^- \rightarrow {}^*OOH + OH^-$	(1.15)
${}^*OOH + H^+ + e^- \rightarrow {}^*O + H_2O$	(1.16)	${}^*OOH + e^- \rightarrow {}^*O + OH^-$	(1.17)
${}^*O + H^+ + e^- \rightarrow {}^*OH$	(1.18)	${}^*O + H_2O + e^- \rightarrow {}^*OH + OH^-$	(1.19)
${}^*OH + H^+ + e^- \rightarrow H_2O + *$	(1.20)	${}^*OH + e^- \rightarrow OH^- + *$	(1.21)
${}^*OOH + H^+ + e^- \rightarrow * + H_2O_2$	(1.22)	${}^*OOH + e^- \rightarrow * + HOO^-$	(1.23)

The key takeaway is that H_2O_2 selectivity stems from the inability to break the O–O bond of the *OOH intermediate. There are two distinct strategies to prevent the O–O cleavage. The first strategy is the optimization of the binding of the *OOH intermediate.[37] Nørskov summarized various theoretical studies, which show that a too strong *OOH either poisons the surface or facilitate O–O bond breaking.[33] A too weak binding of the *OOH yields a high H_2O_2 selectivity, at the cost of a high overpotential and slow electrode kinetics.[38,39] Thus optimizing this binding energy results in fast hydrogen peroxide selective ORR electrodes.

The second strategy to induce hydrogen peroxide selectivity is by geometric control.[40,41] Oxygen binds to the catalytic site in three distinct binding modes, two binding to a monoatomic active site and one bridging two sites.[42] At the monoatomic active site, oxygen can either bind with one oxygen atom via an 'end-on' mode (Pauling type) or with two oxygen atoms via a 'side-on' mode (Griffiths type). Oxygen bridged between two active atoms (Yeager type) always uses both oxygen atoms (all binding modes are depicted on a metal surface in Figure 1.4). The type of bonding is important as binding with both oxygen atoms to the active site (Griffiths and Yeager) inherently gives a higher chance of breaking the O–O bond.[43] There is more interaction with the oxygen molecule and thus more interaction with the antibonding orbitals. This does not mean that Pauling type binding will immediately result in hydrogen peroxide selectivity or Griffiths and Yeager type adsorption only afford water. Having only Pauling type binding statistically increases the chance for hydrogen peroxide selectivity and is thus preferred.

These mechanism and binding considerations are important for hydrogen peroxide selective electrocatalysts and subsequently for waste water treatment via

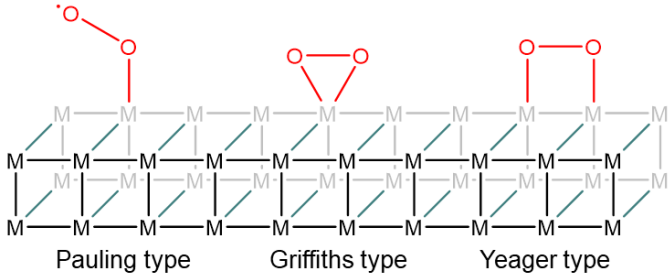

Figure 1.4. *The Pauling, Griffiths and Yeager binding modes of oxygen to a metal surface.*

the electro-Fenton process. We believe that this method is the most viable and sustainable approach for waste water treatment. It converts a large range of pollutants into safe products with a minimal environmental impact. Furthermore, this method is not limited to the PCB industry. A apart of our research will thus focus on the development of hydrogen peroxide selective ORR electrocatalysts.

Waste prevention – The sustainable choice

Waste treatment is a good method to adhere to regulations, but waste prevention is the superior alternative. Unlike waste treatment, it does not drain value from the final product. Contrarily, it saves costs, increases efficiency and is more sustainable. Applying waste reduction in the most wasteful steps is the most effective. In the PCB process, the largest portion of waste comes from producing the copper tracks (steps 3 to 9 in Figure 1.2). This top-down approach, similar to fiddling and sculpting, removes bulk material until the design is formed. The alternative is a bottom-up approach, like pottery and 3D printing, were only desired material is added to the product.

Such an additive method is already used by the PCB industry.[44] Step 12 entails selective chemical copper plating in the holes of the PCB. This electroless copper deposition (ECD) occurs via a plating bath containing both a reducing agent and copper cations. The composition is such that the copper reduction is thermodynamically favourable, but kinetically limited by a high energy barrier.[45,46] This is lowered by an initiator, e.g. it catalyses the oxidation of the reducing agent (eq 1.24). Copper reduction is only possible at the initiator, and

thus initiator placement controls the copper growth. The reaction is also autocatalytic (catalysed by copper), ensuring continuous copper growth even after complete overgrowth of the initial initiator.

$$Cu^{2+} + Red^{n} \rightarrow Cu^{0} + Red^{n+2} \quad (1.24)$$

Implementing this ECD process for making the copper tracks in the PCB manufacturing is straightforward. It replaces steps 3 to 9 with its own steps (shown in Figure 1.5).

Step 3 Initiator solution. Initiator is printed on the epoxy glass substrate, using ink-jet or 3d printing type devices.

Step 4 Rinse. This rinsing step ensures all initiator not adhered to the PCB is removed, enhancing the quality of the PCB.

Step 5 Electroless copper plating. Copper plates on the initiator design from the copper plating bath.

Because the technique is already used, there must be a reason why the industry still uses the top-down method. While satisfactory for the through the hole plating, the ECD process has a three main flaws for growing copper tracks. First, copper adhesion to the surface is not optimal, causing delamination (making the PCB worthless). Secondly, the metastable ECD bath is easily destabilized by contaminants, forming cuprous solids. Lastly, the current initiator is palladium, an expensive and rare element.

Every problem needs to be resolved for economic viability, but changing the initiator is also an interesting catalytic challenge. The plating chemistry dictates the need for the palladium-based initiator. In the traditional alkaline formaldehyde bath, copper salts and formaldehyde are the main components with secondary components such as brighteners, stabilizers, chelating agents. The oxidized to a proton (eq 1.26). However, this last step only occurs on platinum and palladium surfaces. On silver and copper, two adsorbed hydrogen atoms recombine into hydrogen (eq 1.27) without releasing electrons. Any electrons released by the formaldehyde oxidation reduce the copper cations to metallic copper, yielding copper growth.[47–49]

$$H_2C(OH)O^- + OH^- + * \rightarrow HCOO^- + H_2O + {}^*H + e^- \quad (1.25)$$

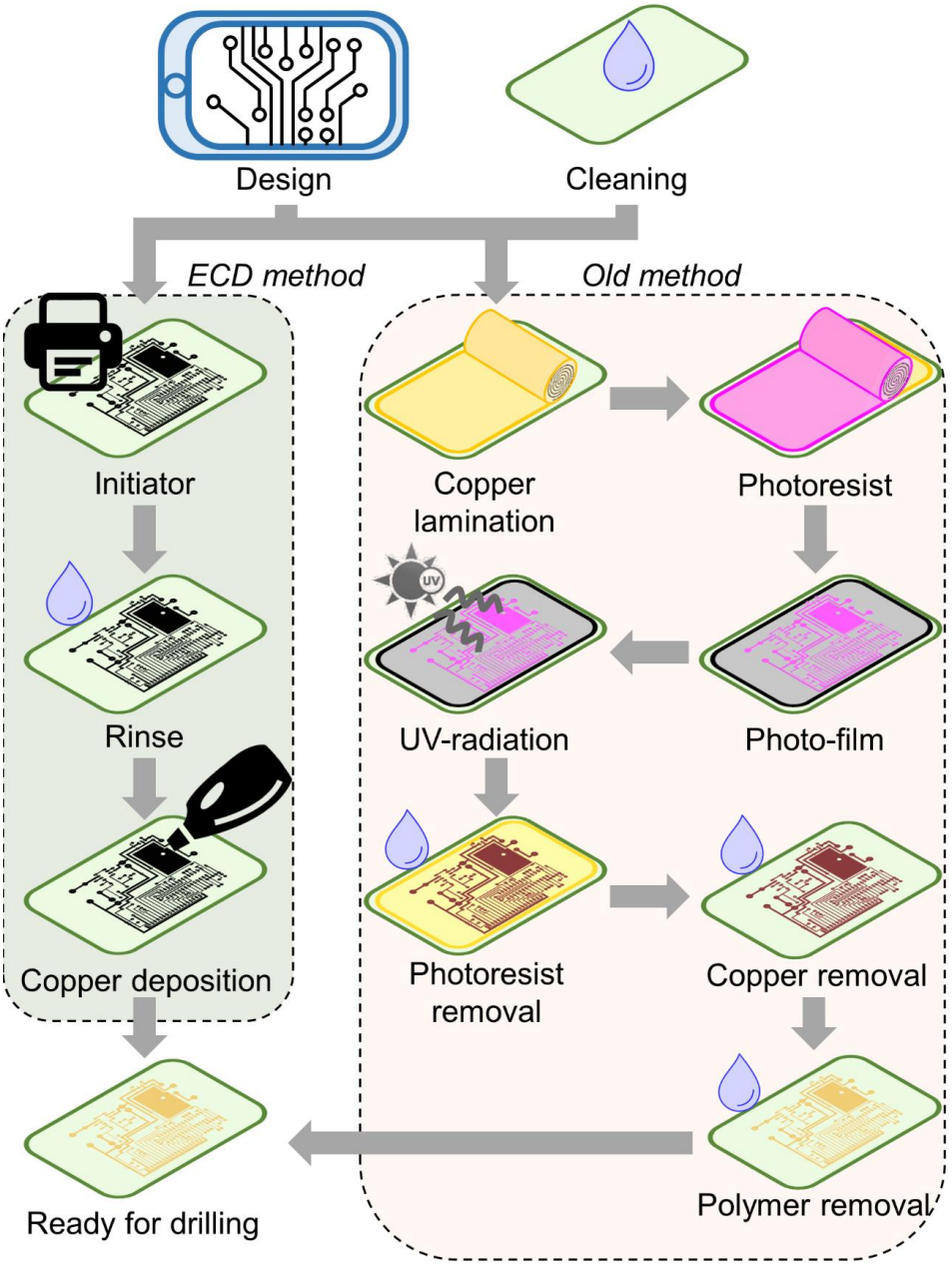

Figure 1.5. *Comparison of the steps for the electroless copper deposition based method and the traditional method for printed circuit boards.*

$$^{*}\mathrm{H} \rightarrow e^{-} + \mathrm{H}^{+} \quad (1.26)$$

$$2\,^{*}\mathrm{H} \rightarrow \mathrm{H}_2 \quad (1.27)$$

An economically viable initiator is achieved by either minimizing the initiator palladium content or replacing palladium completely. Replacing palladium calls for alternative element catalytically active for formaldehyde oxidation. Copper is an alternative as the process is autocatalytic. However, copper is easily oxidized, losing the catalytic activity. Other cheap and abundant options have similar problems.

Replacing palladium still is a viable strategy, but minimizing the initiator palladium content has a higher short-term probability. One option is to minimize expensive metals in catalysts by optimizing their atom efficiency. Nanoparticles have a ratio between the inactive core and active outer surface. Decreasing the particle size shifts the ratio in favour of the active surface. Controlling the nanoparticle size requires excellent understanding of the crystal growth of the nanoparticles. This area is now well understood and new strategies are needed to further improve atom efficiency.

If the core of the nanoparticle is inactive, there is no need to have expensive elements located here. This is where the area of core-shell nanoparticles emerged.[50,51] Making the shell as thin as possible increases the ratio of exposed expensive elements. Another interesting characteristic spawns from the proximity of the active atoms to the interface boundary. Around this boundary the chemical nature of the outer shell changes. Both electronic and geometric effects are responsible for these variations.

The electronic effect (also called ligand effect) occurs from the interaction between electronically different phases.[52–54] The electronic interactions can be visualized as a charge transfer originating from the difference in electronegativity of the two phases.[55] This explanation is heavily simplified, but is acknowledged as one of the components of the ligand effect. The ligand effect is well described in the work of Nørskov on platinum monolayers covering platinum alloys and their ORR activity.[56] In short, oxygen binds too strongly on the platinum surface during ORR. Dissociation of oxygen or hydroxide species from the surface as thus rate limiting. The oxygen binding energy is changed in the alloys of different first row transition metals (Ti to Ni) and platinum with a platinum shell. The electronic interaction between the alloy core and platinum shell decreases the

oxygen binding energy and increases the ORR activity. This is directly correlated to the metal d-band states (electronic surface structures).

The geometric effect stems from the arrangement of crystal structures. Metals have unique crystal lattices, e.g. face-centered cubic (fcc), body-centered cubic (bcc), hexagonal closed packing (hcp),[57] and atomic radii. These differences are important in core-shell structures, because the two crystal phases share a boundary. As they are unique, there is always a mismatch.[58] Imagine footballs stacked into a pyramid and a similar structure made from smaller tennis balls (e.g. same crystal structure, different atomic radii). When building the first half of the pyramid from footballs and the second half out of tennis balls, the task is nearly impossible. There is a mismatch between the two structures. It is possible to make such a two-phase system with tennis balls and golf balls (their sizes are more alike). In this case something interesting happens with the upper layer of golf balls. They will now have more room between them and are a mix between the golf ball and tennis ball pyramid structure. This same expansion or contraction of the crystal lattice also occur in core-shell structures. These geometric or strain effects look minor, but can have heavy implications in catalysis.[59–62]

Synthesizing core-shell structures has two benefits. First, heaving only the expensive elements in the shell and not the core diminishes catalyst cost. Secondly, the strain and ligand effects of the core-shell structures enhance the catalytic activity of the shell beyond the pure metal counterpart. This combination will have a considerable effect on designed ECD catalysts. However, the knowledge obtained about these structures spans more than just the PCB industry. Many catalytic reactions can benefit from tailored core-shell structures, enhancing the catalytic activity, stability and/or selectivity.

Scope of this Thesis

Making waste-free printed circuit boards is difficult. Here we tackle the problem from two different angles. Firstly, we aim to treat the waste generated by the current process. This will be achieved using renewable energy and an electro-Fenton process. Here, organic pollutants – such as polymers and surfactants – are degraded with *in situ* generated hydrogen peroxide. This requires new electrocatalysts that selectively produce hydrogen peroxide, our first focus. Secondly, removing the waste altogether by replacing waste generating steps with

clean alternatives further decreases the environmental impact. This alternative electroless copper deposition, while being less wasteful, requires expensive palladium based catalysts. Thus, our second focus is the development of ECD catalysts that require less palladium.

For the electro-Fenton like process, we envision a hydrogen peroxide selective oxygen reduction reaction (ORR). This is no easy feat and **chapter 2** describes our efforts in understanding the ORR activity of nitrogen-doped carbons. We envisioned that different morphologies and surface groups in the N-doped carbon changes the ORR selectivity. We saw that changes in the morphology and surface functionalities did indeed change the ORR selectivity between the two-electron pathway (towards H_2O_2) and the four-electron pathway (towards H_2O).

However, *in situ* generation of hydrogen peroxide is not enough. To ensure optimal removal, pollutants should be close to hydrogen peroxide generating sites. This is studied in **chapter 3**, taking in consideration the size and adsorption of organic pollutants. As micropores are easily blocked by these species, we prepared a mesoporous N-doped carbon. Mesopores were much better in adsorbing the organic pollutants then micropores, ensuring a close proximity between the pollutants and the hydrogen peroxide generating sites. This excellent combination was not just theoretical, as the N-doped carbon showed the degradation of methylene blue, a model pollutant, during electrocatalysis. Thus, we believe that these carbon-based electrocatalysts are viable candidates for electrochemical waste treatment.

Developing new catalysts for the ECD process is addressed in **chapter 4**. Using the bottom-up ECD approach over the traditional top-down approach diminishes much of the waste. But, as mentioned this requires expensive catalysts. We demonstrated the production of a palladium and cuprous oxide nanocluster assembly, using a simple and green synthesis. This combination results in more active catalysts for the electrochemical reaction required for ECD. Thus, less palladium is needed to achieve the same activity. However, we further showed that these materials are excellent in the oxidation of small organics. This makes them not only ideal for electroless copper depositions, but also for fuel cell/electrolyser applications.

The PCB industry and its pollution are just a small section in the sustainability research field. In **chapter 5**, we broaden our horizon and focus on hydrogen as an energy carrier. In collaboration with the Technion – Israel Institute of Technology, we build an anion-exchange membrane fuel cell based on our N-doped carbon electrocatalyst and their Ni_7Fe/C electrocatalyst. This system – free of any critical raw materials (CRMs) – achieved outstanding cell performance. We believe that CRM-free fuel cells are a viable option for a renewable hydrogen-based future.

References

[1] J. Goodall, Tool-Using and Aimed Throwing in a Community of Free-Living Chimpanzees, *Nature* **1964**, *201*, 1264–1266.

[2] C. Darwin, *The Descent of Man*, D. Appleton And Company, **1871**.

[3] C. Rutz, B. C. Klump, L. Komarczyk, R. Leighton, J. Kramer, S. Wischnewski, S. Sugasawa, M. B. Morrissey, R. James, J. J. H. St Clair, R. A. Switzer, B. M. Masuda, Discovery of species-wide tool use in the Hawaiian crow, *Nature* **2016**, *537*, 403–407.

[4] C. P. van Schaik, E. A. Fox, A. F. Sitompul, Manufacture and use of tools in wild Sumatran orangutans, *Naturwissenschaften* **1996**, *83*, 186–188.

[5] R. S. Khandpur, *Printed Circuit Boards: Design, Fabrication, Assembly and Testing*, Tata McGraw-Hill Education, **2005**.

[6] C. Ducas, *Electrical Apparatus and Method of Manufacturing the Same*, **1925**, US1563731A.

[7] P. Eisler, *Manufacture of Electric Circuit Components*, **1948**, US2441960A.

[8] J. Van der Spiegel, J. Tau, T. Ala'ilima, L. Ang, The ENIAC: history, operation, and reconstruction in VLSI, *First Comput. Hist. Archit.* **2000**, 121–178.

[9] M. Cooper, R. W. Dronsuth, A. J. Leitich, J. C. N. Lynk, J. J. Mikulski, J. F. Mitchell, R. A. Richardson, J. H. Sangster, *Radio Telephone System*, **1975**, US3906166A.

[10] World Bank, "GDP (current US$) - Ghana | Data," can be found under https://data.worldbank.org/indicator/NY.GDP.MKTP.CD?locations=GH, **n.d.**

[11] Mordor Intelligence, Sample - Global Printed Circuit Board Market (2020-2025), **2019**.

[12] M. de Beer, E. H. Mathews, D. Krueger, J. Maree, N. Mbhele, M. Phalanndwa, O. Novhe, Limestone Neutralisation of Arsenic-Rich Effluent from a Gold Mine, *Mine Water Environ.* **2008**, *27*, 46–51.

[13] F. O. Topaç, E. Dindar, S. Uçaroğlu, H. S. Başkaya, Effect of a sulfonated azo dye and sulfanilic acid on nitrogen transformation processes in soil, *J. Hazard. Mater.* **2009**, *170*, 1006–1013.

[14] B. Lellis, C. Z. Fávaro-Polonio, J. A. Pamphile, J. C. Polonio, Effects of textile dyes on health and the environment and bioremediation potential of living organisms, *Biotechnol. Res. Innov.* **2019**, *3*, 275–290.

[15] M. Imran, D. E. Crowley, A. Khalid, S. Hussain, M. W. Mumtaz, M. Arshad, Microbial biotechnology for decolorization of textile wastewaters, *Rev. Environ. Sci. Biotechnol.* **2015**, *14*, 73–92.

[16] B. Van der Bruggen, J. Schaep, D. Wilms, C. Vandecasteele, Influence of molecular size, polarity and charge on the retention of organic molecules by nanofiltration, *J. Membr. Sci.* **1999**, *156*, 29–41.

[17] E. K. Putra, R. Pranowo, J. Sunarso, N. Indraswati, S. Ismadji, Performance of activated carbon and bentonite for adsorption of amoxicillin from wastewater: Mechanisms, isotherms and kinetics, *Water Res.* **2009**, *43*, 2419–2430.

[18] M. Panizza, G. Cerisola, Direct And Mediated Anodic Oxidation of Organic Pollutants, *Chem. Rev.* **2009**, *109*, 6541–6569.

[19] C. A. Martínez-Huitle, S. Ferro, Electrochemical oxidation of organic pollutants for the wastewater treatment: direct and indirect processes, *Chem. Soc. Rev.* **2006**, *35*, 1324–1340.

[20] Á. Anglada, A. Urtiaga, I. Ortiz, Contributions of electrochemical oxidation to wastewater treatment: fundamentals and review of applications, *J. Chem. Technol. Biotechnol.* **2009**, *84*, 1747–1755.

[21] M. Mitadera, N. Spataru, A. Fujishima, Electrochemical oxidation of aniline at boron-doped diamond electrodes, *J. Appl. Electrochem.* **2004**, *34*, 249–254.

[22] A. M. Polcaro, A. Vacca, S. Palmas, M. Mascia, Electrochemical treatment of wastewater containing phenolic compounds: oxidation at boron-doped diamond electrodes, *J. Appl. Electrochem.* **2003**, *33*, 885–892.

[23] J. D. Rodgers, W. Jedral, N. J. Bunce, Electrochemical Oxidation of Chlorinated Phenols, *Environ. Sci. Technol.* **1999**, *33*, 1453–1457.

[24] M. Gattrell, D. W. Kirk, A Study of the Oxidation of Phenol at Platinum and Preoxidized Platinum Surfaces, *J. Electrochem. Soc.* **1993**, *140*, 1534.

[25] H. J. H. Fenton, LXXIII.—Oxidation of tartaric acid in presence of iron, *J Chem Soc Trans* **1894**, *65*, 899–910.

[26] F. Haber, J. Weiss, The catalytic decomposition of hydrogen peroxide by iron salts, *Proc. R. Soc. Lond. Ser. - Math. Phys. Sci.* **1934**, *147*, 332–351.

[27] J. L. WANG, L. J. XU, Advanced Oxidation Processes for Wastewater Treatment: Formation of Hydroxyl Radical and Application, *Crit. Rev. Environ. Sci. Technol.* **2012**, *42*, 251–325.

[28] A. Vandenbussche, P. M. Dhaese, S. Bloomfield, F. Janssens, *Process for Producing Hydrogen Peroxide*, **2017**, US9617153B2.

[29] S. O. Ganiyu, M. Zhou, C. A. Martínez-Huitle, Heterogeneous electro-Fenton and photoelectro-Fenton processes: A critical review of fundamental principles and application for water/wastewater treatment, *Appl. Catal. B Environ.* **2018**, *235*, 103–129.

[30] P. V. Nidheesh, R. Gandhimathi, Trends in electro-Fenton process for water and wastewater treatment: An overview, *Desalination* **2012**, *299*, 1–15.

[31] V. Poza-Nogueiras, E. Rosales, M. Pazos, M. Á. Sanromán, Current advances and trends in electro-Fenton process using heterogeneous catalysts – A review, *Chemosphere* **2018**, *201*, 399–416.

[32] S. Fukuzumi, Y.-M. Lee, W. Nam, Mechanisms of Two-Electron versus Four-Electron Reduction of Dioxygen Catalyzed by Earth-Abundant Metal Complexes, *ChemCatChem* **2018**, *10*, 9–28.

[33] A. Kulkarni, S. Siahrostami, A. Patel, J. K. Nørskov, Understanding Catalytic Activity Trends in the Oxygen Reduction Reaction, *Chem. Rev.* **2018**, *118*, 2302–2312.

[34] I. Katsounaros, W. B. Schneider, J. C. Meier, U. Benedikt, P. U. Biedermann, A. A. Auer, K. J. J. Mayrhofer, Hydrogen peroxide electrochemistry on platinum: towards understanding the oxygen reduction reaction mechanism, *Phys. Chem. Chem. Phys.* **2012**, *14*, 7384.

[35] G.-L. Chai, Z. Hou, T. Ikeda, K. Terakura, Two-Electron Oxygen Reduction on Carbon Materials Catalysts: Mechanisms and Active Sites, *J. Phys. Chem. C* **2017**, *121*, 14524–14533.

[36] H. A. Hansen, V. Viswanathan, J. K. Nørskov, Unifying Kinetic and Thermodynamic Analysis of 2 e– and 4 e– Reduction of Oxygen on Metal Surfaces, *J. Phys. Chem. C* **2014**, *118*, 6706–6718.

[37] K. Zhao, Y. Su, X. Quan, Y. Liu, S. Chen, H. Yu, Enhanced H2O2 production by selective electrochemical reduction of O2 on fluorine-doped hierarchically porous carbon, *J. Catal.* **2018**, *357*, 118–126.

[38] D. Mei, Z. D. He, Y. L. Zheng, D. C. Jiang, Y.-X. Chen, Mechanistic and kinetic implications on the ORR on a Au(100) electrode: pH, temperature and H–D kinetic isotope effects, *Phys. Chem. Chem. Phys.* **2014**, *16*, 13762–13773.

[39] A. Verdaguer-Casadevall, D. Deiana, M. Karamad, S. Siahrostami, P. Malacrida, T. W. Hansen, J. Rossmeisl, I. Chorkendorff, I. E. L. Stephens, Trends in the Electrochemical Synthesis of H_2O_2: Enhancing Activity and Selectivity by Electrocatalytic Site Engineering, *Nano Lett.* **2014**, *14*, 1603–1608.

[40] C. H. Choi, H. C. Kwon, S. Yook, H. Shin, H. Kim, M. Choi, Hydrogen Peroxide Synthesis via Enhanced Two-Electron Oxygen Reduction Pathway on Carbon-Coated Pt Surface, *J. Phys. Chem. C* **2014**, *118*, 30063–30070.

[41] X. Xiao, T. Wang, J. Bai, F. Li, T. Ma, Y. Chen, Enhancing the Selectivity of H2O2 Electrogeneration by Steric Hindrance Effect, *ACS Appl. Mater. Interfaces* **2018**, *10*, 42534–42541.

[42] E. Watanabe, H. Ushiyama, K. Yamashita, Theoretical studies on the mechanism of oxygen reduction reaction on clean and O-substituted Ta3N5(100) surfaces, *Catal. Sci. Technol.* **2015**, *5*, 2769–2776.

[43] M. Suk, M. W. Chung, M. H. Han, H.-S. Oh, C. H. Choi, Selective H2O2 production on surface-oxidized metal-nitrogen-carbon electrocatalysts, *Catal. Today* **2019**, DOI 10.1016/j.cattod.2019.05.034.

[44] Y. Shacham-Diamand, V. Dubin, M. Angyal, Electroless copper deposition for ULSI, *Thin Solid Films* **1995**, *262*, 93–103.

[45] S. Ghosh, Electroless copper deposition: A critical review, *Thin Solid Films* **2019**, *669*, 641–658.

[46] I. Ohno, Electrochemistry of electroless plating, *Mater. Sci. Eng. A* **1991**, *146*, 33–49.

[47] G. O. Mallory, J. B. Hajdu, *Electroless Plating: Fundamentals and Applications*, William Andrew, **1990**.

[48] J. Van Den Meerakker, On the mechanism of electroless plating. II. One mechanism for different reductants, *J. Appl. Electrochem.* **1981**, *11*, 395–400.

[49] M. Zhao, L. Yu, R. Akolkar, A. B. Anderson, Mechanism of Electroless Copper Deposition from [CuIIEDTA]2– Complexes Using Aldehyde-Based Reductants, *J. Phys. Chem. C* **2016**, *120*, 24789–24793.

[50] V. R. Calderone, N. R. Shiju, D. Curulla Ferré, A. Rose, J. Thiessen, A. Jess, E. van der Roest, B. V. Wiewel, G. Rothenberg, Applying Topological and Economical Principles in Catalyst Design: New Alumina–Cobalt Core–Shell Catalysts, *Top. Catal.* **2014**, *57*, 1419–1424.

[51] V. R. Calderone, N. R. Shiju, D. Curulla-Ferré, S. Chambrey, A. Khodakov, A. Rose, J. Thiessen, A. Jess, G. Rothenberg, De Novo Design of Nanostructured Iron–Cobalt Fischer–Tropsch Catalysts, *Angew. Chem. Int. Ed.* **2013**, *52*, 4397–4401.

[52] S. Back, Y. Jung, Importance of Ligand Effects Breaking the Scaling Relation for Core–Shell Oxygen Reduction Catalysts, *ChemCatChem* **2017**, *9*, 3173–3179.

[53] J. R. Kitchin, J. K. Nørskov, M. A. Barteau, J. G. Chen, Modification of the surface electronic and chemical properties of Pt(111) by subsurface 3d transition metals, *J. Chem. Phys.* **2004**, *120*, 10240–10246.

[54] T. Bligaard, J. K. Nørskov, Ligand effects in heterogeneous catalysis and electrochemistry, *Electrochimica Acta* **2007**, *52*, 5512–5516.

[55] W. Tang, G. Henkelman, Charge redistribution in core-shell nanoparticles to promote oxygen reduction, *J. Chem. Phys.* **2009**, *130*, 194504.

[56] V. Stamenkovic, B. S. Mun, K. J. J. Mayrhofer, P. N. Ross, N. M. Markovic, J. Rossmeisl, J. Greeley, J. K. Nørskov, Changing the Activity of Electrocatalysts for Oxygen Reduction by Tuning the Surface Electronic Structure, *Angew. Chem. Int. Ed.* **2006**, *45*, 2897–2901.

[57] P. Söderlind, O. Eriksson, B. Johansson, J. M. Wills, A. M. Boring, A unified picture of the crystal structures of metals, *Nature* **1995**, *374*, 524–525.

[58] M. Mavrikakis, B. Hammer, J. K. Nørskov, Effect of Strain on the Reactivity of Metal Surfaces, *Phys. Rev. Lett.* **1998**, *81*, 2819–2822.

[59] P. Moseley, W. A. Curtin, Computational Design of Strain in Core–Shell Nanoparticles for Optimizing Catalytic Activity, *Nano Lett.* **2015**, *15*, 4089–4095.

[60] J. R. Kitchin, J. K. Nørskov, M. A. Barteau, J. G. Chen, Role of Strain and Ligand Effects in the Modification of the Electronic and Chemical Properties of Bimetallic Surfaces, *Phys. Rev. Lett.* **2004**, *93*, 156801.

[61] P. Strasser, S. Koh, T. Anniyev, J. Greeley, K. More, C. Yu, Z. Liu, S. Kaya, D. Nordlund, H. Ogasawara, M. F. Toney, A. Nilsson, Lattice-strain control of the activity in dealloyed core–shell fuel cell catalysts, *Nat. Chem.* **2010**, *2*, 454–460.

[62] M. P. Hyman, J. W. Medlin, Effects of Electronic Structure Modifications on the Adsorption of Oxygen Reduction Reaction Intermediates on Model Pt(111)-Alloy Surfaces, *J. Phys. Chem. C* **2007**, *111*, 17052–17060.

Chapter 2

Treating Organic Pollutants – Influence of Nitrogen-Doped Carbon Morphology and Surface on ORR

Nitrogen-doped carbons are promising candidates for replacing platinum catalysts in fuel cell electrodes. They typically contain graphitic and amorphous domains, both of which contribute to the oxygen reduction reaction (ORR) activity. Here we aim at revealing the catalytic functions of each domain as well of the surface functional groups, and ultimately maximizing the catalytic performance of the materials in ORR. We develop a sequential oxidative-pyrolytic treatment to remove the amorphous domains and to alter surface functionalities. The effectiveness of the approach is evidenced by various techniques. Our electrochemical results show a positive correlation between the ORR activity and the degree of graphitization/oxygen functional group removal. While the oxidation-induced oxygen-containing group impairs the ORR, the amorphous domains facilitate the 2-electron transfer ORR, lack electrical conductivity and are rich in oxygen-containing group. The ORR activity of the optimized sample increases considerably in the alkaline electrolyte, giving a halfwave potential > 0.85 V (vs. reversible hydrogen electrode) that are comparable to those of commercial platinum on carbon.

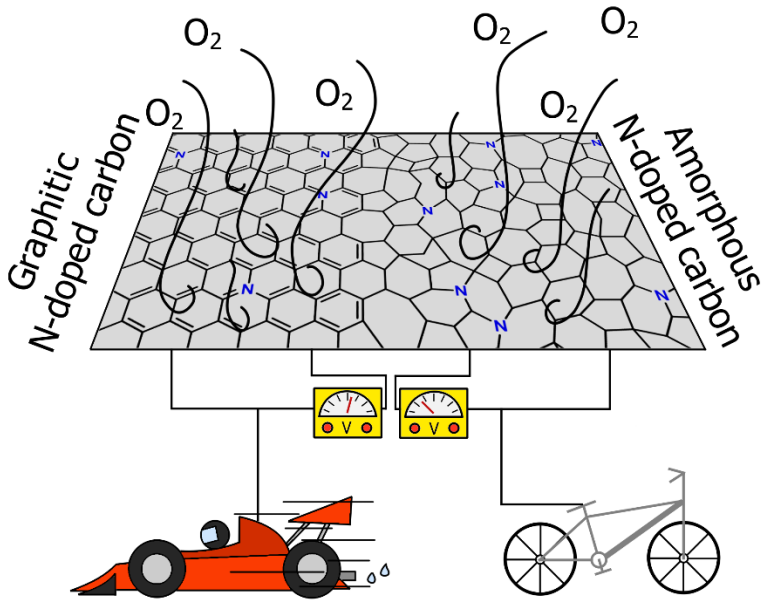

Parts of this chapter have been published as J. Biemolt, G. Rothenberg, N. Yan, Understanding the roles of amorphous domains and oxygen-containing groups of nitrogen-doped carbon in oxygen reduction catalysis: toward superior activity, *Inorg. Chem. Front.* **2020**, *7*, 177–185.

Introduction

Fuel cells are power sources that convert chemical energy into electricity.[1,2] They are much more efficient than internal combustion engines (currently 60% vs 22-45%, respectively).[3] Hydrogen-powered fuel cells have an additional advantage that their only effluent is water vapor (the hydrogen itself must be produced somewhere, but the control of centralized emissions is much simpler). Furthermore, unlike batteries, which carry their entire "fuel" supply within them, fuel cells allows fast refill. All these advantages make fuel cells an attractive part of the sustainable energy economy.

But there is also a catch. The cells must oxidize the fuel on one electrode and reduce the oxygen on the other. This so-called oxygen reduction reaction (ORR) is often a catalytic bottleneck, often requiring platinum containing electrocatalyst.[4,5] At over 24000 US$ per kg, platinum is simply too expensive for large-scale usage. Many ingenious concepts for reducing the Pt in fuel cell electrodes have been published recently,[6–11] but the ideal solution would be avoiding any platinum-group metals entirely. Earlier, we, and others, showed that this can be done using nitrogen-doped carbons (NCs). These materials, which are inexpensive and readily produced and scalable, show good ORR activity and stability.[12–17] Their active sites are ascribed to the pyridinic and graphitic nitrogens.[18–25]

N-doped carbons reported in literature, in many cases, contain both graphitic and amorphous domains. The active sites in these domains might behave differently. Undoubtedly, graphitic domains possess high catalytic performance: using the well-defined graphene substrate, Guo *et al.* demonstrated the significance of pyridinic nitrogen for the ORR activity.[18] Other similar work also showed a positive correlation between pyridinic nitrogen and the ORR performance.[19] However, it is unclear whether the same nitrogen moiety holds comparable ORR activity in the amorphous domains. Indeed, Chen et al. and Cao et al. reported good ORR activity in the disordered amorphous nitrogen-doped carbons.[26,27] Nonetheless, these amorphous carbons also accommodated a relatively large portion of graphitic domains, making it difficult to differentiate the performance between the two domains. In theory, both types of domain have pros and cons: the graphitic domains give high conductivity and contain orderly pyridinic nitrogens as the active site, the vital characteristics for electrocatalysts. In contrast, disordered domains have more intrinsic defects, which generally

function as active sites in catalysis in addition to the N-induced extrinsic defects.[28,29] As a downside, the disorder also generates more labile carbon bonds, which are prone to carbon corrosion.[30–33]

Therefore, we still don't know how the amorphous phase contribute to ORR catalysis, nor the rational approach of optimizing the carbon catalyst in terms of the two domains. Here, starting from a well-characterized series of nitrogen-doped carbons with good ORR activity, we developed a rational and simple approach of selective removal of the amorphous phase and the surface oxygen-containing groups (OCG). Our results show that the new carbon outperforms nearly all the N-doped carbons today and exhibits comparable activity to that of the commercial 20wt% Pt/C in alkaline electrolyte.

Results and Discussion

Nitrogen-doped carbons can be prepared in many ways, from chemical synthesis to biomass pyrolysis.[34–36] Here we emphasize the importance of working with a well-defined system. This is essential if one wants to have reproducible results. We started from our previously reported material, which contains both amorphous and graphitic domains.[37] In a typical synthesis (Figure 2.1a), multi-gram scale samples were prepared by dissolving nitrilotriacetic acid (NTA) and magnesium carbonate in water (see the experimental section for detailed procedures). The precursors contain no ORR-active element such as Fe, Co or Ni, excluding their interference in the reaction.

The fact that this NC has both amorphous and graphitic domains makes it an excellent starting point. We then used a thermal treatment to gradually burn away the amorphous parts (Figure 2.1b). Previous studies on charcoal and graphite showed that amorphous carbon reacts readily with reactive oxygen species, while graphitic carbon reacts much more slowly.[38,39] However, this difference in oxidation kinetics only applies at the right temperature. To pinpoint this temperature, we measured the reactivity of the NC surface with oxygen using temperature programmed oxidation (TPO, see Figure 2.1c). The oxidation profile showed a single peak between 300 °C and 580 °C, in agreement with the results reported for activated carbon.[40] This single peak indicates a fast transition between the amorphous and the graphitic carbon oxidation. That said, the changing slope of the oxidation profile shows that the oxidation kinetics change

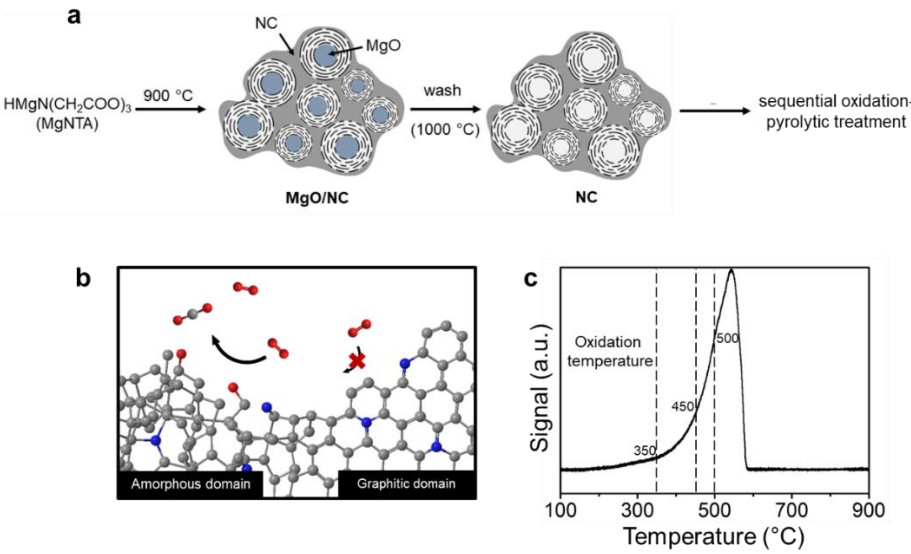

Figure 2.1. *(a) Schematic procedure for synthesizing NC from NTA; (b) Graphic representation of selective oxidation of the amorphous domains over the graphitic domains via the sequential oxidation-pyrolytic treatment. (c) TPO of the pristine NC material, measured from 100 to 900 °C with a ramp rate of 2 °C min⁻¹ and a flow of 2 mL min⁻¹ 5% O_2/He. The dashed lines indicate the temperatures used for the oxidations.*

as the temperature is increased. To understand this behavior, we studied samples treated at different temperatures: 350, 450 and 500 °C (dashed lines in Figure 2.1c). Intuitively, one would imagine that such treatment will also introduce oxygen-containing groups as well surface amorphization. Thus, we also subjected each sample to a pyrolytic treatment in an inert atmosphere at 900 °C to prohibit their possible interference. This cascade oxidative-pyrolytic treatment guaranteed the removal of the amorphous domains while introducing few OCGs.

The effectiveness of this treatment was analyzed with Raman spectroscopy. Generally, this technique is used to monitor the ratio between ordered (G-band at 1580 cm⁻¹) and disordered graphite planes (D-band at 1360 cm⁻¹). Another band for amorphous carbon is located at 1500 cm⁻¹.[41,42] Herein we refer to these three bands as G, D1 and D2, respectively. Figure 2.2a shows the deconvolution of the pristine NC Raman spectrum with the D1, D2 and G bands. Empirically, the decrease of the trough shown by the arrow reflects the ratio decrease of D2. This is supported by the complete deconvolution of a set of Raman spectra in Figure

S1. Therefore, we simply used the depth of this trough as a quicker indicator of the ratio of amorphous carbon in the samples. In general, the ratio between the D1 and G peaks did not change across the set of samples (Figure 2.2b-d, where oxidized samples are denoted as Ox-temp, and pyrolyzed samples as Ox-temp-P). This means that defects in the graphite lattice were hardly introduced or removed by the treatments. The trough did decrease after the treatments, confirming the removal of amorphous carbon. The largest loss in amorphous carbon occurred at 450 °C. Increasing the temperature to 500 °C resulted in the surface oxidation of the graphitic carbon. However, the amount of such oxidation-introduced amorphous carbon decreased after pyrolysis (see the spectrum of Ox-500-P in Figure 2.2d), as expected.

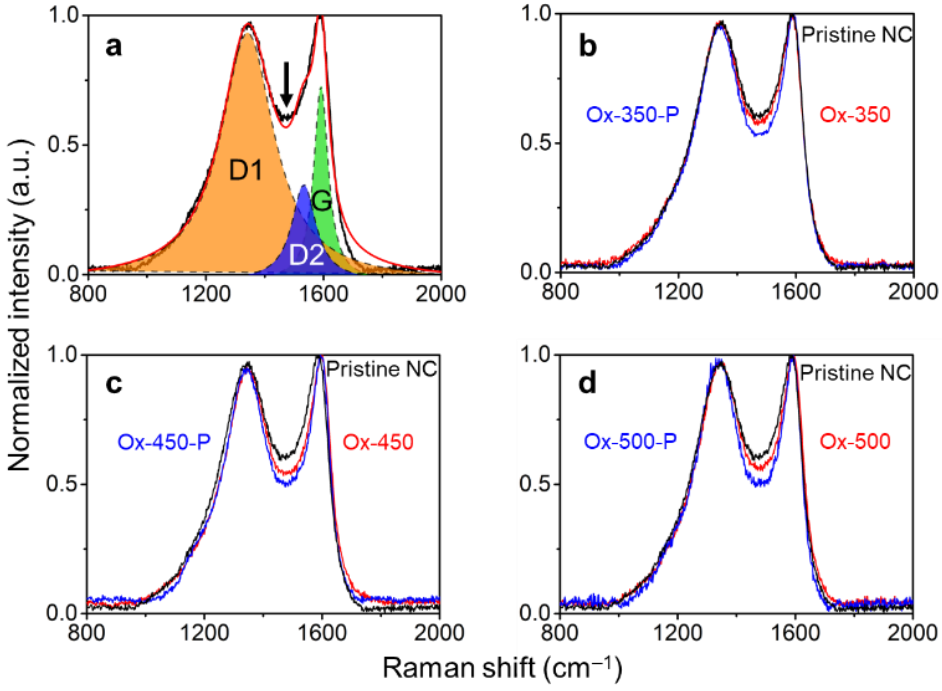

Figure 2.2. *(a) Raman spectra showing curves fitted with the ordered graphitic carbon (G band), disordered graphitic carbon (D1 band), and amorphous carbon (D2 band). The arrow indicates the trough. (b) Raman spectra of the NC samples oxidized at 350 °C. (c) Raman spectra of the NC samples oxidized at 450 °C. (d) Raman spectra of the NC samples oxidized at 500 °C. Oxidized samples are denoted as Ox-temp, and pyrolyzed ones as Ox-temp-P.*

The removal of amorphous carbon hardly changed the morphology of the material. Earlier, we showed that this nitrogen-doped carbon comprised micro-, meso- and macro-pores.[37,43] The relatively low-temperature selective oxidation of amorphous carbon did not significantly alter the porosity of the material. This was confirmed by nitrogen adsorption studies of the oxidized samples (Figure S2.2 and Table S2.1 in the supporting information). The Brunauer-Emmett-Teller (BET) specific surface area (SSA) remained essentially identical after the 350 °C and 450 °C oxidation treatment (~1300 $m^2 g^{-1}$), yet increased to >1700 $m^2 g^{-1}$ at 500 °C. In the meantime, the total pore volume after the oxidative treatment increased slightly, which was attributable to the removal of the hydrogenated carbon layer on the surface, transforming closed-pores into open pores. These changes are even visible in the scanning electron microscopy (SEM) micrographs (Figure 2.3 and Figure S2.3). The surface of the pristine NC is smooth and fully covered carbon layers. The mesopores are hence barely observable (Figure 2.3a). This surface layer was removed after the oxidation, creating large visible mesopores (Figure 2.3b-d). High-resolution transmission electron microscope (HRTEM) measurement was also carried out (see Figure S2.4), the micrographs confirmed that more open pores have formed after the oxidation treatment.

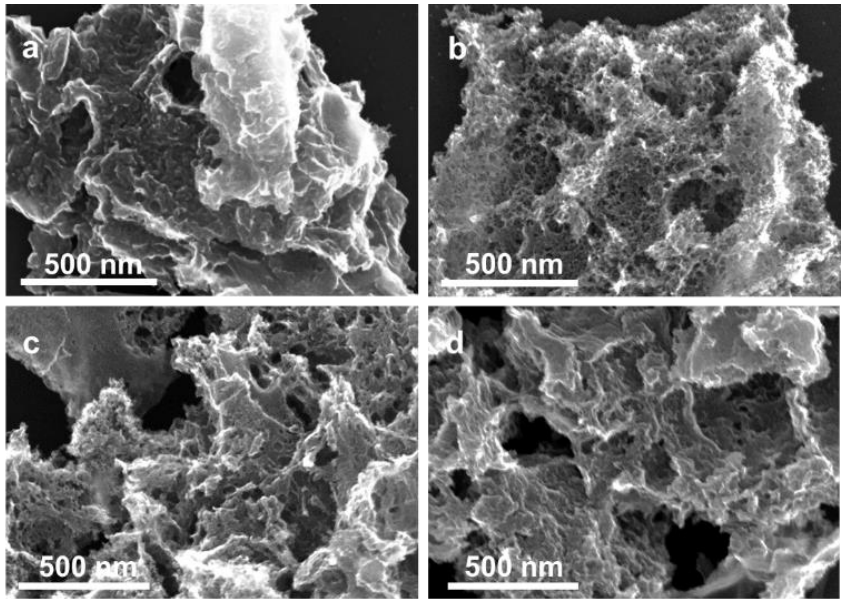

Figure 2.3. *The SEM micrographs of (a) the pristine NC, (b) Ox-350, (c) Ox-450 and (d) Ox-500.*

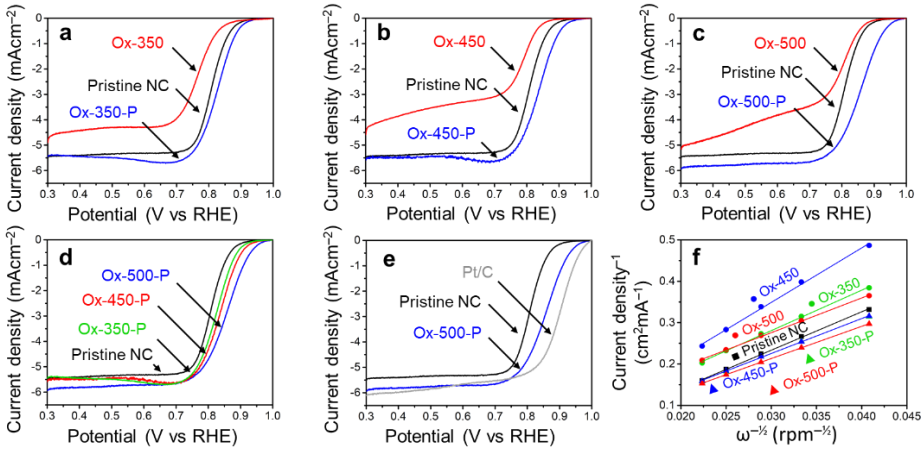

Figure 2.4. *(a) LSV curves of the NCs oxidized at 350 °C. (b) LSV curves of the NCs oxidized at 450 °C. (c) LSV curves of the NCs oxidized at 500 °C. (d) LSV curves of the pyrolysed NCs, showing the trend between ORR activity and oxidation temperature. (e) LSV curves of pristine NCs, Ox-500-P and commercial Pt/C. (f) Koutecký-Levich plots of all the NC samples at 0.5V. All electrochemical experiments were performed in 0.1 M KOH oxygen saturated electrolyte with a scan rate of 10 mV s^{-1} and 1600 rpm.*

We then analyzed the ORR activity of these carbons using the linear sweep voltammetry (LSV, Figure 2.4). These experiments were all done in an oxygen-saturated 0.1 M KOH electrolyte. The measured onset potential (V_{onset}), halfwave potential ($V_{halfwave}$) and electron transfer number (n), derived from the Koutecký-Levich plot,[44] are summarized in Table 2.1. All potentials are reported against the reversible hydrogen electrode (RHE).

As we reported elsewhere,[37] the pristine NC has a high V_{onset} of 0.91 V and $V_{halfwave}$ of 0.81 V (Table 2.1, entry 1). After the oxidation, these values decreased to 0.89 V and 0.76 V for Ox-350 (Figure 2.4a and Table 2.1, entry 2), indicating a negative effect of the oxidation on the ORR activity. This negative effect was even more pronounced for Ox-450 (Figure 2.4b and Table 2.1, entry 4), with a V_{onset} of 0.87 V and $V_{halfwave}$ of 0.79 V. Simultaneously, the selectivity for the 4e– pathway decreased between Ox-350 and Ox-450. However, Ox-500 did not show this trend. The V_{onset} and $V_{halfwave}$ (Figure 2.4c and Table 2.1, entry 6) of this sample were closer to those of pristine NC, as was the $4e^-$ pathway selectivity. After the pyrolysis treatment, a positive correlation between the oxidation temperature and ORR activity was observed (Figure 2.4d). Compared to the pristine NC sample,

Table 2.1. The V_{onset}, $V_{halfwave}$ and electron transfer number (n) for the NC samples

Entry	Sample	V_{onset} (V)[a]	$V_{halfwave}$ (V)	n[b]
1	Pristine NC	0.91	0.81	3.0-3.1
2	Ox-350	0.89	0.76	2.8-3.2
3	Ox-350-P	0.93	0.83	3.3-3.4
4	Ox-450	0.87	0.79	2.5-1.9
5	Ox-450-P	0.94	0.84	3.3-3.4
6	Ox-500	0.89	0.80	3.0-3.5
7	Ox-500-P	0.97	0.85	3.5-3.6
8	Pt/C	0.99	0.90	4[c]

[a] At a faradaic current of 100 μA cm^{-1}. [b] between 0.35 and 0.65 V. [c] Theoretical value.

the V_{onset} increased by 20 mV, 30 mV and 60 mV for Ox-350-P (Table 2.1, entry 3), Ox-450-P (entry 5) and Ox-500-P (entry 7), respectively. A similar effect was seen for the $V_{halfwave}$ and n of these samples. In fact, the ORR activity of Ox-500-P becomes exceptionally high and comes close to the activity of commercial Pt/C (Figure 2.4e and Table 2.1, entry 8), surpassing the state-of-the-art N-doped carbon catalysts in the literature (see the comparison in Table S2.2).

The above results show a positive correlation between the degree of amorphous carbon removal (oxidation temperature) and the ORR activity. Indeed, the low catalytic performance of the amorphous domains can be ascribed to the lack of electrical conductivity and the selectivity to the 2-electron-transfer ORR. However, do the two domains contain rather distinguished type/amount of N moieties? Why simply oxidizing these amorphous domains alone always caused the decrease of the ORR activity? What lead to the performance increase after a subsequent pyrolysis?

A common explanation for the increased ORR activity of NCs is the changes of morphology and SSA. Indeed, the treatments increased both the porosity and SSA, which will affect the ORR activity. However, these properties did not alter for the oxidized and pyrolyzed samples, yet the V_{onset} and $V_{halfwave}$ changed dramatically. Moreover, the electrochemically-active surface area (EASA) only increased for both Ox-350 and Ox-450, and diminished back to similar values as

the pristine NC after the pyrolytic treatment (see the specific capacitance values in Table S2.1). This increase comes from the aromatic OCGs in these samples, increasing the psuedocapacitance of the samples. After the pyrolytic treatment, most of these are removed. Ox-500 also has many OCGs, but the extreme surface roughening and increased aliphatic OCG content diminishes the psuedocapacitance. Since the EASA did not increase after pyrolysis, we argue that the higher ORR activity of these samples is not due to the increased BET surface area.

To understand it, we decided to study further how the oxidation and pyrolysis treatments affect the surface structure. X-ray photoelectron spectroscopy (XPS) showed that the atomic composition of the surface changed after the oxidation treatment (Table 2.2). The pristine NC (entry 1) surface had only 4% oxygen, while this increased to 11% for both Ox-450 (entry 4) and Ox-500 (entry 6). Surprisingly, no change in the oxygen content was observed for Ox-350 (entry 2). According to the previous studies using diffuse reflectance infrared Fourier transform spectroscopy, a carbon with minimal sp^2 characteristics, e.g. amorphous domains, will undergo full gasification during oxidation without generating oxygen functionalities on the surface.[45] We therefore infer that there was a selective gasification of the amorphous domains at 350 °C. At 450 °C and higher temperature, the graphitic domains started to oxidize. But the subsequent pyrolysis removed the oxygen atoms, yielding similar oxygen content values as the pristine NC. The nitrogen content did not change during the oxidation (the

Table 2.2. Surface atomic ratios[a]

Entry	Sample	C Content (%)	N Content (%)	O Content (%)
1	Pristine NC	92.2	4.2	3.5
2	Ox-350	91.2	4.8	4.0
3	Ox-350-P	91.8	3.7	4.4
4	Ox-450	84.7	4.3	11.0
5	Ox-450-P	91.5	3.5	5.0
6	Ox-500	83.5	5.2	11.3
7	Ox-500-P	93.3	4.1	2.7

[a] calculated from the areas of the XPS peaks of C 1*s*, N 1*s* and O 1*s*

fluctuations are attributed to localized heterogeneity in the material). This also reflects the fact that both domains contained similar amount of nitrogen.

While the nitrogen content was unaffected by the treatments, the specific surface groups hardly interchanged either. The different nitrogen moieties, shown in Figure 2.5, were characterized by deconvoluting the N 1*s* XPS peak (see Figure S2.6 in the supporting information). The deconvolution gave four nitrogen peaks: graphitic (398.2 eV), pyrrolic/pyridonic (399.7 eV), pyridinic (401.1 eV) and oxidized nitrogen (403.2 eV). Again, the biggest change in the ratios was observed for Ox-450 (Table 2.3, entry 4) and Ox-500 (entry 6). At these temperatures, the pyridinic nitrogen was oxidized to pyridonic one. This change hardly affected the ORR activity according to the previous studies, e.g., Guo showed that the pyridones, originated from the pyridines, were the intermediates during ORR.[18] The pyrolysis of the oxidized samples converted these groups back to pyridinic nitrogen.

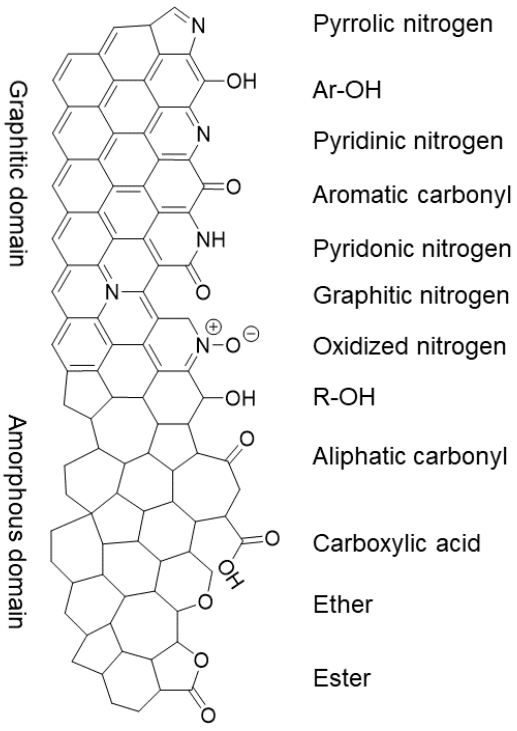

Figure 2.5. *The nitrogen and oxygen functional groups which are expected in the pristine and/or oxidized form of the NC, divided over the graphitic and amorphous carbon domains.*

Since no change in the nitrogen active sites among the samples was detected, the increase in oxygen functionalities was attributable to the drop of ORR activities for the oxidized samples. While OCGs are active in ORR, the activities of each of these species is much lower than that of nitrogen moieties.[46] To prove this, we analyzed the different oxygen functionalities by deconvoluting the O 1*s* XPS peak (Figure S2.7). Quinones, aromatic carbonyls and amides (530.7 eV), aliphatic carbonyls (532.1 eV), alcohols and ethers (532.8 eV), aromatic alcohols and esters (533.6 eV), and carboxyl/adsorbed water (534.9 eV) were used to represent the envelope of the O 1*s* XPS peak.

The main contribution to low oxygen content in the pristine NC came from both aromatic and aliphatic carbonyl groups (Figure 2.6a and Table 2.4, entry 1). A small shift between the ratio of these two functional groups was observed for Ox-350 (entry 2). This resulted from the gasification of the amorphous carbon, increasing the contribution of the aromatic carbonyls/quinones. These groups favor a $2e^-$ ORR pathway and require a higher overpotential compared to nitrogen functionalities.[47,48]

Table 2.3. Distribution of surface nitrogen functionalities[a]

Entry	Sample	Graphitic (%)	Pyridinic (%)	Pyrollic/ pyridonic (%)	Oxidized (%)
1	Pristine NC	1.22 (29.1)	1.65 (39.2)	0.53 (12.6)	0.80 (19.0)
2	Ox-350	1.33 (27.7)	1.81 (37.8)	0.76 (15.8)	0.90 (18.8)
3	Ox-350-P	1.08 (29.3)	1.38 (37.3)	0.53 (14.3)	0.71 (19.1)
4	Ox-450	1.29 (30.0)	1.19 (27.6)	1.02 (23.8)	0.80 (18.6)
5	Ox-450-P	1.05 (30.0)	1.05 (30.0)	0.67 (19.1)	0.73 (20.9)
6	Ox-500	1.55 (29.8)	1.51 (29.0)	1.31 (25.2)	0.83 (16.0)
7	Ox-500-P	1.07 (26.2)	1.32 (32.3)	0.60 (14.7)	1.09 (26.7)

[a] based on the deconvolution of the N 1*s* XPS peaks. The first number represents the absolute percentage of the nitrogen functionality in the sample, while the bracketed number represents the contribution of the functionality to the total amount of nitrogen.

Table 2.4. The distribution of different oxygen functionalities on the NC surface[a]

Entry	Sample	Aromatic carbonyl/ Quinones (%)	Aliphatic carbonyls (%)	R-OH and C-O-C (ethers) (%)	Ar-OH and C-O-C (esters) (%)	adsorbed water (%)
1	Pristine NC	1.33 (38.1)	0.90 (25.6)	0.29 (8.3)	0.31 (8.8)	0.67 (19.3)
2	Ox-350	1.70 (42.5)	0.78 (19.5)	0.43 (10.6)	0.34 (8.6)	0.75 (18.7)
3	Ox-350-P	1.80 (41.0)	1.14 (25.8)	0.38 (8.7)	0.52 (11.7)	0.57 (12.9)
4	Ox-450	5.24 (47.6)	1.97 (17.9)	0.97 (8.9)	1.14 (10.4)	1.67 (15.2)
5	Ox-450-P	2.36 (47.2)	1.17 (23.3)	0.39 (7.9)	0.34 (6.8)	0.74 (14.9)
6	Ox-500	4.47 (39.6)	3.15 (27.9)	0.92 (8.1)	1.16 (10.3)	1.60 (14.2)
7	Ox-500-P	0.77 (28.4)	0.84 (31.1)	0.22 (8.0)	0.32 (12.0)	0.56 (20.6)

[a] based on the deconvolution of the O 1*s* peak in XPS. The first number represents the absolute percentage of the nitrogen functionality in the sample, while the bracketed number represents the contribution of the functionality to the total amount of nitrogen.

Their content increase was reflected by the higher overpotential and low n for Ox-350 (see Figure 2.4a). The oxygen content of Ox-450 and Ox-500 increased drastically, both of which had a significant amount of aromatic carbonyl/quinone functional groups (Figure 2.6b and Table 2.4). These groups were generated by the oxidation of the edges of the graphitic domains. Because of

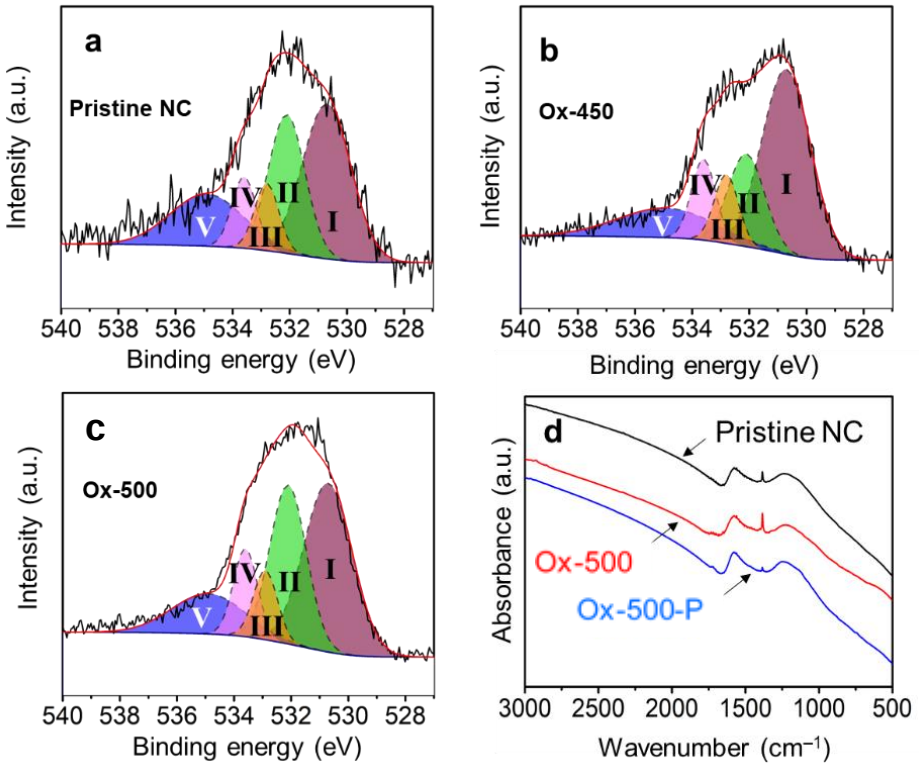

Figure 2.6. *Deconvolution of the O 1s XPS spectra into* ***I*** *aromatic carbonyl/quinone,* ***II*** *aliphatic carbonyl,* ***III*** *R-OH and ethers,* ***IV*** *Ar-OH and esters and* ***IV*** *adsorbed water for (a) pristine NC; (b) Ox-450; (c) Ox-500. (d) The FTIR spectra comparison of pristine NC, Ox-500 and Ox-500-P.*

the high number of quinones, the ORR activity was dominated by the 2e^- pathway.

After pyrolysis, the oxygen content of both Ox-450 and Ox-500 decreased back to the pristine-carbon level (see Tables 2.2 and 2.4). In particular, the aromatic carbonyl/quinone content of Ox-450-P and Ox-500-P dropped pronouncedly. This is also in good agreement with the results of Fourier-transform infrared spectroscopy (FTIR) in Figure 2.6d. The peak at 1380 ± 20 cm-1 was assigned to the stretch vibration of C-H and/or the in-plane bend vibration of C-O, which is linked to the aromatic carbonyl. Its intensity increased substantially after oxidizing pristine carbon at 500 °C. In contrast, the sequential

pyrolysis removed most of them. The lower fraction of the aromatic carbonyl/quinone in Ox-500-P compared to the pristine one also implied the fact that these functionalities were richer in the amorphous domains. Therefore, all the oxidized samples after the pyrolytic treatment showed remarkable ORR activity increase.

Figure 2.7 summarizes the effects of sequential oxidative-pyrolytic treatment on the nitrogen-doped carbon. At 350 °C, only the amorphous domains are gasified, while the graphitic domains remain unaffected. Increasing the temperature to 450 °C starts the oxidation of the graphitic domain edges and introduces oxygen functionalities onto the surface. This effect is amplified at 500 °C, where near complete removal of amorphous carbon removal is expected and the C–C bonds in the graphitic network break, resulting in the surface amorphization in addition to the generation of OCGs. In the electrocatalytic

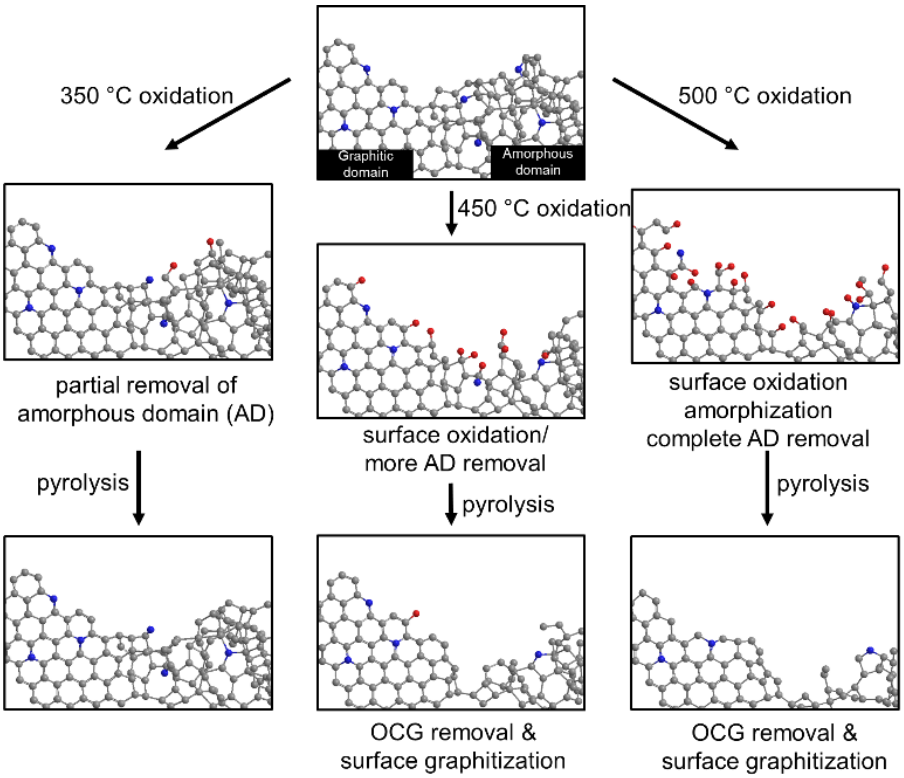

Figure 2.7. *Schematic representation of the effects of the oxidation on the NC at 350 °C, 450 °C and 500 °C, and the subsequent pyrolysis treatment.*

oxygen reduction reaction, a positive correlation between the ORR activity and the degree of graphitization/oxygen functional group removal is observed. We therefore conclude that the amorphous domains and the surface OCGs are unfavored in the ORR catalysis. Rather than lower level of active pyridinic N moiety, such decrease in activity is ascribed to the lower electrical conductivity and the enrichment of in oxygen-containing group. The lower level of amorphous domain also significantly increases the corrosion resistance, contributing to robust electrocatalyst in fuel cells.[29–32]

Conclusions

By simply applying a sequential oxidative-pyrolytic treatment of carbon, we managed to selectively remove the amorphous domains and the surface oxygen-containing groups. Via control experiment, we understand that the graphitic domain in nitrogen-doped carbons is more favoured in the ORR catalysis than amorphous ones. The higher degree of graphitization, high conductivity, less OCGs render superior ORR activity and corrosion resistance of the “upgraded” nitrogen-doped carbon. Since most of the heteroatom-doped carbon materials today contain both domains, our approach and understanding might open new possibilities of optimizing their catalytic performance.

References

[1] R. Schlögl, The Role of Chemistry in the Energy Challenge, *ChemSusChem* **2010**, *3*, 209–222.

[2] S. Chu, Y. Cui, N. Liu, The path towards sustainable energy, *Nat. Mater.* **2017**, *16*, 16–22.

[3] G. W. Crabtree, M. S. Dresselhaus, M. V. Buchanan, The Hydrogen Economy, *Phys. Today* **2004**, *57*, 39–44.

[4] B. Wang, Recent development of non-platinum catalysts for oxygen reduction reaction, *J. Power Sources* **2005**, *152*, 1–15.

[5] D. R. Dekel, Review of cell performance in anion exchange membrane fuel cells, *J. Power Sources* **2018**, *375*, 158–169.

[6] J. Greeley, I. E. L. Stephens, A. S. Bondarenko, T. P. Johansson, H. A. Hansen, T. F. Jaramillo, J. Rossmeisl, I. Chorkendorff, J. K. Nørskov, Alloys of platinum and early transition metals as oxygen reduction electrocatalysts, *Nat. Chem.* **2009**, *1*, 552–556.

[7] L. Bu, S. Guo, X. Zhang, X. Shen, D. Su, G. Lu, X. Zhu, J. Yao, J. Guo, X. Huang, Surface engineering of hierarchical platinum-cobalt nanowires for efficient electrocatalysis, *Nat. Commun.* **2016**, *7*, 11850.

[8] K. Yamamoto, T. Imaoka, W.-J. Chun, O. Enoki, H. Katoh, M. Takenaga, A. Sonoi, Size-specific catalytic activity of platinum clusters enhances oxygen reduction reactions, *Nat. Chem.* **2009**, *1*, 397–402.

[9] S. Yang, J. Kim, Y. J. Tak, A. Soon, H. Lee, Single-Atom Catalyst of Platinum Supported on Titanium Nitride for Selective Electrochemical Reactions, *Angew. Chem. Int. Ed.* **2016**, *55*, 2058–2062.

[10] J. Zhang, M. B. Vukmirovic, Y. Xu, M. Mavrikakis, R. R. Adzic, Controlling the Catalytic Activity of Platinum-Monolayer Electrocatalysts for Oxygen Reduction with Different Substrates, *Angew. Chem. Int. Ed.* **2005**, *44*, 2132–2135.

[11] M. Cao, D. Wu, R. Cao, Recent Advances in the Stabilization of Platinum Electrocatalysts for Fuel-Cell Reactions, *ChemCatChem* **2014**, *6*, 26–45.

[12] M. Zhang, L. Dai, Carbon nanomaterials as metal-free catalysts in next generation fuel cells, *Nano Energy* **2012**, *1*, 514–517.

[13] Z. Chen, D. Higgins, A. Yu, L. Zhang, J. Zhang, A review on non-precious metal electrocatalysts for PEM fuel cells, *Energy Environ. Sci.* **2011**, *4*, 3167.

[14] J. Shui, M. Wang, F. Du, L. Dai, N-doped carbon nanomaterials are durable catalysts for oxygen reduction reaction in acidic fuel cells, *Sci. Adv.* **2015**, *1*, e1400129.

[15] D. Eisenberg, W. Stroek, N. J. Geels, S. Tanase, M. Ferbinteanu, S. J. Teat, P. Mettraux, N. Yan, G. Rothenberg, A rational synthesis of hierarchically porous, N-doped carbon from Mg-based MOFs: understanding the link between nitrogen content and oxygen reduction electrocatalysis, *Phys. Chem. Chem. Phys.* **2016**, *18*, 20778–20783.

[16] D.-S. Yang, S. Chaudhari, K. P. Rajesh, J.-S. Yu, Preparation of Nitrogen-Doped Porous Carbon Nanofibers and the Effect of Porosity, Electrical Conductivity, and Nitrogen Content on Their Oxygen Reduction Performance, *ChemCatChem* **2014**, *6*, 1236–1244.

[17] C. Du, X. Liu, G. Ye, X. Gao, Z. Zhuang, P. Li, D. Xiang, X. Li, A. Z. Clayborne, X. Zhou, W. Chen, Balancing the Micro-Mesoporosity for Activity Maximization of N-Doped Carbonaceous Electrocatalysts for the Oxygen Reduction Reaction, *ChemSusChem* **2019**, *12*, 1017–1025.

[18] D. Guo, R. Shibuya, C. Akiba, S. Saji, T. Kondo, J. Nakamura, Active sites of nitrogen-doped carbon materials for oxygen reduction reaction clarified using model catalysts, *Science* **2016**, *351*, 361–365.

[19] L. Lai, J. R. Potts, D. Zhan, L. Wang, C. K. Poh, C. Tang, H. Gong, Z. Shen, J. Lin, R. S. Ruoff, Exploration of the active center structure of nitrogen-doped graphene-based catalysts for oxygen reduction reaction, *Energy Environ. Sci.* **2012**, *5*, 7936–7942.

[20] C. V. Rao, C. R. Cabrera, Y. Ishikawa, In Search of the Active Site in Nitrogen-Doped Carbon Nanotube Electrodes for the Oxygen Reduction Reaction, *J. Phys. Chem. Lett.* **2010**, *1*, 2622–2627.

[21] H. Kim, K. Lee, S. I. Woo, Y. Jung, On the mechanism of enhanced oxygen reduction reaction in nitrogen-doped graphene nanoribbons, *Phys. Chem. Chem. Phys.* **2011**, *13*, 17505–17510.

[22] Y. Okamoto, First-principles molecular dynamics simulation of O2 reduction on nitrogen-doped carbon, *Appl. Surf. Sci.* **2009**, *256*, 335–341.

[23] L. Yu, X. Pan, X. Cao, P. Hu, X. Bao, Oxygen reduction reaction mechanism on nitrogen-doped graphene: A density functional theory study, *J. Catal.* **2011**, *282*, 183–190.

[24] M. Li, L. Zhang, Q. Xu, J. Niu, Z. Xia, N-doped graphene as catalysts for oxygen reduction and oxygen evolution reactions: Theoretical considerations, *J. Catal.* **2014**, *314*, 66–72.

[25] L. Zhang, Z. Xia, Mechanisms of Oxygen Reduction Reaction on Nitrogen-Doped Graphene for Fuel Cells, *J. Phys. Chem. C* **2011**, *115*, 11170–11176.

[26] J. Chen, X. Wang, X. Cui, G. Yang, W. Zheng, Amorphous carbon enriched with pyridinic nitrogen as an efficient metal-free electrocatalyst for oxygen reduction reaction, *Chem Commun* **2014**, *50*, 557–559.

[27] L. Cao, Z. Lin, J. Huang, X. Yu, X. Wu, B. Zhang, Y. Zhan, F. Xie, W. Zhang, J. Chen, W. Xie, W. Mai, H. Meng, Nitrogen doped amorphous carbon as metal free electrocatalyst for oxygen reduction reaction, *Int. J. Hydrog. Energy* **2017**, *42*, 876–885.

[28] K. Waki, R. A. Wong, H. S. Oktaviano, T. Fujio, T. Nagai, K. Kimoto, K. Yamada, Non-nitrogen doped and non-metal oxygen reduction electrocatalysts based on carbon nanotubes: mechanism and origin of ORR activity, *Energy Environ. Sci.* **2014**, *7*, 1950–1958.

[29] W. Ng, Y. Yang, K. van der Veen, G. Rothenberg, N. Yan, Enhancing the performance of 3D porous N-doped carbon in oxygen reduction reaction and supercapacitor via boosting the meso-macropore interconnectivity using the “exsolved” dual-template, *Carbon* **2018**, *129*, 293–300.

[30] D. von Deak, E. J. Biddinger, U. S. Ozkan, Carbon corrosion characteristics of CNxnanostructures in acidic media and implications for ORR performance, *J. Appl. Electrochem.* **2011**, *41*, 757–763.

[31] P. N. Ross, The Corrosion of Carbon Black Anodes in Alkaline Electrolyte, *J. Electrochem. Soc.* **1988**, *135*, 1464.

[32] L. Li, Y. Xing, Electrochemical durability of carbon nanotubes at 80°C, *J. Power Sources* **2008**, *178*, 75–79.

[33] Y. Shao, G. Yin, J. Zhang, Y. Gao, Comparative investigation of the resistance to electrochemical oxidation of carbon black and carbon nanotubes in aqueous sulfuric acid solution, *Electrochimica Acta* **2006**, *51*, 5853–5857.

[34] Y. Shao, J. Sui, G. Yin, Y. Gao, Nitrogen-doped carbon nanostructures and their composites as catalytic materials for proton exchange membrane fuel cell, *Appl. Catal. B Environ.* **2008**, *79*, 89–99.

[35] Y. Deng, Y. Xie, K. Zou, X. Ji, Review on recent advances in nitrogen-doped carbons: preparations and applications in supercapacitors, *J. Mater. Chem. A* **2016**, *4*, 1144–1173.

[36] H. Wang, T. Maiyalagan, X. Wang, Review on Recent Progress in Nitrogen-Doped Graphene: Synthesis, Characterization, and Its Potential Applications, *ACS Catal.* **2012**, *2*, 781–794.

[37] D. Eisenberg, W. Stroek, N. J. Geels, C. S. Sandu, A. Heller, N. Yan, G. Rothenberg, A Simple Synthesis of an N-Doped Carbon ORR Catalyst: Hierarchical Micro/Meso/Macro Porosity and Graphitic Shells, *Chem. – Eur. J.* **2016**, *22*, 501–505.

[38] C. Li, T. C. Brown, Carbon oxidation kinetics from evolved carbon oxide analysis during temperature-programmed oxidation, *Carbon* **2001**, *39*, 725–732.

[39] L. R. Radović, P. L. Walker, R. G. Jenkins, Importance of carbon active sites in the gasification of coal chars, *Fuel* **1983**, *62*, 849–856.

[40] E. Illeková, K. Csomorová, Kinetics of oxidation in various forms of carbon, *J. Therm. Anal. Calorim.* **2005**, *80*, 103–108.

[41] M. Pawlyta, J.-N. Rouzaud, S. Duber, Raman microspectroscopy characterization of carbon blacks: Spectral analysis and structural information, *Carbon* **2015**, *84*, 479–490.

[42] A. Sadezky, H. Muckenhuber, H. Grothe, R. Niessner, U. Pöschl, Raman microspectroscopy of soot and related carbonaceous materials: Spectral analysis and structural information, *Carbon* **2005**, *43*, 1731–1742.

[43] D. Eisenberg, P. Prinsen, N. J. Geels, W. Stroek, N. Yan, B. Hua, J.-L. Luo, G. Rothenberg, The evolution of hierarchical porosity in self-templated nitrogen-doped carbons and its effect on oxygen reduction electrocatalysis, *RSC Adv.* **2016**, *6*, 80398–80407.

[44] A. J. Bard, L. R. Faulkner, *Electrochemical Methods: Fundamentals and Applications*, Wiley, New York, **2001**.

[45] P. E. Fanning, M. A. Vannice, A DRIFTS study of the formation of surface groups on carbon by oxidation, *Carbon* **1993**, *31*, 721–730.

[46] R.-S. Zhong, Y.-H. Qin, D.-F. Niu, J.-W. Tian, X.-S. Zhang, X.-G. Zhou, S.-G. Sun, W.-K. Yuan, Effect of carbon nanofiber surface functional groups on oxygen reduction in alkaline solution, *J. Power Sources* **2013**, *225*, 192–199.

[47] G. S. Calabrese, R. M. Buchanan, M. S. Wrighton, Mediated electrochemical reduction of oxygen to hydrogen peroxide via a surface-confined naphthoquinone reagent and the mediated electrochemical reduction of a naphthoquinone redox reagent anchored to high surface area oxides, *J. Am. Chem. Soc.* **1983**, *105*, 5594–5600.

[48] G. Jürmann, D. J. Schiffrin, K. Tammeveski, The pH-dependence of oxygen reduction on quinone-modified glassy carbon electrodes, *Electrochim. Acta* **2007**, *53*, 390–399.

Appendix, the Supporting Information for Chapter 2

Experimental

Material Characterization

Temperature-programmed oxidation was performed on a Thermo Fischer TPDRO 1100 series with 25 mg sample sandwiched between two quartz wool layers in a quartz tube reactor (4 mm inner diameter). The system was purged with He and a flow of 5% O_2/He was used during the temperature program. The system was heated with 2 °C/min to 900 °C and the gas output was measured using TCD. Nitrogen adsorption isotherms were measured with a Thermo Scientific Surfer instrument at 77K. Before analysis, the sample was dried in vacuum (10^{-3} mbar) at 200 °C for 3-6 h. For X-ray photoelectron spectroscopy (XPS) a Kratos AXIS equipped with monochromatic Al Kα X-ray source was used and the base pressure in the analytical chamber was 10^{-9} mbar. Raman spectra were measured using a Renishaw InVia system (532 nm and 632.8nm) and a Kaisar Optical Systems RXN-4 system (785 nm) coupled with fiber optics to an immersion probe with a short focal length. Scanning electron microscopy (SEM, FEI Verios 460 with ETD detector) was used to study the morphology of the materials.

Synthesis of the N-doped carbon

All the chemicals were of analytical grade and supplied by Alfa Aesar, Strem Chemical Inc. and Sigma Aldrich. The N-doped carbon was synthesized as reported previously.[A1] In short, nitrilotriacetic acid (22.937 g, 120 mmol, 1 equiv.) and magnesium carbonate ($(MgCO_3)_4Mg(OH)_2$, 11.657 g, 120 mmol Mg, 1 equiv.) were dissolved in water (300 mL) at 85 °C. The resulting yellow solution was stirred for an additional 15 minutes, after which ethanol (1500 mL) was added slowly (± 5 min). The resulting white suspension was cooled in an ice bath for 3 hours, to increase the perception of the magnesium nitrilotriacetic acid (MgNTA). The liquid phase was decanted, producing an off-white gel like product. The product was dried for 3 days under vacuum at 40 °C, yielding a white solid (22-26 grams). Subsequently, the solid was grinded to a powder and

pyrolyzed at 900 °C with a rate of 10 °C/min in a nitrogen (99.999% N_2, 150 mL/min) atmosphere. The resulting coarse carbon powder was washed with a 0.5 M citric acid solution (500 mL) for 24 hours, vacuum filtered, washed with water (3000 mL) and dried at 80 °C for 24 hours. A subsequent thermal treatment at 1000 °C with a ramp of 5 °C/min in a nitrogen atmosphere (99.999% N_2, 150 mL/min) yields the N-doped carbon.

Oxidation and Pyrolysis of the N-doped carbon

The N-doped carbon was oxidized in a 1:3 air:N_2 (99.999% N_2, giving 5% O_2, 150 mL/min) atmosphere. Starting with a 5 °C/min ramp up to the desired temperature of either 350, 450 or 500 °C at which it stayed for 1 hour. Afterwards, the reactor was allowed to naturally cool down. A second thermal treatment was performed, ramping the temperature with 5 °C/min to 900 °C in a nitrogen atmosphere (99.999% N_2, 150 mL/min) for 1 hour.

Electrochemical procedures

Catalyst inks were prepared by suspending 1 mg carbon sample in 1 mL ethanol and 10 µL Nafion® (D-521 dispersion 5 wt.% in water/isopropanol), and sonicated overnight. The Rotating Disk Electrode (RDE) working electrode tip (glassy carbon disk 0.196 cm^{-2}) was polished with diamond polishing film containing 0.1 µm particles and rinsed with water afterwards. The working electrode was prepared by drop casting 6 × 5 µL ink, while air drying between casts. 20 wt.% Pt on Vulcan XC-72 was used for the Pt/C standard.

Electrochemical experiments were performed in a 3-electrode glass cell, with a 0.1 M KOH electrolyte. All electrochemical experiments were performed under 25 °C. A saturated calomel electrode (SCE) was used as a reference electrode, separated from the solution with a luggin capillary. Potentials were reported vs RHE by adding 1.006 V (pH = 13) to the measured SCE potential. A graphite rod was used as a counter electrode, presoaked with the electrolyte 24 hours prior to the measurements. Oxygen was bubbled through the solution for a minimum of 30 min, where after the gas was flown over the solution (gas blanket). Prior to the experiments the solution resistance was measured and 95% of this value was used as a positive correction factor in an automatic iR drop correction. Before measurements, cyclic voltammograms were recorded from 0.3 to 1.0 V vs RHE till no change in current was observed.

Supplementary Figures

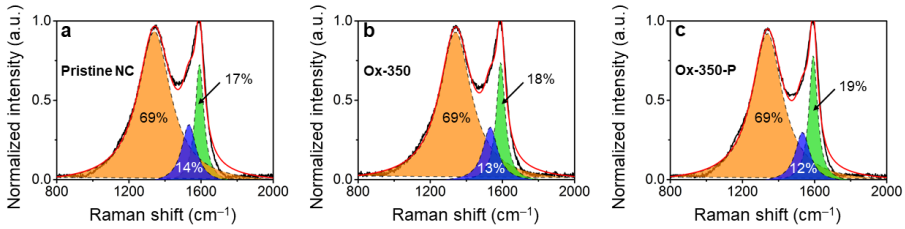

Figure S2.1. *The deconvolution of the Raman spectra of a) Pristine NC, b) Ox-350 and c) Ox-350-P using the D1, D2 and G bands. The numbers of the peaks represent the relative areas of the peaks.*

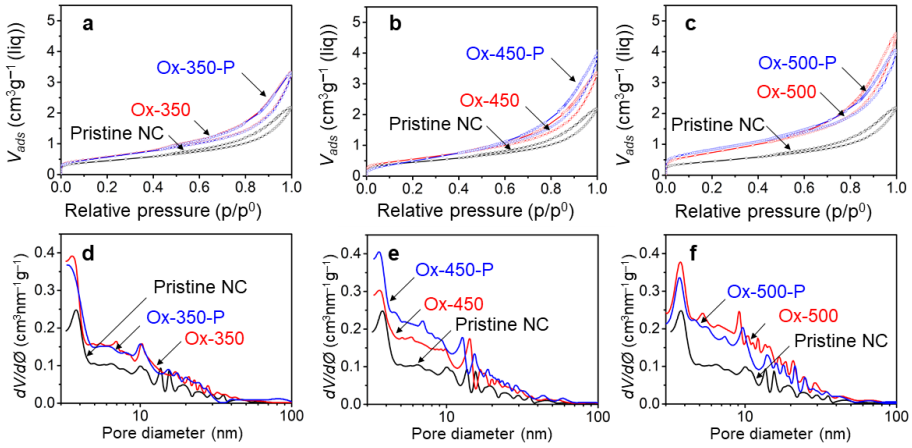

Figure S2.2. *The N_2 adsorption derived BJH mesopore size distribution for of a) 350 °C oxidized samples, b) 450 °C oxidized samples, c) 500 °C oxidized samples.*

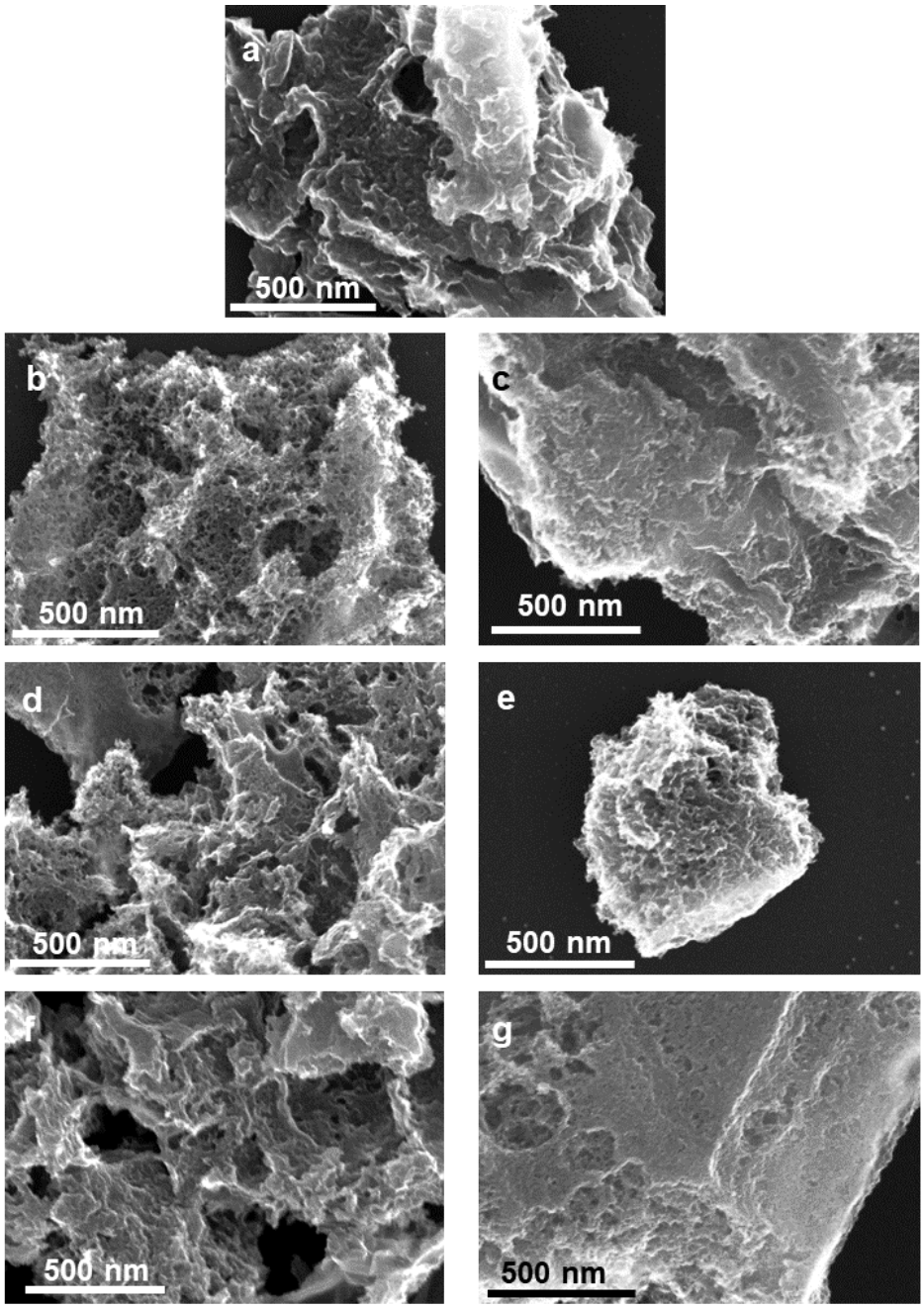

***Figure S2.3**. The SEM micrographs of a) pristine NC, b) Ox-350, c) Ox-350-P, d) Ox-450, e) Ox-450-P, f) Ox-500 and g) Ox-500-P.*

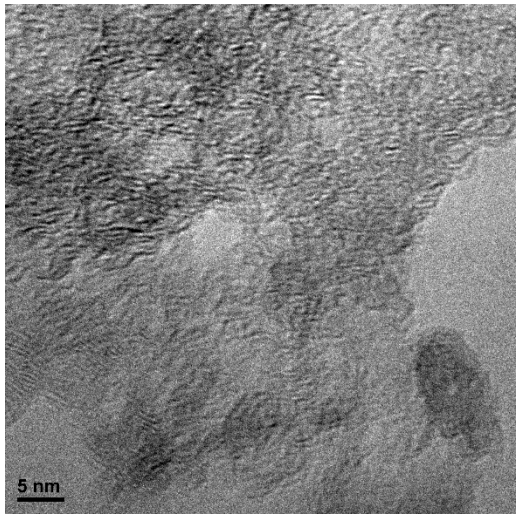

Figure S2.4. *The HRTEM image of Ox-500-P.*

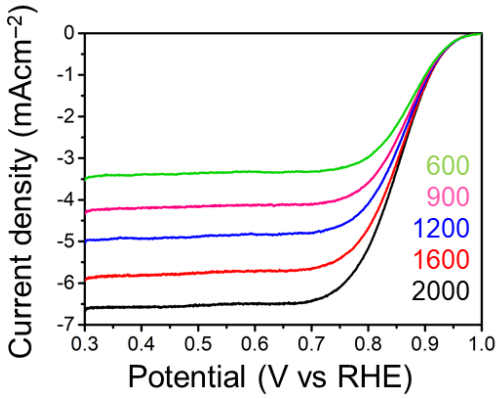

Figure S2.5*. The LSV curves of Ox-500-P at different rotation speeds (rpm).*

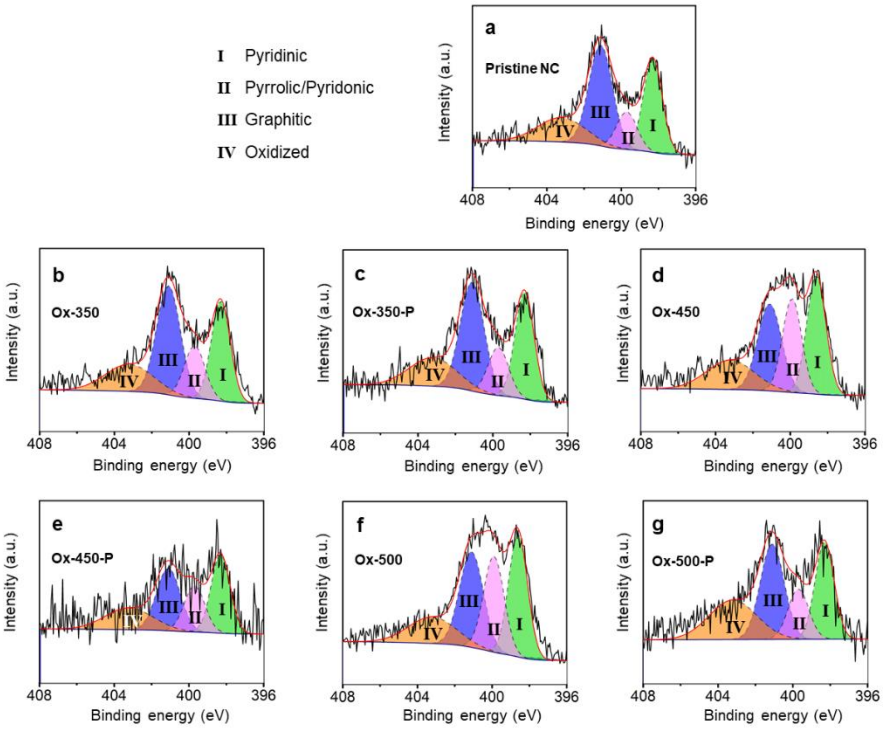

***Figure S2.6**. The deconvolution of the N 1s XPS peak of (a) pristine NC, (b) Ox-350, (c) Ox-350-P, (d) Ox-450, (e) Ox-450-P, (f) Ox-500 and (g) Ox-500-P.*

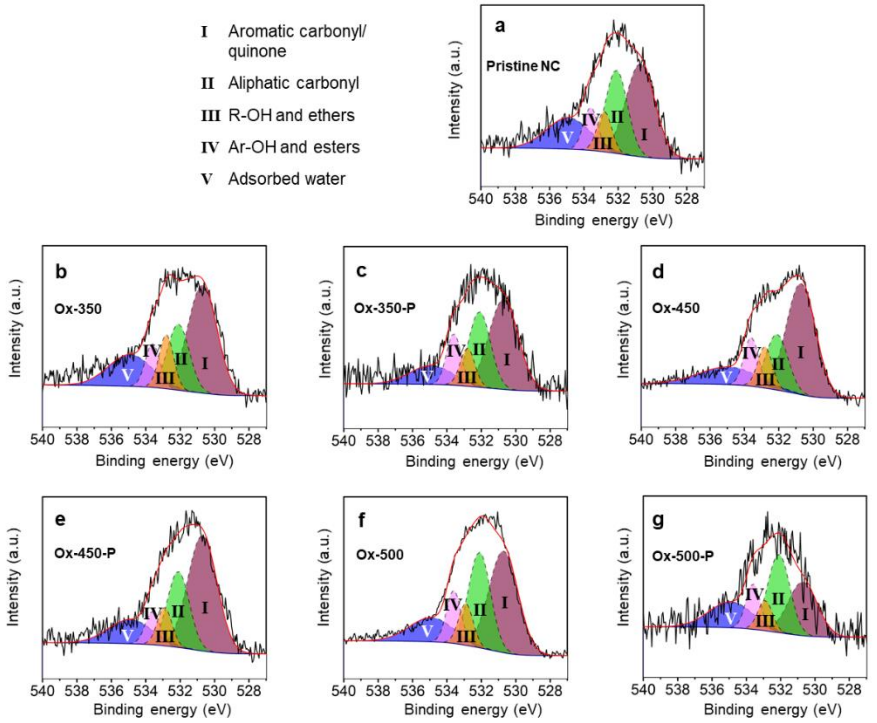

Figure S2.7. *A modified version of the XPS peaks reported by Burg et al was used.*[A2] *The deconvolution of the O 1s XPS peak of (a) pristine NC, (b) Ox-350, (c) Ox-350-P, (d) Ox-450, (e) Ox-450-P, (f) Ox-500 and (g) Ox-500-P.*

Supplementary Tables

Table S2.1. The specific surface area (SSA), pore volume (V_{pore}) and specific capacitance of the NC samples

Entry	Sample	SSA (m^2g^{-1})	V_{pore} (cm^3g^{-1})[a]	Specific capacitance (Fg^{-1})[b]
1	Pristine NC	1320	2.1	36
2	Ox-350	1380	3.4	85
3	Ox-350-P	1360	3.4	38
4	Ox-450	1320	3.4	94
5	Ox-450-P	1360	4.3	41
6	Ox-500	1760	4.5	48
7	Ox-500-P	1930	3.8	35

[a] Barret, Joyner and Halenda (BJH) pore volume calculated from $p/p^o = 0.99$.

[b] Meassured at 20 mV s^{-1}

Table S2.2. Recently reported high-performance N-doped carbons and their ORR activity

Material name	Journal	Onset (V vs RHE)	Halfwave (V vs RHE)	Ref
N-HsGDY-900 °C	Lv *et al.*, Nat. Commun., 2018	~1.0	0.85	[A3]
ONC	Chen *et al.*, Catal. Commun., 2018	0.98	0.87	[A4]
Ox-500-P	**This work**	0.97	0.85	
NCN-1000-5	Jiang *et al.*, Energy Environ. Sci., 2019	0.95	0.82	[A5]
NPMC-1000	Zhang *et al.*, Nat. nanotechnol., 2015	0.94	0.85	[A6]
NG-800	Liu *et al.*, Nat. Commun., 2016	0.92	n.d.	[A7]
Pristine NC[a]	Eisenberg *et al.*, Chem. - Eur. J., 2016	0.91	0.81	[A1]
CCa	Ferrero *et al.*, Carbon, 2016	0.9	0.75	[A8]
N-CNS-120	Yu *et al.*, Adv. Mater., 2016	0.9	0.75	[A9]
NGM	Tang *et al.*, Adv. Mater., 2016	0.89	0.77	[A10]
GZ80C	Thomas *et al.*, ACS Appl. Mater. Interfaces, 2016	0.88	0.75	[A11]
NEMC/G	Lai *et al.*, Adv. Funct. Mater., 2016	0.88	0.82	[A12]
NMCS-3	Tang *et al.*, Angew. Chem., 2015	0.87	n.d.	[A13]
NCNP-CNF	Panomsuwan *et al*, ACS Appl. Mater. Interfaces, 2016	0.82	n.d.	[A14]

[a] This is the base material used in this research

Additional references

[A1] D. Eisenberg, W. Stroek, N. J. Geels, C. S. Sandu, A. Heller, N. Yan, G. Rothenberg, A Simple Synthesis of an N-Doped Carbon ORR Catalyst: Hierarchical Micro/Meso/Macro Porosity and Graphitic Shells, *Chem. – Eur. J.* **2016**, *22*, 501–505.

[A2] P. Burg, P. Fydrych, D. Cagniant, G. Nanse, J. Bimer, A. Jankowska, The characterization of nitrogen-enriched activated carbons by IR, XPS and LSER methods, *Carbon* **2002**, *40*, 1521–1531.

[A3] Q. Lv, W. Si, J. He, L. Sun, C. Zhang, N. Wang, Z. Yang, X. Li, X. Wang, W. Deng, Y. Long, C. Huang, Y. Li, Selectively nitrogen-doped carbon materials as superior metal-free catalysts for oxygen reduction, *Nat. Commun.* **2018**, *9*, 3376.

[A4] Y. Chen, H. Wang, S. Ji, R. Wang, Tailoring the porous structure of N-doped carbon for increased oxygen reduction reaction activity, *Catal. Commun.* **2018**, *107*, 29–32.

[A5] H. Jiang, J. Gu, X. Zheng, M. Liu, X. Qiu, L. Wang, W. Li, Z. Chen, X. Ji, J. Li, Defect-rich and ultrathin N doped carbon nanosheets as advanced trifunctional metal-free electrocatalysts for the ORR, OER and HER, *Energy Environ. Sci.* **2019**, *12*, 322–333.

[A6] J. Zhang, Z. Zhao, Z. Xia, L. Dai, A metal-free bifunctional electrocatalyst for oxygen reduction and oxygen evolution reactions, *Nat. Nanotechnol.* **2015**, *10*, 444–452.

[A7] Y. Liu, Y. Shen, L. Sun, J. Li, C. Liu, W. Ren, F. Li, L. Gao, J. Chen, F. Liu, Y. Sun, N. Tang, H.-M. Cheng, Y. Du, Elemental superdoping of graphene and carbon nanotubes, *Nat. Commun.* **2016**, *7*, 10921.

[A8] G. A. Ferrero, A. B. Fuertes, M. Sevilla, M.-M. Titirici, Efficient metal-free N-doped mesoporous carbon catalysts for ORR by a template-free approach, *Carbon* **2016**, *106*, 179–187.

[A9] H. Yu, L. Shang, T. Bian, R. Shi, G. I. N. Waterhouse, Y. Zhao, C. Zhou, L.-Z. Wu, C.-H. Tung, T. Zhang, Nitrogen-Doped Porous Carbon Nanosheets Templated from g-C3N4 as Metal-Free Electrocatalysts for Efficient Oxygen Reduction Reaction, *Adv. Mater.* **2016**, *28*, 5080–5086.

[A10] C. Tang, H.-F. Wang, X. Chen, B.-Q. Li, T.-Z. Hou, B. Zhang, Q. Zhang, M.-M. Titirici, F. Wei, Topological Defects in Metal-Free Nanocarbon for Oxygen Electrocatalysis, *Adv. Mater.* **2016**, *28*, 6845–6851.

[A11] M. Thomas, R. Illathvalappil, S. Kurungot, B. N. Nair, A. A. P. Mohamed, G. M. Anilkumar, T. Yamaguchi, U. S. Hareesh, Graphene Oxide Sheathed ZIF-8 Microcrystals: Engineered Precursors of Nitrogen-Doped Porous Carbon for Efficient Oxygen Reduction Reaction (ORR) Electrocatalysis, *ACS Appl. Mater. Interfaces* **2016**, *8*, 29373–29382.

[A12] Q. Lai, Y. Zhao, Y. Liang, J. He, J. Chen, In Situ Confinement Pyrolysis Transformation of ZIF-8 to Nitrogen-Enriched Meso-Microporous Carbon Frameworks for Oxygen Reduction, *Adv. Funct. Mater.* **2016**, *26*, 8334–8344.

[A13] Tang Jing, Liu Jian, Li Cuiling, Li Yunqi, Tade Moses O., Dai Sheng, Yamauchi Yusuke, Synthesis of Nitrogen-Doped Mesoporous Carbon Spheres with Extra-Large Pores through Assembly of Diblock Copolymer Micelles, *Angew. Chem. Int. Ed.* **2015**, *54*, 588–593.

[A14] G. Panomsuwan, N. Saito, T. Ishizaki, Nitrogen-Doped Carbon Nanoparticle–Carbon Nanofiber Composite as an Efficient Metal-Free Cathode Catalyst for Oxygen Reduction Reaction, *ACS Appl Mater Interfaces* **2016**, 10.

Chapter 3

Treating Organic Pollutants – Electrochemical H_2O_2 Generation via a Nitrogen-Doped Carbon

The direct synthesis of hydrogen peroxide using sustainable energy and molecular oxygen is a promising alternative approach to the conventional batch synthesis. Here we present a manganese and nitrogen co-doped carbon material which catalyzes the selective reduction of dioxygen in an acidic environment to hydrogen peroxide. The onset potential is close to 0.7 V, with >98% H_2O_2 selectivity in the range of 0.7–0.5 V *vs* RHE. This is the highest reported to date, outperforming many bimetallic noble metal catalysts. Besides, this doped carbon material is hierarchically porous, featuring both a large mesopore volume (4.54 mL g^{-1}) *and* a high specific surface area (1333 m^2 g^{-1}). This enables the effective adsorption of bulky organics such as methylene blue (385 mg g^{-1}). Combined with the formation of hydroxyl radicals during electrochemical H_2O_2 generation, this material also enables the efficient electrochemical degradation of methylene blue, as evidenced by *in situ* UV-vis spectrometry.

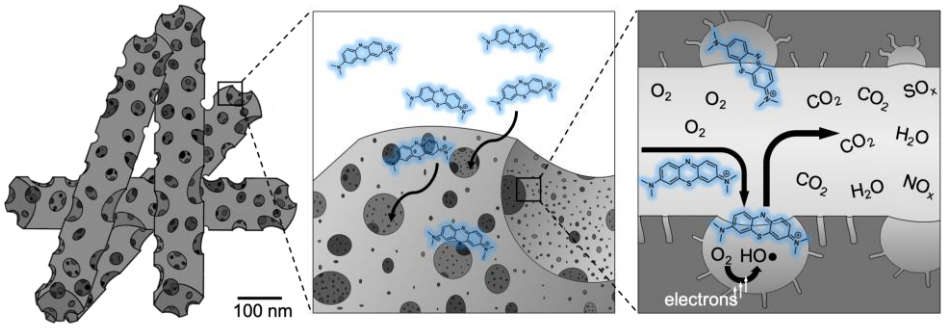

Parts of this chapter have been published as J. Biemolt, K. van der Veen, N.J. Geels, G. Rothenberg, N. Yan, Efficient oxygen reduction to H_2O_2 in highly porous manganese and nitrogen co-doped carbon nanorods enabling electro-degradation of bulk organics, *Carbon* **2019**, *155*, 643–649.

Introduction

Industrial wastewater often contains toxic organic pollutants. Traditional water treatment traps these contaminants in the sludge, incurring a large environmental footprint.[1–4] Recently, electrochemical methods using electrons as "clean reagents" have attracted much attention.[5–10] In particular, the oxygen reduction reaction (ORR) takes advantage of the readily-available oxygen dissolved in the water to produce hydrogen peroxide. This reaction is often associated with the formation of hydroxyl and peroxyl radicals at the electrode.[11–13] These radicals can break up even the most resistant organic compounds. Yet converting O_2 electrocatalytically into H_2O_2 is no easy task. The state-of-the-art platinum catalysts often facilitate the 4-electron transfer reaction, producing mainly water with little H_2O_2.[14–16] Alloying Pt with suitable transition metals such as Au and Hg can boost the H_2O_2 selectivity to > 90%,[17] but these catalysts are expensive and their working potential at the benchmark 1 mA cm^{-2} is often below 0.4 V vs RHE. As we[18–21] and others[22–24] recently showed, metal-free carbon catalysts show excellent ORR activity in alkaline media. But most of these are not H_2O_2-selective and show poor activity under acidic conditions.[25] There are exceptions: a carbon-based catalyst tailored to produce H_2O_2 selectively in an acidic electrolyte was reported by Liu *et al.*[26] Their material, made from MOF-5, showed a 0.42 V vs RHE onset potential and a H_2O_2 selectivity of 90%. Elsewhere, Fellinger *et al.* used acidic media for their mesoporous nitrogen-doped carbon, reporting an onset potential of 0.55 V vs RHE and 95% H_2O_2 selectivity (other high-performance H_2O_2 catalysts are listed in Table S1 in the supporting information).

Because the reactive hydroxyl radicals are short-lived, the organic contaminants must be adsorbed and held at the electrode in close proximity to the radical-generating sites. This means that the H_2O_2-formation catalyst should be a porous material, allowing the capture of the organic pollutants. Pollutants come in all sizes, and the pore structure of the electrode must be designed appropriately. For instance, simple aromatics such as benzene, toluene and xylene have kinetic diameters < 8 Å, fitting easily in micropores. But many dyes,[27–30] surfactants[31,32] and pharmaceutical compounds[33,34] can be >2 nm in size, requiring larger pores for effective adsorption and mass transfer. Ideally, we want hierarchically porous electrodes with a high micropore volume *and* a high mesopore volume. Carbon materials are suitable electrode materials, due to their high conductivity, low cost and tunable pore structure. Many groups are working

on this topic (see also Table S2 in the supporting information for details): Schuster *et al.* prepared a spherical mesoporous carbon with 2.32 cm^3g^{-1} pore volume and SSA of 2445 m^2g^{-1} via a complex double 'hard' templating method.[35] Elsewhere, Xu *et al.* reported the synthesis of hollow NC nanospheres with a surface area of 3022 m^2g^{-1} and pore volume of 2.43 cm^3g^{-1} NC using a 'soft' templating technique.[36] Using MOF-5 as the precursor, a hierarchically mesoporous carbon with a SSA of 2734 m^2g^{-1} and pore volume of 5.53 cm^3g^{-1} was reported by Srinivas *et al.*[32] We also reported a series of NCs with hierarchical porosity showing excellent catalytic activities using the same approach.[18] Yet making hierarchically porous carbons with a high surface area and a large mesopore volume remains a challenge.

Based on our recent research into nitrogen-doped carbon (NC) catalysts, we hypothesized that an active and selective catalyst for reducing O_2 to H_2O_2 with a high pore volume would both capture bulky organic pollutants from water and catalyze their degradation. Here we report a facile synthesis of hierarchically Mn and N co-doped carbon nanorods (Mn-NC) starting from nitrilotriacetic acid. This material, with its large pore volume of 4.54 cm^3g^{-1} and a high specific surface area of 1333 m^2g^{-1}, can adsorb 385 mgg^{-1} of methylene blue (MB, a dye with many industrial applications).[33–37] Importantly, our catalyst converts O_2 selectively into H_2O_2, exhibiting a high onset potential of *ca.* 0.7 V vs RHE in 0.1 M $HClO_4$. The hydroxyl radicals degrade the adsorbed MB in the adjacent area within the

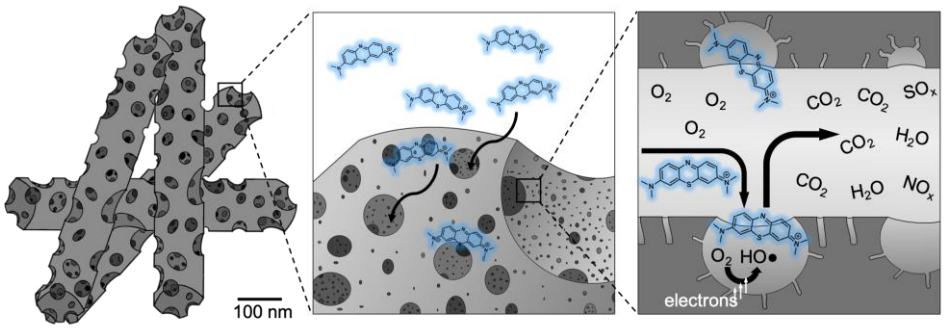

Figure 3.1. *The manganese and nitrogen co-doped carbon nanorods have macropores, mesopores and micropores, enabling the adsorption of large contaminant molecules such as methylene blue and their subsequent decomposition through the generation of hydroxyl radicals via simultaneous electrochemical oxygen reduction.*

porous electrode (see schematic in Figure 3.1). This combined adsorption and electrocatalytic activity opens new opportunities for wastewater treatment as well as for electrocatalysis applications.

Results and Discussion

The Mn-NC nanorods were prepared by adapting our previously published method (detailed experimental procedures are included in the supporting information).[21] Briefly, nanorods of the manganese nitrilotriacetate precursor were synthesized hydrothermally. Subsequent pyrolysis and acid-washing removed the MnO particles, yielding the Mn and N co-doped carbon (see Figure 3.2a). Scanning transmission electron microscopy (STEM) measurements confirmed that all of the MnO particles were removed (Figure 3.2b). The nanorods have abundant mesopores (D <20 nm) which are visible in the magnified SEM image in Figure 3.2c. These mesopores vary in size, enabling the

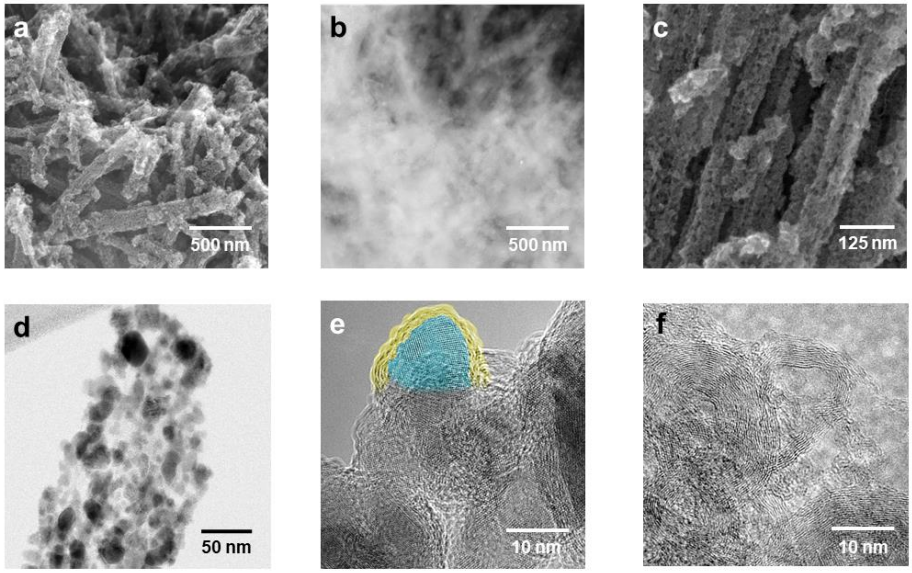

Figure 3.2. *(a) SEM and the corresponding (b) STEM images of the Mn-NC nanorods; (c) magnified SEM image of Mn-NC shows abundant mesopores in the nanorods; (d) bright-field TEM micrograph of a MnO-imbedded Mn-NC nanorod; HRTEM micrographs of (e) the imbedded MnO template in Mn-NC (colored in cyan and yellow respectively, unaltered version in Figure S3.2), and (f) the mesopores with graphitic shells of Mn-NC after acid washing.*

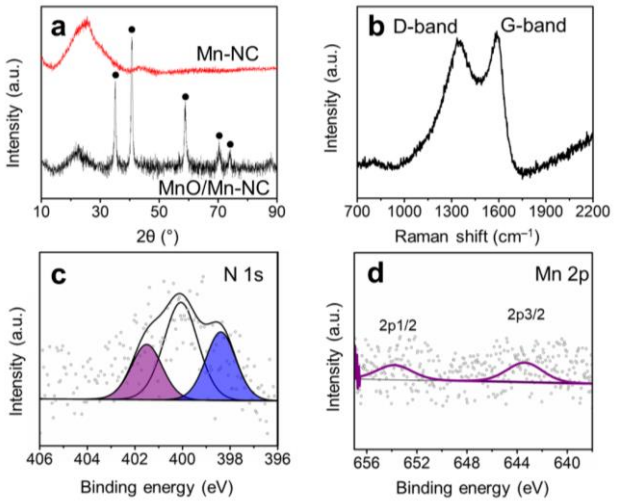

Figure 3.3. *(a) XRD of the MnO/Mn-NC hybrid material and the Mn-NC nanorods acquired after the acid wash with '●' symbols denoting the peaks for MnO, (b) the Raman spectrum and (c,d) the XPS spectra of the Mn-NC nanorods.*

adsorption of different contaminants. By comparing the high-resolution transmission electron microscopy (HRTEM) images in Figures 3.2e and 3.2f, we confirmed that these mesopores were templated by the MnO nanoparticles. The pore walls are made of graphitic carbon shells. They are typically less than 20 layers in thickness, containing many worm-like micropores. This connectivity creates a hierarchical pore structure (*vide infra*).

Figure 3.3a compares the powder XRD patterns of MnO/Mn-NC and the Mn-NC nanorods. Three strong peaks in MnO/Mn-NC at $2\theta = 35.0°$, 40.7° and 58.8° correspond to the (111), (200) and (220) planes of MnO, respectively. The Mn-NC nanorods had no residual MnO. The broad peak at $2\theta = 25°$ was assigned to the graphite (002) plane. From the Raman spectrum in Figure 3.3b we infer that the Mn-NC nanorods contain both ordered and disordered carbon domains, (*cf.* the D- and G-band at 1351 and 1588 cm^{-1}, respectively).[39] Again, no MnO signal (typically below 800 cm^{-1}) was observed. The presence of Mn and N moieties in the carbon was verified by X-ray photoelectron spectroscopy (XPS, Figure 3.3c). It revealed a 1.5% nitrogen content including graphitic, pyridinic and oxidized N, of which *ca.* 20% was pyridinic nitrogen.[21]

We then studied the pore structure using both nitrogen adsorption and mercury intrusion porosimetry. The nitrogen adsorption isotherm (Figure 3.4a), shows a combination of a H3 and H4 hysteresis loops, implying the presence of micro-, meso- and macropores.[40] A BET analysis gave a high specific surface area of 1333 $m^2 g^{-1}$. We used the Saito and Foley model to examine the micropore volume and micropore size distribution (see Figure 3.4b). This model indicated a micropore volume of 0.76 mL g^{-1}, with most pores > 0.6 nm. As CO_2 is produced during the pyrolysis, these pores might be created by the typical CO_2 activation process.[41] For comparison, we measured under the same conditions a control sample of commercial activated carbon. This had a similar specific surface area of 1301 $m^2 g^{-1}$ and a micropore volume of 0.64 mL g^{-1}.

In the middle region of the isotherm, our Mn-NC differs from the commercial carbon sample. The adsorption-desorption hysteresis of Mn-NC nanorod suggests the existence of mesopores. Analysis of the isotherm using Gurvich model revealed a pore volume of 4.54 mLg^{-1} at 0.99 p/p^0.[42] This value

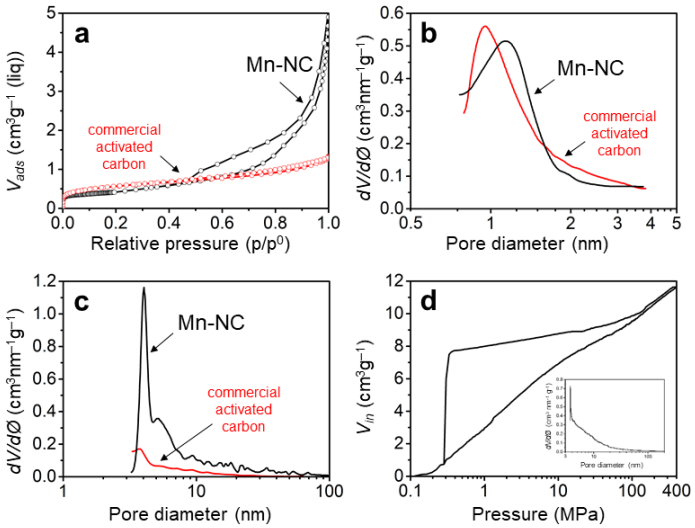

Figure 3.4. *(a) The N_2 adsorption isotherms at 77K, adjusted to adsorbed liquid volume, (b) the micropore size distributions derived from the N_2 isotherms using the Saito and Foley analysis, (c) the mesopore size distributions from the N_2 isotherms using the Barrett-Joyner-Halenda analysis of the Mn-NC nanorods and commercial activated carbon; and (d) the mercury intrusion curve of the Mn-NC nanorods.*

surpasses most of the porous carbon materials reported to date (for a detailed comparison see Table S3.2 in the supporting information). Most of the mesopores in our material are < 10 nm in diameter (see Figure 3.4c). This matches well the observations from the TEM micrographs. The mesopore volume calculated from the mercury intrusion porosimetry (Figure 3.4d) reached 3.45 mL g^{-1}, derived from the intruded volume between pore sizes 3.6 - 50 nm (p = 29.6 MPa for 50 nm, $\theta = 140°$, $\gamma = 0.48$ N m^{-1}). This is slightly lower than that obtained from N_2 adsorption. Most likely, the difference is caused by ink-bottle shaped pores where the pore opening is too small for mercury to enter. The pore size distribution shows that most of the pores are < 15 nm in diameter (inset of Figure 3.4d).

To evaluate the performance of our porous nanorods in the adsorption and electrocatalytic degradation of methylene blue (MB) illustrated in Figure 3.1, we initially studied their capability of removing 50 ppm MB from an aqueous solution. This was compared to a commercial activated carbon which is essentially microporous with similar surface area (see Figure 3.4a, 3.4b, 3.4c and Table 3.1 for the N_2 adsorption comparisons). After adding 5 mg of either Mn-NC or activated carbon to 25 mL 50 ppm MB solution (pH was adjusted to 4 using HCl) and shaking gently, the blue color in the Mn-NC suspension disappeared almost instantly. The complete removal of MB was confirmed by UV-visible spectroscopy (Figure 3.5b). In contrast, the activated carbon suspension still displayed a light blue color even after 12 h agitation (see Figure 3.5a). This implies that the carbon was already saturated by MB and could not remove the residual MB from the suspension.

To quantify the MB uptake, we measured its adsorption from solutions with varied concentrations, from 25 ppm up to 300 ppm. In each case, the amounts of adsorbed MB on the material and remaining MB in solution at equilibrium were measured and denoted as q_e (mg g^{-1}) and C_e, (mg L^{-1}), respectively. Fitting the q_e-C_e plot using established adsorption models can reveal the adsorption mechanism and maximum uptake of MB for each adsorbent.[43] Here we used the Langmuir, Freundlich and Redlich-Peterson adsorption models (see Supporting Information for details).[44–47] The adsorption model parameters acquired from the linear fit of the models are summarized in Table S3.2. Figures 3.5c and 3.5d compares the MB adsorption isotherms of the Mn-NC nanorods and the commercial activated carbon. The commercial activated carbon clearly follows the Langmuir and Redlich-Peterson isotherm models, suggesting a monolayer

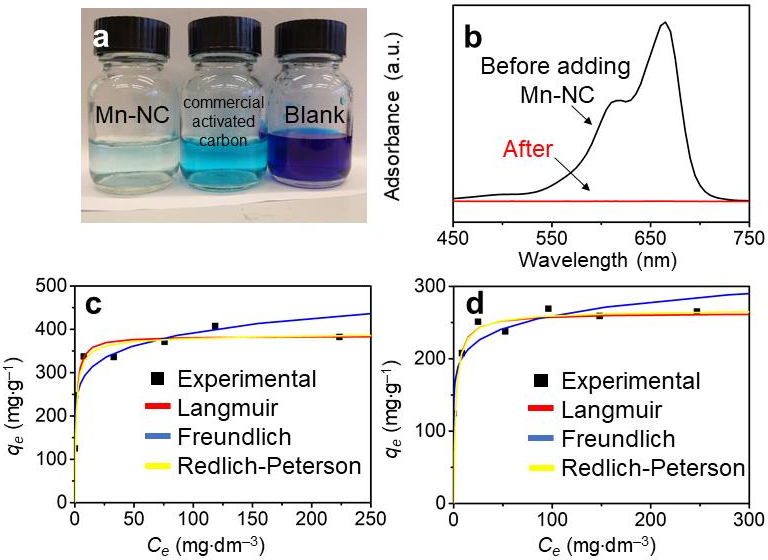

Figure 3.5. *(a) Photo of three vials containing 25 mL of a 50 ppm MB solutions after the addition of 5 mg Mn-NC nanorods, 5 mg commercial activated carbon and nothing; (b) The UV-Vis spectrum of a 50 ppm MB solution before and after adding 5 mg Mn-NC nanorods; Experimental data and fittings of the adsorption isotherm of MB for (c) Mn-NC nanorods and (d) the commercial activated carbon.*

Table 3.1. BET SSA, Saito and Foley micropore, BJH mesopore and BJH total pore volume of both the NC and the commercial activated carbon.

Carbon	**SSA (m^2g^{-1})**	**Micropore volume (mLg^{-1})**	**Gurvich pore volume[a] (mLg^{-1})**	**Hg intrusion mesopore volume (mLg^{-1})**
Mn-NC nanorods	1333	0.76	4.54	3.45
Commercial activated carbon (Norit Darco)	1301	0.64	0.75	n.a.

[a] Gurvich volume calculated with $p/p^o = 0.99$

adsorption of MB. The Mn-NC results fit both the Langmuir and Freundlich model well, but show a maximum in the MB adsorption. When the Langmuir model is considered, we used the monolayer saturation capacity (Q), equaling to k_L/a_L, to quantify the maximum MB uptake in the adsorbent. Albeit that both samples showed a similar specific surface area, their Q values differ significantly: 385 mg g^{-1} for the Mn-NC sample compared to only 263 mg g^{-1} for the commercial activated carbon.

In fact, when the molecular dimension of the adsorbate is sufficiently small, such as that of N_2, CO_2 and K^+/OH^-, the adsorption capability of the adsorbent can, in many cases, be simply maximized by increasing its specific surface area that is mainly attributed by the micropore. This principle has been applied in developing high-performance materials for supercapacitors and CO_2 adsorption.[45–49] However, when the molecular dimension of the adsorbate is large, such as that of dyes and surfactants, the adsorbate will transfer slowly in the adsorbent and can easily block the small micropores during the adsorption process (see the schematic comparison in Figure S3.3). In this case, the material with more mesopores is much advantageous in capturing and accommodating these bulky molecules.[30,53,54] The large MB molecules (1.3–1.8 nm diameter[28,55,56]) may block the micropores of the commercial activated carbon.[30,53,54] In addition, the commercial activated carbon would also suffer from a lower mass transport. Consequently, our hierarchically porous Mn-NC nanorods with high specific surface area and mesopore volume showed a superior capability in adsorbing MB.

We studied the catalytic activity of Mn-NC nanorods in producing H_2O_2 from the dissolved O_2 through the electrocatalytic oxygen reduction reaction. The ORR activity and selectivity of both the Mn-NC nanorods and commercial activated carbon were tested in a 0.1 M $HClO_4$ electrolyte. Cyclic voltammetry using a rotating disc electrode in the N_2-saturated electrolyte only showed capacitive behaviors for both materials (Figure S3.3). In the O_2-saturated electrolyte, reduction peaks at *ca.* 0.6 and 0.3 V vs RHE were observed for the Mn-NC nanorods and commercial activated carbon, respectively, which confirmed that ORR has occurred at these potentials.

We then used a rotating ring disk electrode (RRDE) for evaluating the ORR activity and H_2O_2 selectivity. Figure 3.6a compares the linear sweep

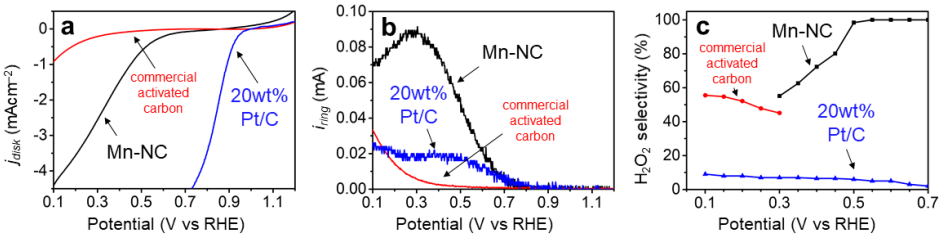

Figure 3.6. *(a) Disk current density and (b) ring current from the RRDE experiments; (c) the H_2O_2 selectivity at different potentials. The measurements were performed in a O_2 saturated 0.1 M $HClO_4$, with a scan rate of 10 mV s^{-1} and the rotating speed of 1600 rpm.*

voltammograms (LSVs) of the disk for three different samples: commercial activated carbon (red), Mn-NC nanorods (black) and 20 wt% Pt/C (blue). The Mn -NC nanorods have an onset potential of *ca.* 0.7 V vs RHE. This agrees with the observed potential from the ring when H_2O_2 oxidation starts (see Figure 3.6b). This value is close to the standard reduction potential $E^0_{(O_2/H_2O_2)}$ = 0.7 V and is among the highest reported for the O_2-H_2O_2 conversion.[17,26,57–60] Moreover, unlike many excellent carbon-based ORR catalysts,[18,23,61,62] our NC nanorods showed not only high activity in acidic media, but also exceptionally high H_2O_2 selectivity (98%) at potentials > 0.5 V vs RHE (see Figure 3.6c). At the benchmark 1 mA cm^{-2}, the potential reached 0.41 V vs RHE and the selectivity remained 74%, comparable with the noble metal catalyst. A detailed comparison with the state-of-the-art is included in the Table S3.1. Note that the Pt/C showed better ORR activity with an onset potential of 0.92 V vs RHE, due to the 4-electron transfer reaction pathway in which the O_2 was fully reduced to H_2O. The H_2O_2 selectivity for the Pt/C catalyst was <10%, in good agreement with published results.[63] The commercial activated carbon is inactive in the acidic electrolyte, with a very low current and H_2O_2 yield.

H_2O_2 is not a strong enough oxidizing agent to degrade many "robust" organic pollutants directly (such as the aromatics and MB).[64,12] Typically, the oxidation can only occurs via the scission of the peroxo bond and the generation of active free-radicals (eq 3.1). Transition metal ions are often applied as the catalysts,[65–67] as is the activated carbon.[68,69] Remarkably, the advantage of converting O_2 into H_2O_2 electrochemically is the formation *in situ* of these hydroxyl and peroxyl radical intermediates.[11–13] A 3-electron transfer process

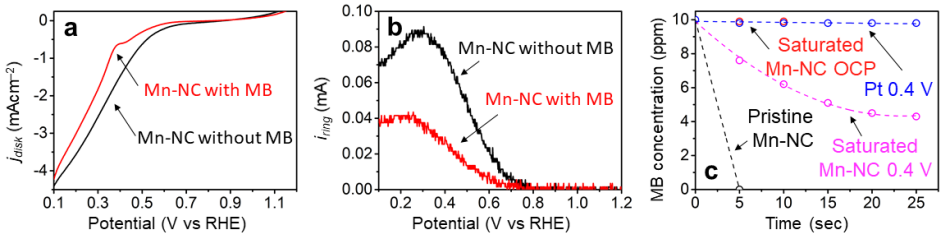

Figure 3.7. *(a) Disk current density and (b) ring current from the RRDE experiments in a O_2 saturated 0.1 M $HClO_4$ with and without the addition of 25 ppm MB, the scan rate is 10 mV s^{-1} and the rotating speed is 1600 rpm, (c) in situ UV-Vis measurements for the oxidation of MB by the Mn-NC nanorods.*

and a mono-electron reduction of H_2O_2 have been proposed as the two possible pathways (eqs 3.2 and 3.3):

$$2H_2O_2 \rightarrow HOO^{\cdot} + OH^{\cdot} + H_2O \qquad (3.1)$$

$$O_2 + 3H^+ + 3e^- \rightarrow OH^{\cdot} + H_2O \qquad (3.2)$$

$$H_2O_2 + e^- + H^+ \rightarrow OH + H_2O \qquad (3.3)$$

With the presence of hydroxyl radicals, the complete oxidation of MB can be achieved following eq (3.4) with minimal toxic products release.[71] As the hydroxyl radicals can be rapidly reduced to hydroxyl ions, it is critical that MB is pre-adsorbed in the porous structure where the radical-generation sites are nearby (see Figure 3.1).

$$C_{16}H_{18}N_2SCl \xrightarrow{51\ OH^{\cdot}} 16CO_2 + 6H_2O + H_2SO_4 + 3HNO_3 + HCl \qquad (3.4)$$

Before studying the electrocatalytic degradation of MB, we first examined whether the adsorption of MB will cause the poison of our catalyst. Figure 3.7a compares the performances of Mn-NC nanorods with and without the presence of 25 ppm MB. Despite the fact that the reduction current has shifted a little to lower voltages due to the MB addition, the onset potential barely changed. This is also reflected by the unchanged onset potential, recorded at the ring in Figure 3.7b, at which the production of H_2O_2 starts. The current drops in both the ring and disk after adding MB can be ascribed to (1) blockage of active site by adsorbed MB molecules and (2) the consumption of peroxyl or hydroxyl radicals by MB.

To study the electrocatalytic degradation of MB, we performed an *in-situ* UV-vis spectrometric study using a three-electrode cell. The electrolyte was also O_2-saturated 0.1 M $HClO_4$ containing 10 ppm MB and the working electrode was biased at 0.4 V vs RHE (see supporting information for details). Because the Pt wire reference electrode can catalyze the generation of hydroxyl radicals through eq.1, we limited the test time to <30 s. We anticipated that this can avoid the contact between the generated H_2O_2 and Pt wire. In the Pt working electrode test, the concentration of MB remained constant in time (see Figure 3.7c). Interestingly, the test with pristine Mn-NC nanorod showed that all of the MB disappeared after only 5 s. However, this was not because of the electrocatalytic degradation of MB, but was ascribed to the rapid adsorption of MB on the working electrode. To exclude this artefact, we first immersed the Mn-NC nanorod working electrode in 10 ppm electrolyte with sufficient volume. Then the MB-saturated working electrode, denoted as treated Mn-NC, was then mounted in the *in situ* cell. A clear MB concentration decrease was observed progressively only when the potential was applied, confirming the electrocatalytic decomposition.

Conclusions

The decomposition of organic pollutants in water can be done efficiently if one combines adsorption, electrocatalysis, and free-radical reactions. Hierarchically porous carbon nanorods co-doped with manganese and nitrogen are ideal for this purpose, as they have both a large surface area and a high pore volume, as well as good active sites. These materials can adsorb large amounts of methylene blue from water (385 mg g^{-1}, 46% higher compared to a commercial activated carbon with a similar surface area). Importantly, they also catalyze the electrochemical reduction of dixoygen to hydrogen peroxide with >98% selectivity. *In situ* generation of hydroxyl free-radicals at the catalyst surface enables the efficient decomposition of methylene blue. The catalysts are made from abundant elements, and can be produced on gram scale. We hope that the results reported here will stimulate researchers to use these materials in a variety of applications.

References

[1] Y. Yang, Y. Zhao, A. Babatunde, L. Wang, Y. Ren, Y. Han, Characteristics and mechanisms of phosphate adsorption on dewatered alum sludge, *Sep. Purif. Technol.* **2006**, *51*, 193–200.

[2] K. C. Makris, D. Sarkar, R. Datta, Aluminum-based drinking-water treatment residuals: A novel sorbent for perchlorate removal, *Environ. Pollut.* **2006**, *140*, 9–12.

[3] A. O. Babatunde, Y. Q. Zhao, Constructive Approaches Toward Water Treatment Works Sludge Management: An International Review of Beneficial Reuses, *Crit. Rev. Environ. Sci. Technol.* **2007**, *37*, 129–164.

[4] E. Igos, A. Dalle, L. Tiruta-Barna, E. Benetto, I. Baudin, Y. Mery, Life Cycle Assessment of water treatment: what is the contribution of infrastructure and operation at unit process level?, *J. Clean. Prod.* **2014**, *65*, 424–431.

[5] E. Brillas, J. C. Calpe, J. Casado, Mineralization of 2,4-D by advanced electrochemical oxidation processes, *Water Res.* **2000**, *34*, 2253–2262.

[6] T.-C. An, X.-H. Zhu, Y. Xiong, Feasibility study of photoelectrochemical degradation of methylene blue with three-dimensional electrode-photocatalytic reactor, *Chemosphere* **2002**, *46*, 897–903.

[7] S. Yuan, M. Tian, Y. Cui, L. Lin, X. Lu, Treatment of nitrophenols by cathode reduction and electro-Fenton methods, *J. Hazard. Mater.* **2006**, *137*, 573–580.

[8] H. Ma, Q. Zhuo, B. Wang, Electro-catalytic degradation of methylene blue wastewater assisted by Fe2O3-modified kaolin, *Chem. Eng. J.* **2009**, *155*, 248–253.

[9] M. A. Hassan, M. M. El Jamal, Kinetic Study of the Electrochemical Oxidation of Methylene Blue with Pt Electrode:, *Port. Electrochim. Acta* **2012**, *30*, 351–359.

[10] L. Ma, M. Zhou, G. Ren, W. Yang, L. Liang, A highly energy-efficient flow-through electro-Fenton process for organic pollutants degradation, *Electrochim. Acta* **2016**, *200*, 222–230.

[11] Q. Yue, K. Zhang, X. Chen, L. Wang, J. Zhao, J. Liu, J. Jia, Generation of OH radicals in oxygen reduction reaction at Pt–Co nanoparticles supported on graphene in alkaline solutions, *Chem. Commun.* **2010**, *46*, 3369.

[12] J.-M. Noël, A. Latus, C. Lagrost, E. Volanschi, P. Hapiot, Evidence for OH Radical Production during Electrocatalysis of Oxygen Reduction on Pt Surfaces: Consequences and Application, *J. Am. Chem. Soc.* **2012**, *134*, 2835–2841.

[13] K. Sobańska, P. Pietrzyk, Z. Sojka, Generation of Reactive Oxygen Species via Electroprotic Interaction of H_2O_2 with ZrO_2 Gel: Ionic Sponge Effect and pH-Switchable Peroxidase- and Catalase-Like Activity, *ACS Catal.* **2017**, *7*, 2935–2947.

[14] Z. Wen, J. Liu, J. Li, Core/Shell Pt/C Nanoparticles Embedded in Mesoporous Carbon as a Methanol-Tolerant Cathode Catalyst in Direct Methanol Fuel Cells, *Adv. Mater.* **2008**, *20*, 743–747.

[15] M. Inaba, M. Ando, A. Hatanaka, A. Nomoto, K. Matsuzawa, A. Tasaka, T. Kinumoto, Y. Iriyama, Z. Ogumi, Controlled growth and shape formation of platinum nanoparticles and their electrochemical properties, *Electrochimica Acta* **2006**, *52*, 1632–1638.

[16] R. Kou, Y. Shao, D. Wang, M. H. Engelhard, J. H. Kwak, J. Wang, V. V. Viswanathan, C. Wang, Y. Lin, Y. Wang, I. A. Aksay, J. Liu, Enhanced activity and stability of Pt catalysts on functionalized graphene sheets for electrocatalytic oxygen reduction, *Electrochem. Commun.* **2009**, *11*, 954–957.

[17] S. Siahrostami, A. Verdaguer-Casadevall, M. Karamad, D. Deiana, P. Malacrida, B. Wickman, M. Escudero-Escribano, E. A. Paoli, R. Frydendal, T. W. Hansen, I. Chorkendorff, I. E. L. Stephens, J. Rossmeisl, Enabling direct H2O2 production through rational electrocatalyst design, *Nat. Mater.* **2013**, *12*, 1137–1143.

[18] D. Eisenberg, W. Stroek, N. J. Geels, C. S. Sandu, A. Heller, N. Yan, G. Rothenberg, A Simple Synthesis of an N-Doped Carbon ORR Catalyst: Hierarchical Micro/Meso/Macro Porosity and Graphitic Shells, *Chem. – Eur. J.* **2016**, *22*, 501–505.

[19] D. Eisenberg, W. Stroek, N. J. Geels, S. Tanase, M. Ferbinteanu, S. J. Teat, P. Mettraux, N. Yan, G. Rothenberg, A rational synthesis of hierarchically porous, N-doped carbon from Mg-based MOFs: understanding the link between nitrogen content and oxygen reduction electrocatalysis, *Phys. Chem. Chem. Phys.* **2016**, *18*, 20778–20783.

[20] D. Eisenberg, P. Prinsen, N. J. Geels, W. Stroek, N. Yan, B. Hua, J.-L. Luo, G. Rothenberg, The evolution of hierarchical porosity in self-templated nitrogen-doped carbons and its effect on oxygen reduction electrocatalysis, *RSC Adv.* **2016**, *6*, 80398–80407.

[21] J. Pandey, B. Hua, W. Ng, Y. Yang, K. van der Veen, J. Chen, N. J. Geels, J.-L. Luo, G. Rothenberg, N. Yan, Developing hierarchically porous MnOx/NC hybrid nanorods for oxygen reduction and evolution catalysis, *Green Chem.* **2017**, *19*, 2793–2797.

[22] K. Gong, F. Du, Z. Xia, M. Durstock, L. Dai, Nitrogen-Doped Carbon Nanotube Arrays with High Electrocatalytic Activity for Oxygen Reduction, *Science* **2009**, *323*, 760–764.

[23] L. Yang, S. Jiang, Y. Zhao, L. Zhu, S. Chen, X. Wang, Q. Wu, J. Ma, Y. Ma, Z. Hu, Boron-Doped Carbon Nanotubes as Metal-Free Electrocatalysts for the Oxygen Reduction Reaction, *Angew. Chem.* **2011**, *123*, 7270–7273.

[24] W. Wei, H. Liang, K. Parvez, X. Zhuang, X. Feng, K. Müllen, Nitrogen-Doped Carbon Nanosheets with Size-Defined Mesopores as Highly Efficient Metal-Free Catalyst for the Oxygen Reduction Reaction, *Angew. Chem.* **2014**, *126*, 1596–1600.

[25] Y. Jiang, P. Ni, C. Chen, Y. Lu, P. Yang, B. Kong, A. Fisher, X. Wang, Selective Electrochemical H_2O_2 Production through Two-Electron Oxygen Electrochemistry, *Adv. Energy Mater.* **2018**, *8*, 1801909.

[26] Y. Liu, X. Quan, X. Fan, H. Wang, S. Chen, High-Yield Electrosynthesis of Hydrogen Peroxide from Oxygen Reduction by Hierarchically Porous Carbon, *Angew. Chem.* **2015**, *127*, 6941–6945.

[27] H. Tamai, T. Kakii, Y. Hirota, T. Kumamoto, H. Yasuda, Synthesis of Extremely Large Mesoporous Activated Carbon and Its Unique Adsorption for Giant Molecules, *Chem. Mater.* **1996**, *8*, 454–462.

[28] J. de S. Macedo, N. B. da Costa Júnior, L. E. Almeida, E. F. da S. Vieira, A. R. Cestari, I. de F. Gimenez, N. L. Villarreal Carreño, L. S. Barreto, Kinetic and calorimetric study of the adsorption of dyes on mesoporous activated carbon prepared from coconut coir dust, *J. Colloid Interface Sci.* **2006**, *298*, 515–522.

[29] D. D. Asouhidou, K. S. Triantafyllidis, N. K. Lazaridis, K. A. Matis, S.-S. Kim, T. J. Pinnavaia, Sorption of reactive dyes from aqueous solutions by ordered hexagonal and disordered mesoporous carbons, *Microporous Mesoporous Mater.* **2009**, *117*, 257–267.

[30] X. Zhuang, Y. Wan, C. Feng, Y. Shen, D. Zhao, Highly Efficient Adsorption of Bulky Dye Molecules in Wastewater on Ordered Mesoporous Carbons, *Chem. Mater.* **2009**, *21*, 706–716.

[31] A. S. Sirotkin, L. Yu. Koshkina, K. G. Ippolitov, The BAC-process for treatment of waste water Containing non-ionogenic synthetic surfactants, *Water Res.* **2001**, *35*, 3265–3271.

[32] F. Karray, M. Mezghani, N. Mhiri, B. Djelassi, S. Sayadi, Scale-down studies of membrane bioreactor degrading anionic surfactants wastewater: Isolation of new anionic-surfactant degrading bacteria, *Int. Biodeterior. Biodegrad.* **2016**, *114*, 14–23.

[33] E. K. Putra, R. Pranowo, J. Sunarso, N. Indraswati, S. Ismadji, Performance of activated carbon and bentonite for adsorption of amoxicillin from wastewater: Mechanisms, isotherms and kinetics, *Water Res.* **2009**, *43*, 2419–2430.

[34] T. X. Bui, H. Choi, Adsorptive removal of selected pharmaceuticals by mesoporous silica SBA-15, *J. Hazard. Mater.* **2009**, *168*, 602–608.

[35] J. Schuster, G. He, B. Mandlmeier, T. Yim, K. T. Lee, T. Bein, L. F. Nazar, Spherical Ordered Mesoporous Carbon Nanoparticles with High Porosity for Lithium–Sulfur Batteries, *Angew. Chem. Int. Ed.* **2012**, *51*, 3591–3595.

[36] F. Xu, Z. Tang, S. Huang, L. Chen, Y. Liang, W. Mai, H. Zhong, R. Fu, D. Wu, Facile synthesis of ultrahigh-surface-area hollow carbon nanospheres for enhanced adsorption and energy storage, *Nat. Commun.* **2015**, *6*, 7221.

[37] G. Srinivas, V. Krungleviciute, Z.-X. Guo, T. Yildirim, Exceptional CO_2 capture in a hierarchically porous carbon with simultaneous high surface area and pore volume, *Energy Env. Sci* **2014**, *7*, 335–342.

[38] A. F. Strickland, W. S. Perkins, Decolorization of Continuous Dyeing Wastewater by Ozonation, *Text. Chem. Color.* **1995**, *27*, 11–15.

[39] A. Sadezky, H. Muckenhuber, H. Grothe, R. Niessner, U. Pöschl, Raman microspectroscopy of soot and related carbonaceous materials: Spectral analysis and structural information, *Carbon* **2005**, *43*, 1731–1742.

[40] M. Thommes, K. Kaneko, A. V. Neimark, J. P. Olivier, F. Rodriguez-Reinoso, J. Rouquerol, K. S. W. Sing, Physisorption of gases, with special reference to the evaluation of surface area and pore size distribution (IUPAC Technical Report), *Pure Appl. Chem.* **2015**, *87*, DOI 10.1515/pac-2014-1117.

[41] F. Rodríguez-Reinoso, M. Molina-Sabio, M. T. González, The use of steam and CO2 as activating agents in the preparation of activated carbons, *Carbon* **1995**, *33*, 15–23.

[42] L. G. Gurvich, *Zhurnal Rus. Fiz.-Khimicheskago Obshchestva* **1915**, 805–827.

[43] K. Y. Foo, B. H. Hameed, Insights into the modeling of adsorption isotherm systems, *Chem. Eng. J.* **2010**, *156*, 2–10.

[44] E. N. El Qada, S. J. Allen, G. M. Walker, Adsorption of Methylene Blue onto activated carbon produced from steam activated bituminous coal: A study of equilibrium adsorption isotherm, *Chem. Eng. J.* **2006**, *124*, 103–110.

[45] A. M. M. Vargas, A. L. Cazetta, M. H. Kunita, T. L. Silva, V. C. Almeida, Adsorption of methylene blue on activated carbon produced from flamboyant pods (Delonix regia): Study of adsorption isotherms and kinetic models, *Chem. Eng. J.* **2011**, *168*, 722–730.

[46] M. U. Dural, L. Cavas, S. K. Papageorgiou, F. K. Katsaros, Methylene blue adsorption on activated carbon prepared from Posidonia oceanica (L.) dead leaves: Kinetics and equilibrium studies, *Chem. Eng. J.* **2011**, *168*, 77–85.

[47] K. Mahmoudi, N. Hamdi, E. Srasra, Study of adsorption of methylene blue onto activated carbon from lignite, *Surf. Eng. Appl. Electrochem.* **2015**, *51*, 427–433.

[48] A. Wahby, J. M. Ramos-Fernández, M. Martínez-Escandell, A. Sepúlveda-Escribano, J. Silvestre-Albero, F. Rodríguez-Reinoso, High-Surface-Area Carbon Molecular Sieves for Selective CO2 Adsorption, *ChemSusChem* **2010**, *3*, 974–981.

[49] Z. Yang, Y. Xia, R. Mokaya, Enhanced Hydrogen Storage Capacity of High Surface Area Zeolite-like Carbon Materials, *J. Am. Chem. Soc.* **2007**, *129*, 1673–1679.

[50] Y. Zhu, S. Murali, M. D. Stoller, K. J. Ganesh, W. Cai, P. J. Ferreira, A. Pirkle, R. M. Wallace, K. A. Cychosz, M. Thommes, D. Su, E. A. Stach, R. S. Ruoff, Carbon-Based Supercapacitors Produced by Activation of Graphene, *Science* **2011**, *332*, 1537–1541.

[51] W. Chaikittisilp, K. Ariga, Y. Yamauchi, A new family of carbon materials: synthesis of MOF-derived nanoporous carbons and their promising applications, *J. Mater. Chem. A* **2013**, *1*, 14–19.

[52] Y. S. Yun, S. Y. Cho, J. Shim, B. H. Kim, S.-J. Chang, S. J. Baek, Y. S. Huh, Y. Tak, Y. W. Park, S. Park, H.-J. Jin, Microporous Carbon Nanoplates from Regenerated Silk Proteins for Supercapacitors, *Adv. Mater.* **2013**, *25*, 1993–1998.

[53] C. Pelekani, V. L. Snoeyink, A kinetic and equilibrium study of competitive adsorption between atrazine and Congo red dye on activated carbon: the importance of pore size distribution, *Carbon* **2001**, *39*, 25–37.

[54] Q. Li, V. L. Snoeyink, B. J. Mariñas, C. Campos, Pore blockage effect of NOM on atrazine adsorption kinetics of PAC: the roles of PAC pore size distribution and NOM molecular weight, *Water Res.* **2003**, *37*, 4863–4872.

[55] M. Arias, E. López, A. Nuñez, D. Rubinos, B. Soto, M. T. Barral, F. Díaz-Fierros, in *Eff. Miner.-Org.-Microorg. Interact. Soil Freshw. Environ.* (Eds.: J. Berthelin, P.M. Huang, J.-M. Bollag, F. Andreux), Springer US, Boston, MA, **1999**, pp. 361–365.

[56] P. Simoncic, T. Armbruster, Cationic methylene blue incorporated into zeolite mordenite-Na: a single crystal X-ray study, *Microporous Mesoporous Mater.* **2005**, *81*, 87–95.

[57] Y. Sun, I. Sinev, W. Ju, A. Bergmann, S. Dresp, S. Kühl, C. Spöri, H. Schmies, H. Wang, D. Bernsmeier, B. Paul, R. Schmack, R. Kraehnert, B. Roldan Cuenya, P. Strasser, Efficient Electrochemical Hydrogen Peroxide Production from Molecular Oxygen on Nitrogen-Doped Mesoporous Carbon Catalysts, *ACS Catal.* **2018**, *8*, 2844–2856.

[58] T.-P. Fellinger, F. Hasché, P. Strasser, M. Antonietti, Mesoporous Nitrogen-Doped Carbon for the Electrocatalytic Synthesis of Hydrogen Peroxide, *J. Am. Chem. Soc.* **2012**, *134*, 4072–4075.

[59] F. Hasché, M. Oezaslan, P. Strasser, T.-P. Fellinger, Electrocatalytic hydrogen peroxide formation on mesoporous non-metal nitrogen-doped carbon catalyst, *J. Energy Chem.* **2016**, *25*, 251–257.

[60] A. Verdaguer-Casadevall, D. Deiana, M. Karamad, S. Siahrostami, P. Malacrida, T. W. Hansen, J. Rossmeisl, I. Chorkendorff, I. E. L. Stephens, Trends in the Electrochemical Synthesis of H_2O_2: Enhancing Activity and Selectivity by Electrocatalytic Site Engineering, *Nano Lett.* **2014**, *14*, 1603–1608.

[61] W. Ding, Z. Wei, S. Chen, X. Qi, T. Yang, J. Hu, D. Wang, L.-J. Wan, S. F. Alvi, L. Li, Space-Confinement-Induced Synthesis of Pyridinic- and Pyrrolic-Nitrogen-Doped Graphene for the Catalysis of Oxygen Reduction, *Angew. Chem.* **2013**, *125*, 11971–11975.

[62] T. Najam, S. S. A. Shah, W. Ding, J. Jiang, L. Jia, W. Yao, L. Li, Z. Wei, An Efficient Anti-poisoning Catalyst against SOx, NOx, and POx: P, N-Doped Carbon for Oxygen Reduction in Acidic Media, *Angew. Chem.* **2018**, *130*, 15321–15326.

[63] H. Liu, J. Li, X. Xu, F. Wang, J. Liu, Z. Li, J. Ji, Highly graphitic carbon black-supported platinum nanoparticle catalyst and its enhanced electrocatalytic activity for the oxygen reduction reaction in acidic medium, *Electrochim. Acta* **2013**, *93*, 25–31.

[64] B. H. J. Bielski, D. E. Cabelli, in *Act. Oxyg. Chem.* (Eds.: C.S. Foote, J.S. Valentine, A. Greenberg, J.F. Liebman), Springer Netherlands, Dordrecht, **1995**, pp. 66–104.

[65] H. J. H. Fenton, LXXIII.—Oxidation of tartaric acid in presence of iron, *J. Chem. Soc. Trans.* **1894**, *65*, 899–910.

[66] A. Xu, X. Li, S. Ye, G. Yin, Q. Zeng, Catalyzed oxidative degradation of methylene blue by in situ generated cobalt (II)-bicarbonate complexes with hydrogen peroxide, *Appl. Catal. B Environ.* **2011**, *102*, 37–43.

[67] L. Cheng, M. Wei, L. Huang, F. Pan, D. Xia, X. Li, A. Xu, Efficient H_2O_2 Oxidation of Organic Dyes Catalyzed by Simple Copper(II) Ions in Bicarbonate Aqueous Solution, *Ind. Eng. Chem. Res.* **2014**, *53*, 3478–3485.

[68] G. Fang, C. Liu, J. Gao, D. Zhou, New Insights into the Mechanism of the Catalytic Decomposition of Hydrogen Peroxide by Activated Carbon: Implications for Degradation of Diethyl Phthalate, *Ind. Eng. Chem. Res.* **2014**, *53*, 19925–19933.

[69] A. Asghar, A. A. Abdul Raman, W. M. A. Wan Daud, Advanced oxidation processes for in-situ production of hydrogen peroxide/hydroxyl radical for textile wastewater treatment: a review, *J. Clean. Prod.* **2015**, *87*, 826–838.

[70] M. Panizza, A. Barbucci, R. Ricotti, G. Cerisola, Electrochemical degradation of methylene blue, *Sep. Purif. Technol.* **2007**, *54*, 382–387.

Appendix, the Supporting Information for Chapter 3

Experimental

Procedure for mesoporous N-doped carbon synthesis

Manganese acetate tetrahydrate ($Mn(CH_3CHOO)_2.4H_2O$, 99% purity, Sigma-Aldrich) (613 mg, 2.5 mmol, 1 equiv), nitrilotriacetic acid (NTA) ($N(CH_2COOH)_3$, 99% purity, Alfa-Aesar) (483 mg, 2.5 mmol, 1 equiv) and water (30 mL) were mixed in a 50 mL stainless steel autoclave with Teflon insert. Subsequently, the reaction was stirred (650 rpm) and heated to 180 °C for 6 hours, resulting in a pinkish white precipitate. The precipitate was collected by centrifugation. Thereafter the sample was washed eight times, alternating between ethanol (40 mL) and water (40 mL). The now white slurry was dried *in vacuo* at 70 °C for at least 18 hours. After grinding the white solid to a powder, it was transferred to a quartz tube and pyrolyzed at 900 °C in a N_2 atmosphere for 1h (heating rate $10°Cmin^{-1}$, N_2 flow 150 $mLmin^{-1}$). The resulting MnO/NC was washed with 0.5 M HCl at 80 °C for 4 hours and a second time at rt overnight. From start to finish, the yield of the reaction was ±5%.

Materials characterization

X-ray diffraction (XRD) patterns were measured with a Miniflex II diffractometer equipped with CuKα radiation, where the X-ray tube operated at 30 kV with a current of 5 mA. Nitrogen adsorption isotherms were measured with a Thermo Scientific Surfer instrument at 77K. Before analysis, the sample was dried in vacuum (10^{-3} mbar) at 200 °C for 3 h. Mercury intrusion porosimetry was performed on a Ce Instruments Pascal 440 measuring up to 400 MPa at ambient temperature. Samples were pretreated in a similar fashion to the nitrogen adsorption samples. Scanning electron microscopy (SEM, FEI Verios 460 with ETD detector) and transmission electron microscopy (TEM, JEOL 2200 FS TEM) were used to characterize the morphology. For X-ray photoelectron spectroscopy (XPS) a Kratos AXIS instrument equipped with monochromatic Al Kα X-ray source was used and the base pressure in the analytical chamber was 10^{-9} mbar. Raman spectra were measured using a Renishaw InVia system (532 nm and

632.8nm) and a Kaisar Optical Systems RXN-4 system (785 nm) coupled with fiber optics to an immersion probe with a short focal length. UV-Vis measurements were performed on a Varian Cary 50 bio UV-Visible spectrophotometer with plastic cuvettes.

Procedure for methylene blue adsorption on carbons

First a 1000 ppm methylene blue (MB) stock solution was prepared by dissolving MB (1.00 gr) in DI water (1.0 L). For the adsorption isotherm, the stock solution was diluted to batches containing 25, 50, 75, 100, 150, 200 and 300 ppm MB, which were adjusted to pH 4 with 0.1 M HCl. 5 mg of either NC or Norit Darco was added to 25 mL of the batches and the resulting suspensions were agitated overnight on a roller mixer. The suspension were filtered with a 0.45 μm filter to remove the adsorbate and the resulting MB solution was diluted till the UV-Vis absorbance at 290 nm was < 2. The concentration of MB was determined using a calibration curve prepared by diluting the MB stock solution to 2, 4, 6, 8, 10, 12 and 14 ppm and using a linear fit of the peak at 290 nm. The MB concentration in solution after adsorption (C_e) was determined by multiplying the UV-Vis calculated concentration by the dilution factor used for preparing the UV-Vis sample. Subsequently, the value of amount of MB adsorbed on the adsorbate (q_e) was determined by subtracting the value of *Ce* from the initial concentration of the solution.

Electrochemical procedures

Catalyst inks were prepared by suspending 1 mg catalyst powder in 1 mL ethanol and 10 μL Nafion® (D-521 dispersion 5 wt% in water/isopropanol) and sonication overnight. The Rotating Ring Disk Electrode (RRDE) working electrode tip (glassy carbon disk 0.2475 cm^{-2}, platinum ring 0.1866 cm^{-2}) was polished with diamond polishing film containing 0.1 μm particles and rinsed with water afterwards. The working electrode was prepared by drop casting 6 × 5 μL ink, while air drying between casts. 20 wt% Pt on Vulcan XC-72 was used for the Pt/C standard.

Electrochemical experiments were performed in a 3-electrode glass cell, with a 0.1 M $HClO_4$ electrolyte. All electrochemical experiments were performed under 25 °C. A bipotentiostat setup was made by connecting two Gamry Reference 600 potentiostats together in conjunction with a Gamry RDE710 Rotating Electrode setup. A saturated calomel electrode (SCE) was used as a reference electrode,

separated from the solution with a luggin capillary. Potentials were reported vs RHE by adding 0.3001 V (pH = 1) to the measured SCE potential. A graphite rod was used as a counter electrode, presoaked with the electrolyte 24 hours prior to the measurements. Either nitrogen or oxygen was bubbled through the solution for a minimum of 30 min, where after the gas was flown over the solution (gas blanket). Prior to the experiments the solution resistance was measured and 95% of this value was used as a positive correction factor in an automatic iR drop correction. Before measurements, cyclic voltammograms were recorded from 0.05 to 1.20 V vs RHE till no change in current was visible. RRDE measurements were performed by keeping a constant potential of 1.2 V vs RHE on the ring, while sweeping the potential on the disk from 0.05 V to 1.2 V vs RHE at a rotation of 1600 rpm and a scan rate of 10 mVs^{-1}. The contribution of the capacitance was corrected for by subtracting the average current in the potential window of 0.8-1.0 V vs RHE.

The poisoning effect of MB was studied by first measuring the electrochemical performance as stated above in 200 mL oxygen saturated 0.1 M $HClO_4$. Subsequently, 5 mg of MB was added to the electrolyte and dissolved by stirring for 30 min, creating a 25 ppm MB solution (The solubility of MB is highly reduced in the electrolyte). Subsequent measurements were performed in a similar fashion as stated above.

The H_2O_2 selectivity was calculated from the ratio between the recorded ring and disk current, according to equation (S3.1):

$$H_2O_2\% = \frac{200 I_{ring}}{N|I_{disk}| + I_{ring}} \quad \text{(S3.1)}$$

where the collection efficiency (N) determined from an RRDE experiment with $[Fe(CN)_6]^{4-}/[Fe(CN)_6]^{3-}$

Adsorption isotherm models

Langmuir isotherm model

The Langmuir isotherm model assumes a homogenous adsorption of adsorbate on the adsorbent surface. Therefore, adsorption sites are equal and always available. The model is described by eq S3.2, with q_e being the amount of adsorbate adsorbed on the adsorbent (mg g^{-1}) at equilibrium, Q being an energy term most often equal to unity, C_e being the adsorbate concentration in the liquid (mg dm^{-3}) at equilibrium and K_L (dm^3g^{-1}) and a_L (dm^3mg^{-1}) being one of the

Langmuir constants. A linearized version of this model (eq S3.3) is used to calculate the Langmuir constants from the intercept and slope of the graph. The Langmuir isotherm model can also be used to indicate if the adsorption is favorable or unfavorable with the dimensionless separation constant R_L. This constant is defined by eq S3.4 in which C_o is the initial dye concentration in solution and K_L is the Langmuir constant. An unfavorable adsorption is indicated by $R_L>1$, while a favorable adsorption is indicated by $0<R_L<1$. Furthermore, irreversible adsorption is indicated by $R_L=0$ and a linear adsorption by $R_L=1$.

$$q_e = \frac{QK_LC_e}{1+(a_LC_e)} \quad \text{(S3.2)}$$

$$\frac{C_e}{q_e} = \frac{1}{K_L} + \frac{a_L}{K_L}C_e \quad \text{(S3.3)}$$

$$R_L = \frac{1}{1+K_LC_o} \quad \text{(S3.4)}$$

Freundlich isotherm model

The Freundlich isotherm model assumes a multilayer adsorption on a heterogeneous surface. The adsorption sites are not equal in energy and adsorption occurs first on the most favorable sites. The model is described by eq S3.5, with q_e being the amount of adsorbate adsorbed on the adsorbent ($mg \cdot g^{-1}$) at equilibrium, K_F being the Freundlich constant, C_e being the adsorbate concentration in the liquid ($mgdm^{-3}$) at equilibrium and n being the heterogeneity factor. Eq S3.6 gives a linearized version of this model, which is used to calculate the Langmuir constants from the intercept and slope of the graph.

$$q_e = K_F C_e^{\frac{1}{n}} \quad \text{(S3.5)}$$

$$\ln q_e - \ln K_F = \frac{1}{n}\ln C_e \quad \text{(S3.6)}$$

Redlich-Peterson isotherm model

The Redlich-Peterson isotherm model is a hybrid between the Langmuir and Freundlich isotherm models. It usually displays a similarity with the Langmuir isotherm model at low concentrations, while being more similar to the Freundlich model at high concentrations. The model is described by eq S3.7, with q_e being the amount of adsorbate adsorbed on the adsorbent ($mg \cdot g^{-1}$) at equilibrium, K_r being the modified Langmuir constant, C_e being the adsorbate concentration in the liquid ($mgdm^{-3}$) at equilibrium and a_r and β being constants. Eq S3.8 gives

linearized version of this model, which is used to calculate the constants. However, the inclusion of three unknown variables in eq S8 makes solving the equation impossible. For simplicity, $K_R = K_L$ (Langmuir constant), which results in an equation with two variables.

$$q_e = \frac{K_R C_e}{1+(a_R C_e^g)} \quad \text{(S3.7)}$$

$$\ln\left(\frac{K_r C_e}{q_e} - 1\right) = g \ln C_e + \ln a_R \quad \text{(S3.8)}$$

Supplementary Figures

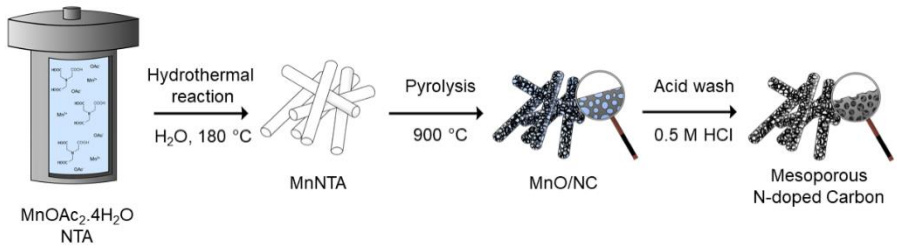

Figure S3.1*. A schematic representation of the synthesis of the MnNTA precursor and the final NC nanotubes.*

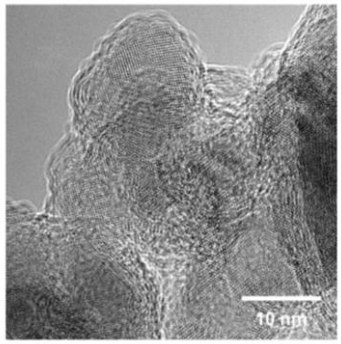

Figure S3.2. *The uncolored version of Figure 2e.*

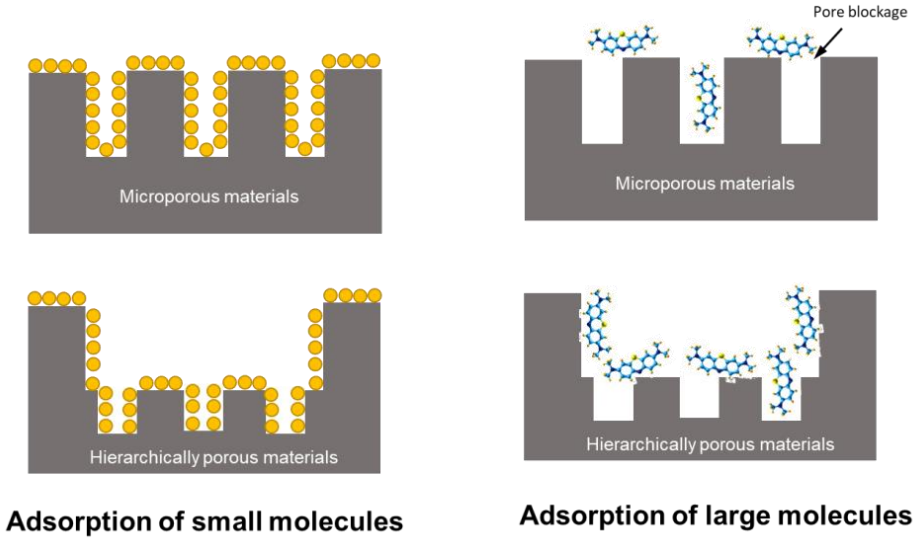

Figure S3.3. *Schematic representation of small molecules and large molecules in micro- and mesopores. Large molecules block micropores when they adsorb on the edge of the pore, decreasing the overall adsorption of the molecules.*

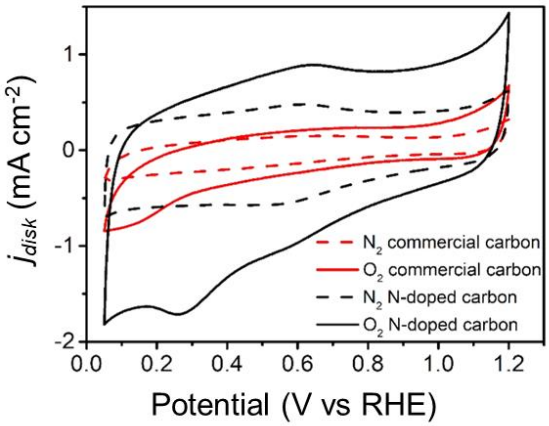

Figure S3.4. *The cyclic voltammograms of the NC and commercial carbon in N_2 (scan rate of 10 mVs^{-1}) and O_2 (scan rate of 20 mVs^{-1}) saturated 0.1 M HClO4 electrolyte.*

Supplementary Tables

Table S3.1. Overview of H_2O_2 selective metal-free carbon based materials

Entry	Material	Electrolyte	Onset potential	H_2O_2 selectivity	Ref.
1	MOF-5 derived Carbon	0.05 M H_2SO_4 + 0.05 M Na_2SO_4	0.42 V v RHE	>90%	[A1]
2	Ionic liquid modified MCK-3	0.5 M H_2SO_4	0.44 V v RHE	83%	[A2]
3	Silica template with BMP-dca Carbon	0.1 M $HClO_4$	0.55 V v RHE	>95%	[A3]
4	Silica template with BMP-dca Carbon	0.1 M $KClO_4$	0.62 V v RHE	<30%	[A4]
5	Silica template with heteroaromatics Carbon	0.5 M H_2SO_4	0.38 V v RHE	76%	[A5]
6	Pd-Hg/C	0.1 M $HClO_4$	±0.7 V v RHE	95%	[A6]
7	Pt/Hg	0.1 M $HClO_4$	0.6 V v RHE	96%	[A7]
This work	MnNTA derived	0.1 M $HClO_4$	±0.7 V v RHE	>98%	-

Table S3.2. High surface area and/or pore volume carbon materials reported in literature

Journal	Material	Pore volume (cm^3g^{-1})	BET Surface area (cm^2g^{-1})	Ref
1	Spherical mesoporous carbon nanoparticles	2.32	2445	[A8]
2	Tomato processing solid waste derived carbon	1.57	1093	[A9]
3	Hollow carbon nanospheres	2.43	3022	[A10]
4	Coconut shell derived carbon	2.1	2141	[A11]
5	Activated graphene	2.14	2995	[A12]
6	MOF-5 derived carbon	5.53	2734	[A13]
7	Nitrogen doped carbon nanosheets	1.52	589	[A14]
8	Ordered mesoporous carbon fiber	1.21	1345	[A15]
9	Zn,Co-ZIF derived carbon	1.52	1170	[A16]
10	Peapodlike carbon	4.69	977	[A17]
11	MC22	4.8	1175	[A18]
12	Hexagonally ordered mesostructured carbon	1.3	1520	[A19]
13	Mesoporous carbon spheres	3.5	1321	[A20]
14	Ordered mesoporous few-layer carbon	2.2	1580	[A21]
15	Mesoporous carbon spheres between reduced graphene oxide sheets	3.36	1496	[A22]
16	Mesoporous carbon interlayers	3.23	900	[A23]
17	Silica templated carbon	3.6	1512	[A24]
18	Bimodal mesoporous carbon	2.0	2300	[A25]
19	Magnesium citrate	2.9	1432	[A26]

Table S3.3. Parameters derived from the Linearized Langmuir, Freundlich and Redlich-Peterson isotherm models

Sample	**Langmuir**			
	K_L $dm^3\ g^{-1}$	a_L $dm^3 mg^{-1}$	Q $mg \cdot g^{-1}$	r^2
Mn-NC	357.14	0.9586	385	0.999
Norit Darco	123.46	0.4691	263	0.998
Sample	**Freundlich**			
	r^2	K_F $mg \cdot g^{-1} / (dm^3 g^{-1})^n$	n	r^2
Mn-NC	0.999	228.77	8.52	0.9117
Norit Darco	0.998	161.71	9.74	0.9468
Sample	**Redlich-Peterson**			**R_L**
	β	a_r $dm^3 g^{-1}$	r^2	
Mn-NC	0.9863	0.9931	0.998	$6E^{-6}$
Norit Darco	0.9936	0.4801	0.999	$2E^{-5}$

Additional references

[A1] Y. Liu, X. Quan, X. Fan, H. Wang, S. Chen, High-Yield Electrosynthesis of Hydrogen Peroxide from Oxygen Reduction by Hierarchically Porous Carbon, *Angew. Chem.* **2015**, *127*, 6941–6945.

[A2] Y. Sun, I. Sinev, W. Ju, A. Bergmann, S. Dresp, S. Kühl, C. Spöri, H. Schmies, H. Wang, D. Bernsmeier, B. Paul, R. Schmack, R. Kraehnert, B. Roldan Cuenya, P. Strasser, Efficient Electrochemical Hydrogen Peroxide Production from Molecular Oxygen on Nitrogen-Doped Mesoporous Carbon Catalysts, *ACS Catal.* **2018**, *8*, 2844–2856.

[A3] T.-P. Fellinger, F. Hasché, P. Strasser, M. Antonietti, Mesoporous Nitrogen-Doped Carbon for the Electrocatalytic Synthesis of Hydrogen Peroxide, *J. Am. Chem. Soc.* **2012**, *134*, 4072–4075.

[A4] F. Hasché, M. Oezaslan, P. Strasser, T.-P. Fellinger, Electrocatalytic hydrogen peroxide formation on mesoporous non-metal nitrogen-doped carbon catalyst, *J. Energy Chem.* **2016**, *25*, 251–257.

[A5] V. Perazzolo, C. Durante, R. Pilot, A. Paduano, J. Zheng, G. A. Rizzi, A. Martucci, G. Granozzi, A. Gennaro, Nitrogen and sulfur doped mesoporous carbon as metal-free electrocatalysts for the in situ production of hydrogen peroxide, *Carbon* **2015**, *95*, 949–963.

[A6] A. Verdaguer-Casadevall, D. Deiana, M. Karamad, S. Siahrostami, P. Malacrida, T. W. Hansen, J. Rossmeisl, I. Chorkendorff, I. E. L. Stephens, Trends in the Electrochemical Synthesis of H_2O_2: Enhancing Activity and Selectivity by Electrocatalytic Site Engineering, *Nano Lett.* **2014**, *14*, 1603–1608.

[A7] S. Siahrostami, A. Verdaguer-Casadevall, M. Karamad, D. Deiana, P. Malacrida, B. Wickman, M. Escudero-Escribano, E. A. Paoli, R. Frydendal, T. W. Hansen, I. Chorkendorff, I. E. L. Stephens, J. Rossmeisl, Enabling direct H2O2 production through rational electrocatalyst design, *Nat. Mater.* **2013**, *12*, 1137–1143.

[A8] J. Schuster, G. He, B. Mandlmeier, T. Yim, K. T. Lee, T. Bein, L. F. Nazar, Spherical Ordered Mesoporous Carbon Nanoparticles with High Porosity for Lithium–Sulfur Batteries, *Angew. Chem. Int. Ed.* **2012**, *51*, 3591–3595.

[A9] H. Sayğılı, F. Güzel, High surface area mesoporous activated carbon from tomato processing solid waste by zinc chloride activation: process optimization, characterization and dyes adsorption, *J. Clean. Prod.* **2016**, *113*, 995–1004.

[A10] F. Xu, Z. Tang, S. Huang, L. Chen, Y. Liang, W. Mai, H. Zhong, R. Fu, D. Wu, Facile synthesis of ultrahigh-surface-area hollow carbon nanospheres for enhanced adsorption and energy storage, *Nat. Commun.* **2015**, *6*, 7221.

[A11] A. Jain, R. Balasubramanian, M. P. Srinivasan, Production of high surface area mesoporous activated carbons from waste biomass using hydrogen peroxide-mediated hydrothermal treatment for adsorption applications, *Chem. Eng. J.* **2015**, *273*, 622–629.

[A12] Y. You, W. Zeng, Y.-X. Yin, J. Zhang, C.-P. Yang, Y. Zhu, Y.-G. Guo, Hierarchically micro/mesoporous activated graphene with a large surface area for high sulfur loading in Li–S batteries, *J. Mater. Chem. A* **2015**, *3*, 4799–4802.

[A13] G. Srinivas, V. Krungleviciute, Z.-X. Guo, T. Yildirim, Exceptional CO_2 capture in a hierarchically porous carbon with simultaneous high surface area and pore volume, *Energy Env. Sci* **2014**, *7*, 335–342.

[A14] W. Wei, H. Liang, K. Parvez, X. Zhuang, X. Feng, K. Müllen, Nitrogen-Doped Carbon Nanosheets with Size-Defined Mesopores as Highly Efficient Metal-Free Catalyst for the Oxygen Reduction Reaction, *Angew. Chem.* **2014**, *126*, 1596–1600.

[A15] H. Wang, C. Zhang, Z. Chen, H. K. Liu, Z. Guo, Large-scale synthesis of ordered mesoporous carbon fiber and its application as cathode material for lithium–sulfur batteries, *Carbon* **2015**, *81*, 782–787.

[A16] L. Shang, H. Yu, X. Huang, T. Bian, R. Shi, Y. Zhao, G. I. N. Waterhouse, L.-Z. Wu, C.-H. Tung, T. Zhang, Well-Dispersed ZIF-Derived Co,N-Co-doped Carbon Nanoframes through Mesoporous-Silica-Protected Calcination as Efficient Oxygen Reduction Electrocatalysts, *Adv. Mater.* **2016**, *28*, 1668–1674.

[A17] D. Li, F. Han, S. Wang, F. Cheng, Q. Sun, W.-C. Li, High Sulfur Loading Cathodes Fabricated Using Peapodlike, Large Pore Volume Mesoporous Carbon for Lithium–Sulfur Battery, *ACS Appl. Mater. Interfaces* **2013**, *5*, 2208–2213.

[A18] X. Li, Y. Cao, W. Qi, L. V. Saraf, J. Xiao, Z. Nie, J. Mietek, J.-G. Zhang, B. Schwenzer, J. Liu, Optimization of mesoporous carbon structures for lithium–sulfur battery applications, *J. Mater. Chem.* **2011**, *21*, 16603.

[A19] S. Jun, S. H. Joo, R. Ryoo, M. Kruk, M. Jaroniec, Z. Liu, T. Ohsuna, O. Terasaki, Synthesis of New, Nanoporous Carbon with Hexagonally Ordered Mesostructure, *J. Am. Chem. Soc.* **2000**, *122*, 10712–10713.

[A20] Q. Li, R. Jiang, Y. Dou, Z. Wu, T. Huang, D. Feng, J. Yang, A. Yu, D. Zhao, Synthesis of mesoporous carbon spheres with a hierarchical pore structure for the electrochemical double-layer capacitor, *Carbon* **2011**, *49*, 1248–1257.

[A21] T. Lin, I.-W. Chen, F. Liu, C. Yang, H. Bi, F. Xu, F. Huang, Nitrogen-doped mesoporous carbon of extraordinary capacitance for electrochemical energy storage, *Science* **2015**, *350*, 1508–1513.

[A22] Z. Lei, N. Christov, X. S. Zhao, Intercalation of mesoporous carbon spheres between reduced graphene oxide sheets for preparing high-rate supercapacitor electrodes, *Energy Environ. Sci.* **2011**, *4*, 1866.

[A23] J. Balach, T. Jaumann, M. Klose, S. Oswald, J. Eckert, L. Giebeler, Mesoporous Carbon Interlayers with Tailored Pore Volume as Polysulfide Reservoir for High-Energy Lithium–Sulfur Batteries, *J. Phys. Chem. C* **2015**, *119*, 4580–4587.

[A24] S. Han, T. Hyeon, Simple silica-particle template synthesis of mesoporous carbons, *Chem. Commun.* **1999**, 1955–1956.

[A25] G. He, X. Ji, L. Nazar, High "C" rate Li-S cathodes: sulfur imbibed bimodal porous carbons, *Energy Environ. Sci.* **2011**, *4*, 2878.

[A26] J. Wang, Y. Wu, Z. Shi, C. Wu, Mesoporous carbon with large pore volume and high surface area prepared by a co-assembling route for Lithium-Sulfur Batteries, *Electrochim. Acta* **2014**, *144*, 307–314.

Chapter 4

Waste Prevention – a Palladium and Cuprous Oxide Nanocluster Assembly for Electroless Copper Deposition

To effectively manipulate the electronic structure of the catalysts, we present here a simple bottom-up synthesis protocol for agglomerating palladium and cuprous oxide ultrasmall nanoclusters into single nanoparticles, forming so-called quantum dot assemblies (QDAs). Our synthesis is based on the galvanic displacement of copper with palladium cations at O_2-free conditions, rendering the simultaneous and unique crystal growth of ~3 nm Cu_2O and Pd clusters. Such assemblies, comprising ultrasmall nano-constitutes, offer much more phase boundaries, where the interfacial electronic effect becomes prominent in catalysis. This is demonstrated in the electrocatalytic oxidation of formaldehyde, ethanol and glucose. In all three cases, the QDA catalyst, despite its lower Pd loading, outperforms the monometallic palladium catalyst. Indeed, complementing the experimental results with density-functional theory calculations, we could confirm the sharply increased charge density at the Pd-Cu heterojunction and the decreased energy barrier of the formaldehyde oxidation on the QDA catalyst. Finally, we applied these catalysts in electroless copper deposition – an industrially relevant process for the manufacturing of printed circuit boards. The QDA catalysts gave uniform and robust copper wires at a rate that was three times faster than the monometallic Pd catalyst, showing their potential for real-life applications.

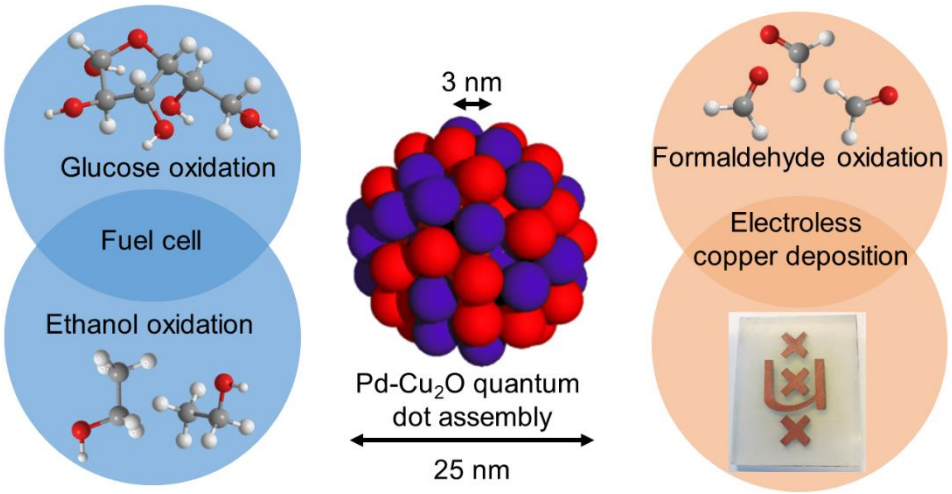

Parts of this chapter have been published as J. Biemolt, D. van Noordenne, J. Liu, E. Antonetti, M. Leconte, S. van Vliet, R. Bliem, G. Rothenberg, X.-Z. Fu, N. Yan, Assembling Palladium and Cuprous Oxide Nanoclusters into Single Quantum Dots for the Electrocatalytic Oxidation of Formaldehyde, Ethanol, and Glucose, *ACS Appl. Nano Mater.* **2020**, *3*, 10176–10182.

Introduction

Engineering the topology of catalysts on the nano-scale is one of the most effective approaches of optimizing their catalytic performance. It allows the construction of hybrid systems comprising different components within the same nanostructure.[1–5] Such assemblies can result in the formation of optimized active sites thanks to the physical and chemical interactions of constituent components. The synergistic effect is often prominent at the interface, where the electronic and geometric interactions start affecting one another.[6–8] Thus, creating more these boundaries can be beneficial for catalysis.

Intuitively, decreasing the size of the nanoclusters in the assemblies will create more interfaces. In particular, when the clusters become small enough to be considered as quantum dots (d < 3 nm, also called ultrasmall nanoparticles), quantum effects start influencing the catalytic properties significantly.[9–13] There are various ways for making nanoclusters. Based on the pioneering work by LaMer and Dinegar,[14] monodispersed nanoclusters are produced by controlling the different colloidal growth-phases. Surfactants are typically used to influence these growth-phases, offering control over the particle size, shape and crystal structure. This can yield well-defined and highly active catalysts.[15–18] Alternatively, one can also use physical methods such as atomic layer deposition or vapor phase deposition.[19,20] These gas-based methods give even better control over the final catalyst structure.[21–23] They are excellent for lab-scale catalyst synthesis, and are often used for making model catalysts for fundamental studies. But the high cost hinders their practical application in industry.

Notwithstanding the progress in the nanocluster synthesis, hybridizing multiple types of nanoclusters to form a quantum dot assemblies (QDAs) remains a difficult challenge. Now, motivated by the prospect of strengthening the interfacial electronic effect in such assemblies, we show that simple galvanic displacement is an effective approach for making QDAs. In the literature, this method is often used to grow conventional nanostructures such as the core-shell, dumbbell, nanotubes, and nanospheres.[24–27] There, structure dimensions are typically larger than 50 nm. By taking advantage of the competing crystal growth of the Cu_2O and Pd, we succeeded in preventing the overgrowth of the two types of nuclei. The resulting quantum dots of Cu_2O and Pd are both *ca.* 3nm in diameter, agglomerating into QDAs of 10–25 nm. Thanks to the maximized interfacial electronic effect as supported by the simulation results, our Cu_2O-Pd

QDAs are excellent catalysts for the electrooxidation of small organics (formaldehyde, glucose and ethanol), outperforming even pure Pd nanoparticles. In the electroless copper deposition process, which is industrially relevant for the fabrication of printed circuit boards (PCBs),[28,29] the new catalysts accelerate the deposition rate three-fold, promoting the growth of robust copper wires on flexible substrates. The fact that our method uses only water as the solvent, without any additive, increases the opportunities for industrial applications.

Results and Discussion

The geometric structure and the synthetic strategy of Cu_2O/Pd quantum dot assemblies (QDAs) are illustrated in Figure 4.1. After obtaining the copper nanoparticles (8 wt.%) supported on Vulcan XC-72R, QDAs were synthesized through the galvanic displacement reaction shown in eq 4.1 with the absence of O_2 (see the supporting information for details). The redox potential difference between palladium and copper (eqs 4.2 and 4.3) results in copper oxidation and Pd^{2+} reduction. Usually, the copper atoms would be oxidized following a two-electron process all the way to soluble Cu^{2+} cations. In our system, however, the reaction gives insoluble Cu_2O (eq 4.4) as the reaction took place in O_2-free environment.[30] The palladium and the cuprous oxide particles grow

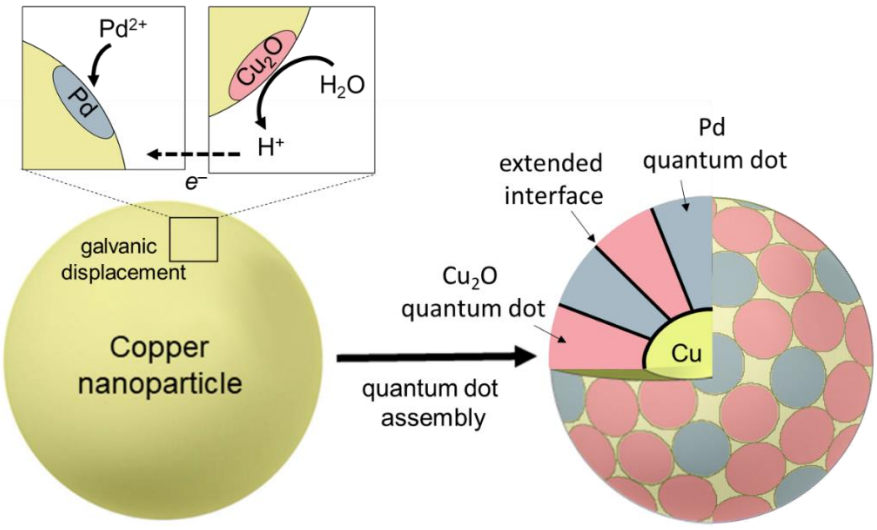

Figure 4.1. *Schematic illustration of the growth and configuration of a Pd and Cu_2O quantum dot assembly (QDA).*

simultaneously during the galvanic displacement (as illustrated in Figure 1 and eq 1). Each phase inhibits the growth of the other in its vicinity, resulting in the formation of ultrasmall nano-domains on the native Cu nanoparticle.

$$2Cu^0 + 2OH^- + Pd^{2+} \rightarrow Cu_2O + H_2O + Pd^0 \qquad E^o = +1.275\ V \qquad (4.1)$$

$$Cu^{2+} + 2e^- \rightarrow Cu^0 \qquad E^o = +0.342\ V \qquad (4.2)$$

$$Pd^{2+} + 2e^- \rightarrow Pd^0 \qquad E^o = +0.915\ V \qquad (4.3)$$

$$Cu_2O + H_2O + 2e^- \rightarrow 2Cu^0 + 2OH^- \qquad E^o = -0.360\ V \qquad (4.4)$$

We then varied the size and number of the nanoclusters in the Pd-Cu_2O QDAs, to optimize their catalytic activity. Our hypothesis was that using low concentration of palladium solution during galvanic displacement would give less Pd and more Cu_2O clusters, and *vice versa*. Thus, we prepared QDAs with different Pd:Cu mass ratios (0.2:8, 0.5:8, 1:8, 2:8 and 5:8) from the same Cu/C (8wt% Cu loading) and varying amounts of palladium in the solution during galvanic displacement. The five catalysts are denoted using their Pd:Cu percentage mass ratios subscripted before the element symbol (e.g., $_{0.2}$Pd-$_8$Cu/C refers to a QDA with 0.2 wt% palladium and 8 wt% copper supported on Vulcan). Additional monometallic palladium catalysts (Pd/C) were prepared as control samples.

X-ray diffraction (XRD) was used to determine the bulk crystal phases of the Pd-Cu/C, Pd/C and Cu/C catalysts. Figure 2a shows the diffraction patterns of the $_5$Pd-$_8$Cu/C, $_5$Pd/C and $_8$Cu/C catalysts (for clarity and brevity, we discuss here only the XRD of $_5$Pd-$_8$Cu/C; other results are shown in Figure S4.1 in the Supporting Information). The $_5$Pd-$_8$Cu sample shows the characteristic peaks of Cu_2O (36.6° (111) and 42.5° (200), COD 1000063), while no Pd peaks are

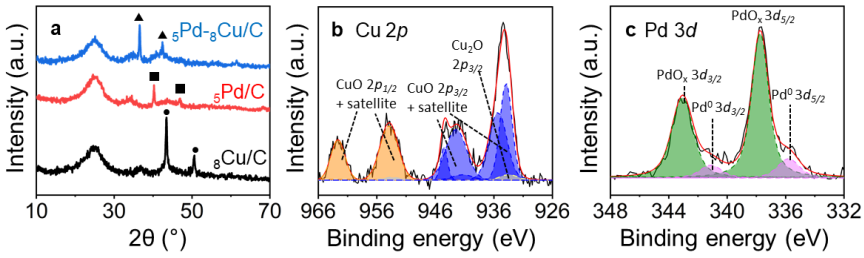

Figure 4.2. *a) XRD spectra of $_8$Cu/C, $_5$Pd/C and $_5$Pd-$_8$Cu/C with ● Cu, ▲ Cu_2O and ■ Pd; b) deconvoluted Cu 2p XPS spectrum of $_5$Pd-$_8$Cu/C; c) deconvoluted Pd 3d XPS spectrum of $_5$Pd-$_8$Cu/C; the red lines are the spectral envelopes.*

observed. This pertains to the formation of ultrasmall Pd nanoparticles, these local structures of the catalyst were further examined using other techniques (*vide infra*). Only peaks for metallic copper (43.5° (111) and 50.7° (200), COD 9011604) are observed in the diffractogram of the $_{8}$Cu/C catalyst, showing that the cuprous oxide in the Pd-Cu/C QDAs formed during the galvanic displacement, and not by air oxidation. The control catalyst $_{5}$Pd/C shows peaks for metallic Pd (40.2° (111) and 46.8° (200), COD 1011106).

Further insight of the surface composition was gained via X-ray photoelectron spectroscopy (XPS) performed *ex situ* on $_{5}$Pd-$_{8}$Cu/C QDA. The Cu 2*p* and Pd 3*d* spectra of the $_{5}$Pd-$_{8}$Cu/C QDA are shown in Figure 4.2b and 4.2c, and are used for the chemical interpretation.[31–33] The Cu $2p_{3/2}$ peak suggests that the sample surface is rich in Cu^{2+} oxide, as shown by the peak position and the characteristic strong satellite peaks. The peak at 933 eV (grey in Figure 4.2b) was assigned to the Cu^{1+} oxide which accounts for approximately 2.6% of the sample volume probed by XPS. The discrepancy between the XRD and XPS results is attributed to the oxygen spillover from Pd to Cu_2O on the materials surface when the catalyst is exposed to air for a long period of time. This hypothesis was supported by the Pd 3*d* peak, showing 86% palladium oxide and 14% metallic palladium (Figure 4.2c, green and pink peaks respectively). A palladium to copper ratio of 0.72:1 was determined in the $_{5}$Pd-$_{8}$Cu/C QDA using the Pd 3*d* and Cu 3*p* peaks (see Figure S4.2). As Cu 3*p* is closer in kinetic energy to Pd 3*d* than Cu 2*p*, the probing depths will be similar. This ratio is comparable with the theoretical one of 0.63:1 based on the synthetic procedure, which is also verified by the microscopic analysis (*vide infra*).

Transmission electron microscopy (TEM) studies of the $_{2}$Pd-$_{8}$Cu/C catalyst reveal the QDAs, sizing between 10 to 25 nm, were uniformly distributed on the carbon surface (see Figure 4.3a). A clear view of the metallic QDAs was obtained via a high angle annular dark field imaging using the scanning transmission electron microscope (HAADF-STEM, Figure 4.3b). All the QDAs contain both palladium and copper, as shown by the elemental mappings from the energy dispersive spectroscopy (EDS, see Figure 4.3c). No monometallic species were observed. This confirms that the Pd grows from the Cu nanoparticles during the galvanic displacement. We also performed the EDS line scan of the QDAs at the nanoscale (Figure 4.3d). The scan profile in Figure 3e shows alternating signals for Cu and Pd, implying the formation of the QDA structure as illustrated in Figure 4.1. Specifically, the size of all Cu and Pd domains is less than 3 nm, which

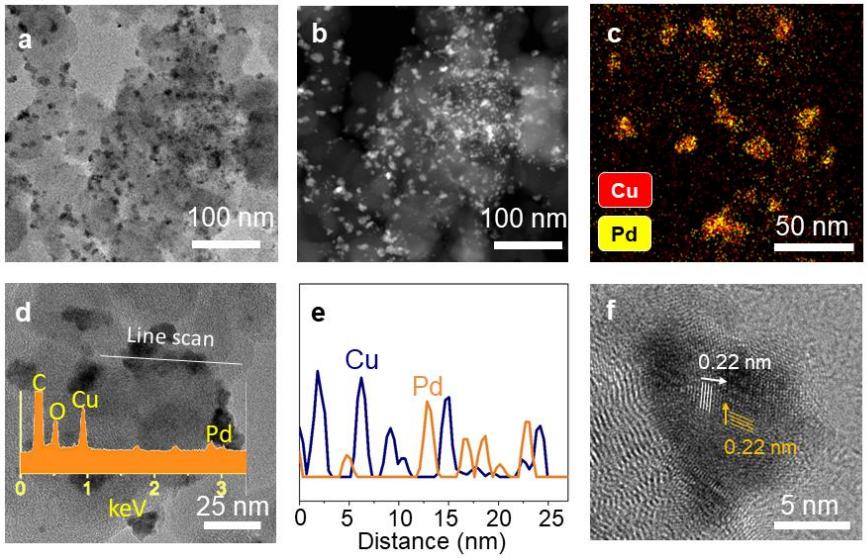

***Figure 4.3**. Microscopic characterizations of $_2$Pd-$_8$Cu/C QDA: a) TEM micrograph; b) HAADF-TEM micrograph; c) EDS elemental mapping; d) TEM image of the QDA where EDS line scan was performed, the inset is the EDS spectrum of the entire area; e) TEM-EDS line scan analysis of Cu and Pd; f) HRTEM micrograph.*

corroborate the quantum-dot nature of both Cu_2O and Pd particles. The high-resolution TEM (HRTEM) in Figure 4.3f also reveals that the particles are assemblies of multiple quantum dots. The interplanar spacings in these nanoclusters are ~0.22 nm, corresponding to either Pd (111) or Cu_2O (200) with a small lattice expansion.[34,35]

To examine the catalytic performance of the new structure, we used the Pd-Cu/C QDAs in three electrooxidation examples: formaldehyde, glucose and ethanol. These oxidations are important in a number of practical applications, such as in fuel cells, (bio)sensing and wastewater treatment.[36] The conversion of formaldehyde is also relevant in the electroless copper deposition (ECD) process. For the formaldehyde oxidation reaction, we used a classical 3-electrode setup with an alkaline electrolyte containing KOH, ethylenediaminetetraaceticacid (EDTA) and formaldehyde. EDTA was added to simulate the environment of the ECD process (it is commonly added to ensure the stability of Cu^{2+} and the quality of the deposited layer). The Pd/C catalyst was tested in both blank-bath (formaldehyde-free) and formaldehyde-bath (see Figure 4.4a; the bath

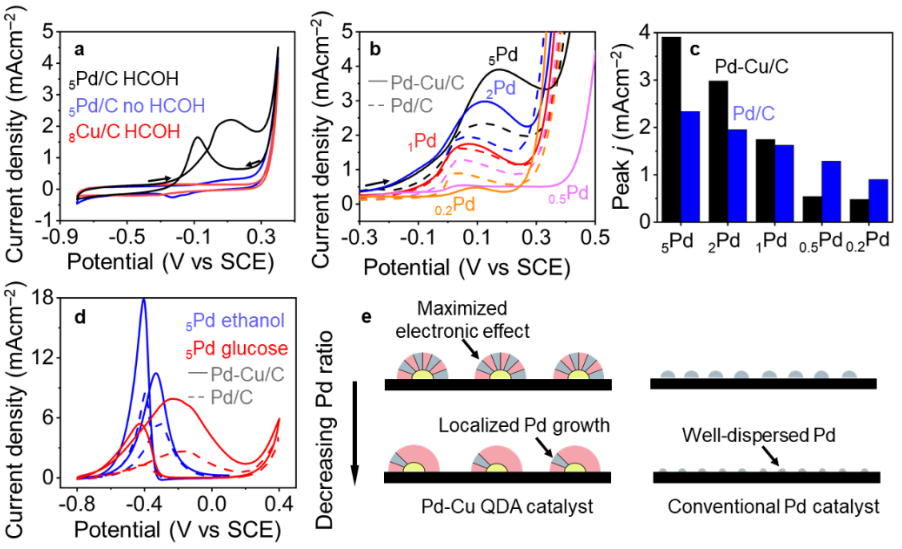

Figure 4.4. *a) CV curves of $_5$Pd/C and $_8$Cu/C in HCOH-free and HCOH bath; b) comparison of LSV curves of Pd-Cu/C QDAs (solid lines) with the corresponding Pd/C (dashed lines) with the same Pd content in formaldehyde oxidation; c) comparison of peak current density of different catalysts in formaldehyde oxidation; d) CV curves of $_5$Pd/C and $_5$Pd-$_8$Cu/C for both glucose and ethanol oxidation; e) schematic structural comparison of QDA with conventional Pd catalyst with varying Pd ration. Test conditions are specified in the supporting information.*

compositions are given in the Supporting Information). No parasitic current from EDTA oxidation was observed in our potential range in the blank bath. The cyclic voltammetry (CV) curve in the formaldehyde-bath has an anodic peak in the forward scan at 0.1 V vs SCE which is attributed to the oxidation of formaldehyde. The peak at −0.1 V in the backward scan originates from the oxidation of organic fragments, which is also documented in the electrooxidation of other small organics.[37] These peaks were not observed in the experiments in the blank bath. In contrast, when the Cu/C catalyst was tested, neither of these anodic peaks were observed. This inactivity was due to the surface oxidation of the Cu nanoparticle. To ensure the reaction was carried out at the optimum temperature, we performed the CV at different temperatures. The highest oxidation current was observed at 45 °C as shown in Figure S4.3. This temperature was used in all subsequent experiments.

We then analyzed catalytic performance of Pd-Cu_2O QDAs with varying Pd:Cu mass ratios. Comparing with the corresponding monometallic Pd/C controls, the QDAs containing >1wt% Pd loadings showed the improved activity in the linear sweep voltammograms (LSVs). For example, the $_5$Pd-$_8$Cu/C QDA had a peak oxidation current density of 3.91 mA cm^{-2} whereas that for $_5$Pd/C was 2.34 mA cm^{-2} (see Figures 4.4b and 4.4c). The structural advantage of Pd-Cu_2O QDAs was also valid in the glucose electrooxidation performed in a 0.5 M KOH + 0.5 M glucose electrolyte. Two peaks are observed in the CV curve (Figure 4.4d, scan rate 50 mV s^{-1}): a peak in the forward scan at -0.23 V vs SCE and the other one in the backward scan at -0.43 V vs SCE. The former is attributed to the oxidation of glucose, while the latter is attributed to the oxidation of bound intermediates which are not oxidized during the forward scan.[38] The peaks have a small positive shift (0.04 V and 0.03 V for the forward and backward scan, respectively) for $_5$Pd/C. The peak current density for glucose oxidation of $_5$Pd-$_8$Cu/C is ~3 times higher than that of $_5$Pd/C (7.90 mA cm^{-2}, 17.6 A cm^{-2} mg_{Pd}^{-1} *vs.* 2.67 mA cm^{-2}, 5.93 A $cm^{-2}mg_{Pd}^{-1}$). A similar result was obtained in the ethanol oxidation reaction performed in 1.0 M ethanol and 1.0 M KOH electrolyte. The superior performance of QDA in the oxidation of these small organic molecules emphasizes the importance of the interaction between the Pd and Cu_2O domains.

We hypothesize that the catalytic advantages of QDAs come from the maximized interfacial electronic effect between Pd and Cu_2O quantum dots (see illustration in Figure 4.1). Such an effect is prominent only when the size of Pd and Cu_2O dots is the same, maximizing the phase boundaries. When the Pd ratio decreases, this effect diminishes accordingly and the QDA will perform similarly to pure Pd (1% Pd). However, at extremely low Pd loadings (e.g., 0.5 and 0.2 wt% Pd, see Figure 4.4d), the low Pd cation concentration in the galvanic displacement bath results in the formation of much less Pd nuclei which subsequentially undergo non-epitaxial and continuous growth. Therefore, non-uniform dispersed, localized and large Pd dots are observed on the Cu particles (see Figure 4.4e). Hence, these QDA perform worse than the corresponding Pd/C with well distributed Pd nanoparticles.

To understand and verify the interfacial properties, we have constructed a Pd-Cu_2O QDA model and performed density-functional theory (DFT) calculations. Figure 4.5a shows the optimized hetero-structure containing a 46-

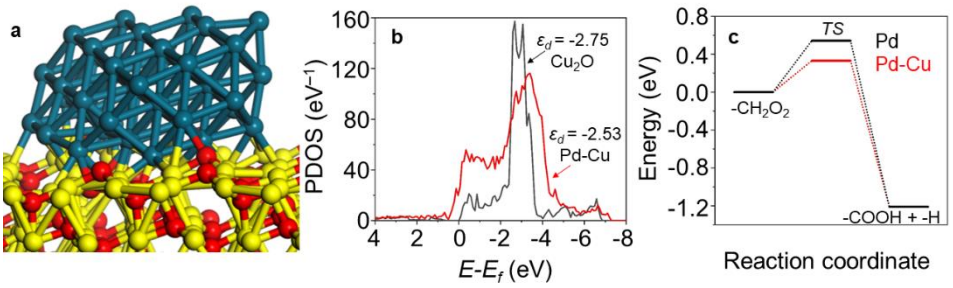

Figure 4.5. *a) Configuration of the Pd-Cu_2O QDA model; b) projected density of states (PDOS) for Cu_2O and Pd-Cu_2O QDA; c) DFT energy diagram of -CH_2O_2 conversion on Pd and Pd-Cu_2O QDA with normalized zero potential energy.*

atom Pd cluster on Cu_2O (111) surface. This structure is thermodynamically favorable, as the interface has more interfacial bonds and less strain stress.[39] Because of the formation of the interfacial Pd-O and Pd-Cu bonds, charge accumulation at the boundary is observed. This has substantially changed the projected density of states in the interface (see Figure 4.5b). The d-band center (ε_d) of the QDA was upshifted to –2.53 eV toward the Fermi level compared to –2.75 eV of Cu_2O. The catalytic benefits of the optimized electronic structure were demonstrated in the potential energy diagram in Figure 4.5c. We used the optimized Meerakker's model[40] in the alkaline media in which HCHO is in equilibrium with CH_2OOH^-:

$$HCHO + H_2O \leftrightarrow CH_2(OH)_2 \quad (4.5)$$

$$CH_2(OH)_2 + OH^- \leftrightarrow CH_2OOH^- + H_2O \quad (4.6)$$

The elementary reactions are below:

$$-CH_2OOH^- + OH^- \rightarrow -CH_2O_2^{2-} + H_2O \quad (4.7)$$

$$-CH_2O_2^{2-} + -^* \rightarrow -COOH^- + -H + e^- \quad (4.8)$$

$$-H + OH^- \rightarrow H_2O + e^- \quad (4.9)$$

where eq. 4.8 is the rate-determining step. The calculation indicates that the activation energy barrier from CH_2O_2 to COOH has decreased by 0.21 eV when the catalytic surface is switched from Pd to Pd-Cu heterostructure.

We then tested the performance of the Pd-Cu_2O QDAs in electroless copper deposition (ECD). The plating is performed in a bath containing metal ions and a

reducing agent (eq 4.10). Although this reaction is autocatalytic, it must be initiated by a catalyst. The state-of-the-art Pd initiator is rather expensive, replacing it with cheaper and more active materials is industrially important.

$$M^{x+} + Red^{n} \rightarrow M^{0} + Red^{n+x} \qquad (4.10)$$

In the traditional alkaline formaldehyde bath, the reduction of EDTA-stabilized Cu^{2+} cations proceeds through the adsorption of formaldehyde hydrate on the catalyst surface, followed by anodic oxidation to formate (eq 4.11).[29] The electrons liberated from this process are transferred for cathodic Cu deposition (eq 4.12). The combination of both reactions gives the overall cell reaction (eq 4.13). The initiator catalyzes this reaction via facilitating the oxidation of formaldehyde.

$$HCOO^{-} + 2H_2O + 2e^{-} \rightarrow HCOH + 3OH^{-} \text{ (pH 14)} \qquad E = -1.070\ V \qquad (4.11)$$

$$[CuEDTA]^{2-} + 2e^{-} \rightarrow Cu^{0} + EDTA^{4-} \qquad E = -0.216\ V \qquad (4.12)$$

$$HCOH + 3OH^{-} + Cu^{2+} \rightarrow HCOO^{-} + 2H_2O + Cu^{0} \text{ (pH 14)} \qquad E = +0.854\ V \qquad (4.13)$$

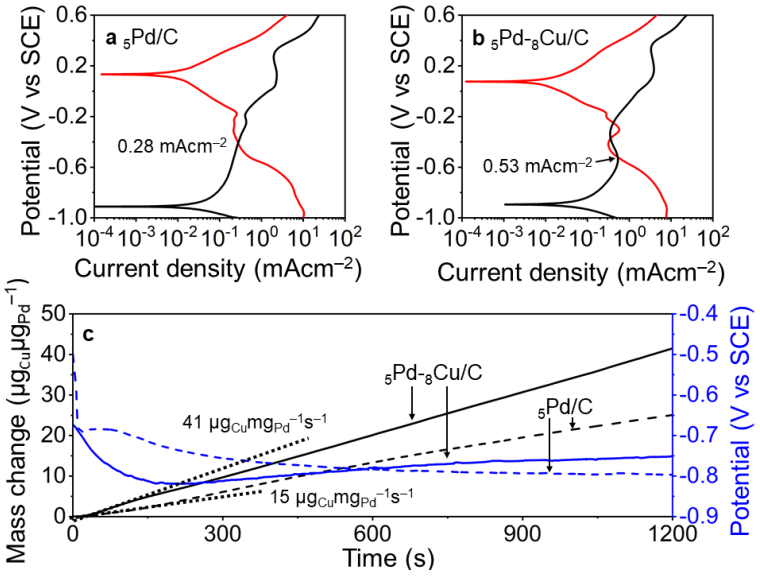

Figure 4.6. *Tafel curves recorded in their respective baths for formaldehyde oxidation and copper reduction for a) $_5$Pd/C and b) $_5$Pd-$_8$Cu/C; c) the mass change and potential during ECD measured via eQCM of $_5$Pd-$_8$Cu/C (solid lines) and $_5$Pd/C (dashed lines). For conditions and bath compositions, see the supporting information.*

We have shown that the Pd-Cu_2O QDAs are excellent catalysts for formaldehyde oxidation (*vide supra*). Yet, monitoring both the formaldehyde oxidation and copper reduction gives a much clearer picture. Thus, we first used the mixed potential theory to further analyze the activity of both the $_5$Pd/C and $_5$Pd-$_8$Cu/C QDA catalysts in ECD. The mixed potential theory concludes that the maximum electrochemical reaction rate is achieved when both the anodic and cathodic reactions occur at the same rate, resulting in no buildup of electrons at the interface. The kinetics can be derived from the intersection between the two half-reaction Tafel curves. Here, we measured the Tafel curves for copper reduction and formaldehyde oxidation for both the $_5$Pd/C catalyst and $_5$Pd-$_8$Cu/C QDA (Figure 4.6a & 4.6b). For $_5$Pd/C, the curves intersect at −0.41 V vs SCE with a current density of 0.28 mA cm^{-2}. In contrast, the $_5$Pd-$_8$Cu/C QDA intersects at a lower potential (−0.52 V vs SCE), while showing substantially increased current density of 0.53 mA cm^{-2}. We hence conclude that the $_5$Pd-$_8$Cu/C QDA also outperformed the monometallic $_5$Pd/C catalyst in the ECD.

As the mixed potential theory only gives an indication of the *initial* activity of the catalyst, we also used an electrochemical quartz crystal microbalance (eQCM) to monitor both the deposition rate and surface potential. The quartz crystals were coated with the catalysts and then subjected to the ECD-bath (see Table S4.2 for the both composition). During ECD, the frequency variations of this crystal were monitored, which are correlated to the mass change. Simultaneously, the potential was also recorded, revealing more information about the electrochemical nature of the plating process. Both the $_5$Pd-$_8$Cu/C QDA and $_5$Pd/C catalyst were examined in this eQCM system. A plot of the potential and mass change versus time is shown in Figure 4.6c. Deposition rates of 35 μg_{Cu} $mg_{Pd}^{-1}s^{-1}$ and 21 μg_{Cu} $mg_{Pd}^{-1}s^{-1}$ are derived from the total plating time for $_5$Pd-$_8$Cu/C and $_5$Pd/C, respectively (deposition rates are denoted as the amount of plated copper per mg of palladium per second). For both catalysts, a linear increase for the mass change is observed after the first 150 s. This linearity comes from the uniformly plated copper on the surface, which autocatalytically grows at constant rate. The differences in deposition rate for 150–1200 s region comes from the surface area differences of the pre-deposited copper film.

We thus obtained the plating kinetics of the $_5$Pd-$_8$Cu/C and $_5$Pd/C catalysts from the first 150 s of ECD. The first 15 seconds is an induction period in which the system equilibrates to the plating bath. After this period, the $_5$Pd-$_8$Cu/C QDA achieved a deposition rate of 41 μg_{Cu} $mg_{Pd}^{-1}s^{-1}$. This is faster than the

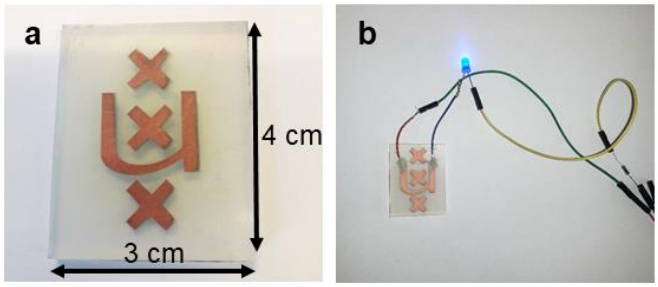

Figure 4.7. *a) The University of Amsterdam logo plated in copper on a silicon rubber plate; b) conductivity test of the plated surface using a LED assembly.*

monometallic $_{5}$Pd/C catalyst, which had a deposition rate of 15 μg_{Cu} $mg_{Pd^{-1}s^{-1}}$. Furthermore, the initial deposition rate of $_{5}$Pd-$_{8}$Cu/C is faster than that during autocatalysis which is catalyzed by deposited Cu layer whereas this rate for $_{5}$Pd/C is lower than that during the autocatalysis. This implies that the activity order is $_{5}$Pd-$_{8}$Cu/C QDA > Cu > $_{5}$Pd/C. This trend is also reflected by the potential profiles of the two materials. From the autocatalysis region in Figure 4.6c, we found the potential for auto- catalyzed ECD is in the range of –0.75 to –0.8 V vs Ag/AgCl. After the initial induction period, the potential of the $_{5}$Pd-$_{8}$Cu/C QDA became lower than the autocatalytic ECD potential that of whereas $_{5}$Pd/C remained higher than the autocatalytic potential.

Finally, we demonstrated the excellent mechanical and electronic properties of the Cu deposit layer initiated by the $_{5}$Pd-$_{8}$Cu/C QDA by plating copper wires on a flexible silicon rubber substrate. The QDA catalyst was airbrushed onto the substrate using a simple mask with the logo of the University of Amsterdam. After ECD, copper layer was uniformly and exclusively deposited within the pattern where catalyst was spray-painted (Figure 4.7a). The copper pattern is highly conductive and could be used as wires to successfully power a LED assembly (Figure 4.7b). This shows the potential of using the new catalyst in the context of industrial applications.

Conclusion

We developed a novel quantum dot assembly (QDA) catalyst via galvanic displacement approach, consisting of 3 nm Cu_2O and Pd clusters. These QDAs are better electrocatalysts for the oxidation of formaldehyde, glucose and ethanol, outperforming equivalent monometallic catalysts. Together with the DFT simulations, we concluded that the activity enhancement was originated from the maximized interfacial electronic effect between Pd and Cu_2O quantum dots. The industrial relevance of the new catalyst was demonstrated in the excellent performance in initiating the electroless copper deposition, yet reducing the Pd-Cu_2O metal loading in the future will make the supported catalyst even more promising for industrial processes. We believe that this catalyst structure opens opportunities for designing better catalytic materials at ultrasmall nanoscale.

References

[1] C. Chen, C. Nan, D. Wang, Q. Su, H. Duan, X. Liu, L. Zhang, D. Chu, W. Song, Q. Peng, Y. Li, Mesoporous Multicomponent Nanocomposite Colloidal Spheres: Ideal High-Temperature Stable Model Catalysts, *Angew. Chem. Int. Ed.* **2011**, *50*, 3725–3729.

[2] L. Liu, J. Jiao, W. Wei, B. Lv, Y. Liu, Z. Hu, J. Tang, Construction of multicomponent nanocomposite CdSe/NaYF4:Yb,Er colloidal spheres for tuning visible light, *Scr. Mater.* **2019**, *169*, 61–64.

[3] J. Liu, J. Wang, B. Zhang, Y. Ruan, H. Wan, X. Ji, K. Xu, D. Zha, L. Miao, J. Jiang, Mutually beneficial Co 3 O 4 @MoS 2 heterostructures as a highly efficient bifunctional catalyst for electrochemical overall water splitting, *J. Mater. Chem. A* **2018**, *6*, 2067–2072.

[4] L. Jiang, W. Zhu, C. Wang, W. Dong, L. Zhang, G. Wang, B. Chen, C. Li, X. Zhang, Preparation of hollow Ag/Pt heterostructures on TiO2 nanowires and their catalytic properties, *Appl. Catal. B Environ.* **2016**, *180*, 344–350.

[5] X. Yan, Y. Yang, Y. Zeng, B. Shalchi Amirkhiz, J.-L. Luo, N. Yan, Generating C4 Alkenes in Solid Oxide Fuel Cells via Cofeeding H $_2$ and *n* -Butane Using a Selective Anode Electrocatalyst, *ACS Appl. Mater. Interfaces* **2020**, *12*, 16209–16215.

[6] S. Su, Y. Shi, Y. Zhou, Y.-B. Wang, F.-B. Wang, X.-H. Xia, Tailoring the electron density of Pd nanoparticles through electronic metal-support interaction for accelerating electrocatalysis of formic acid, *Electrochem. Commun.* **2019**, *107*, 106540.

[7] Y. Kang, X. Ye, J. Chen, Y. Cai, R. E. Diaz, R. R. Adzic, E. A. Stach, C. B. Murray, Design of Pt–Pd Binary Superlattices Exploiting Shape Effects and Synergistic Effects for Oxygen Reduction Reactions, *J. Am. Chem. Soc.* **2013**, *135*, 42–45.

[8] N. Yan, J. Pandey, Y. Zeng, B. S. Amirkhiz, B. Hua, N. J. Geels, J.-L. Luo, G. Rothenberg, Developing a Thermal- and Coking-Resistant Cobalt–Tungsten Bimetallic Anode Catalyst for Solid Oxide Fuel Cells, *ACS Catal.* **2016**, *6*, 4630–4634.

[9] X. Wang, G. Sun, N. Li, P. Chen, Quantum dots derived from two-dimensional materials and their applications for catalysis and energy, *Chem. Soc. Rev.* **2016**, *45*, 2239–2262.

[10] H. Li, L. Li, Y. Li, The electronic structure and geometric structure of nanoclusters as catalytic active sites, *Nanotechnol. Rev.* **2013**, *2*, 515–528.

[11] X. Zhou, Z. Tian, J. Li, H. Ruan, Y. Ma, Z. Yang, Y. Qu, Synergistically enhanced activity of graphene quantum dot/multi-walled carbon nanotube composites as metal-free catalysts for oxygen reduction reaction, *Nanoscale* **2014**, *6*, 2603.

[12] E. Roduner, Size matters: why nanomaterials are different, *Chem. Soc. Rev.* **2006**, *35*, 583.

[13] H. Wang, X.-K. Gu, X. Zheng, H. Pan, J. Zhu, S. Chen, L. Cao, W.-X. Li, J. Lu, Disentangling the size-dependent geometric and electronic effects of palladium nanocatalysts beyond selectivity, *Sci. Adv.* **2019**, *5*, eaat6413.

[14] V. K. LaMer, R. H. Dinegar, Theory, Production and Mechanism of Formation of Monodispersed Hydrosols, *J. Am. Chem. Soc.* **1950**, *72*, 4847–4854.

[15] Y. Sun, Controlled synthesis of colloidal silver nanoparticles in organic solutions: empirical rules for nucleation engineering, *Chem Soc Rev* **2013**, *42*, 2497–2511.

[16] C.-L. Lee, C.-C. Syu, H.-P. Chiou, C.-R. Liu, C.-H. Huang, Effect of electrochemical surface area on electroless copper deposition: Pd nanocubes as new activators, *Electrochim. Acta* **2012**, *59*, 587–591.

[17] C.-Y. Chiu, P.-J. Chung, K.-U. Lao, C.-W. Liao, M. H. Huang, Facet-Dependent Catalytic Activity of Gold Nanocubes, Octahedra, and Rhombic Dodecahedra toward 4-Nitroaniline Reduction, *J. Phys. Chem. C* **2012**, *116*, 23757–23763.

[18] M. McEachran, D. Keogh, B. Pietrobon, N. Cathcart, I. Gourevich, N. Coombs, V. Kitaev, Ultrathin Gold Nanoframes through Surfactant-Free Templating of Faceted Pentagonal Silver Nanoparticles, *J. Am. Chem. Soc.* **2011**, *133*, 8066–8069.

[19] S. M. George, Atomic Layer Deposition: An Overview, *Chem. Rev.* **2010**, *110*, 111–131.

[20] R. W. Johnson, A. Hultqvist, S. F. Bent, A brief review of atomic layer deposition: from fundamentals to applications, *Mater. Today* **2014**, *17*, 236–246.

[21] J. Lu, B. Fu, M. C. Kung, G. Xiao, J. W. Elam, H. H. Kung, P. C. Stair, Coking- and Sintering-Resistant Palladium Catalysts Achieved Through Atomic Layer Deposition, *Science* **2012**, *335*, 1205–1208.

[22] R. Liu, Y. Lin, L.-Y. Chou, S. W. Sheehan, W. He, F. Zhang, H. J. M. Hou, D. Wang, Water Splitting by Tungsten Oxide Prepared by Atomic Layer Deposition and Decorated with an Oxygen-Evolving Catalyst, *Angew. Chem. Int. Ed.* **2011**, *50*, 499–502.

[23] H. Ge, B. Zhang, X. Gu, H. Liang, H. Yang, Z. Gao, J. Wang, Y. Qin, A Tandem Catalyst with Multiple Metal Oxide Interfaces Produced by Atomic Layer Deposition, *Angew. Chem. Int. Ed.* **2016**, *55*, 7081–7085.

[24] A. Papaderakis, I. Mintsouli, J. Georgieva, S. Sotiropoulos, Electrocatalysts Prepared by Galvanic Replacement, *Catalysts* **2017**, *7*, 80.

[25] S. M. Alia, Y. S. Yan, B. S. Pivovar, Galvanic displacement as a route to highly active and durable extended surface electrocatalysts, *Catal. Sci. Technol.* **2014**, *4*, 3589–3600.

[26] C. M. Hangarter, Y.-I. Lee, S. C. Hernandez, Y. Choa, N. V. Myung, Nanopeapods by Galvanic Displacement Reaction, *Angew. Chem. Int. Ed.* **2010**, *49*, 7081–7085.

[27] M. B. Strand, G. J. Leong, C. J. Tassone, B. Larsen, K. C. Neyerlin, B. Gorman, D. R. Diercks, S. Pylypenko, B. Pivovar, R. M. Richards, Mechanistic Study of Shape-Anisotropic Nanomaterials Synthesized via Spontaneous Galvanic Displacement, *J. Phys. Chem. C* **2016**, *120*, 25053–25060.

[28] Y. Shacham-Diamand, T. Osaka, Y. Okinaka, A. Sugiyama, V. Dubin, 30years of electroless plating for semiconductor and polymer micro-systems, *Microelectron. Eng.* **2015**, *132*, 35–45.

[29] S. Ghosh, Electroless copper deposition: A critical review, *Thin Solid Films* **2019**, *669*, 641–658.

[30] W. M. Haynes, *CRC Handbook of Chemistry and Physics, 93rd Edition*, CRC Press, Boca Raton, **2012**.

[31] M. C. Biesinger, Advanced analysis of copper X-ray photoelectron spectra: Advanced analysis of copper X-ray photoelectron spectra, *Surf. Interface Anal.* **2017**, *49*, 1325–1334.

[32] M. Brun, A. Berthet, J. C. Bertolini, XPS, AES and Auger parameter of Pd and PdO, *J. Electron Spectrosc. Relat. Phenom.* **1999**, *104*, 55–60.

[33] D. Zemlyanov, B. Aszalos-Kiss, E. Kleimenov, D. Teschner, S. Zafeiratos, M. Hävecker, A. Knop-Gericke, R. Schlögl, H. Gabasch, W. Unterberger, K. Hayek, B. Klötzer, In situ XPS study of Pd(111) oxidation. Part 1: 2D oxide formation in 10–3mbar O2, *Surf. Sci.* **2006**, *600*, 983–994.

[34] D. Zhang, C. Jin, H. Tian, Y. Xiong, H. Zhang, P. Qiao, J. Fan, Z. Zhang, Z. Y. Li, J. Li, An In situ TEM study of the surface oxidation of palladium nanocrystals assisted by electron irradiation, *Nanoscale* **2017**, *9*, 6327–6333.

[35] P. Liu, Z. Li, W. Cai, M. Fang, X. Luo, Fabrication of cuprous oxide nanoparticles by laser ablation in PVP aqueous solution, *RSC Adv.* **2011**, *1*, 847–851.

[36] J. Biemolt, K. van der Veen, N. J. Geels, G. Rothenberg, N. Yan, Efficient oxygen reduction to H2O2 in highly porous manganese and nitrogen co-doped carbon nanorods enabling electro-degradation of bulk organics, *Carbon* **2019**, *155*, 643–649.

[37] F. Kaedi, Z. Yavari, M. Asmaei, A. R. Abbasian, M. Noroozifar, Ethanol electrooxidation on high-performance mesoporous ZnFe2O4-supported palladium nanoparticles, *New J. Chem.* **2019**, *43*, 3884–3890.

[38] B. Tao, F. Miao, P. K. Chu, Preparation and characterization of a novel nickel–palladium electrode supported by silicon nanowires for direct glucose fuel cell, *Electrochimica Acta* **2012**, *65*, 149–152.

[39] Y. Guo, J. Liu, Y.-T. Xu, B. Zhao, X. Wang, X.-Z. Fu, R. Sun, C.-P. Wong, In situ redox growth of mesoporous Pd-Cu2O nanoheterostructures for improved glucose oxidation electrocatalysis, *Sci. Bull.* **2019**, *64*, 764–773.

[40] J. Van Den Meerakker, On the mechanism of electroless plating. II. One mechanism for different reductants, *J. Appl. Electrochem.* **1981**, *11*, 395–400.

Appendix, the Supporting Information for Chapter 4

Experimental

Materials characterization

X-ray diffraction (XRD) diffractograms were measured with a Miniflex II diffractometer equipped with CuKα radiation, where the X-ray tube operated at 30 kV with a current of 5 mA. X-ray photoelectron spectroscopy (XPS) spectra were acquired using a Scienta Omicron HiPP-3 analyzer and a monochromatic Al Kα source operating at 20mA emission current. The base pressure was about $2*10^{-9}$ mbar, and the operating pressure was about $5*10^{-9}$ mbar. Survey and high-resolution spectra were acquired at pass energies of 300eV and 100eV respectively. Data analysis and quantification were performed using KolXPD from Kolibrik. The morphology and surface composition of both the fresh and the spent catalysts were characterized using the Talos F200S Field Emission Transmission Electron Microscope (TEM) equipped with an Energy Dispersive X-ray Spectrometer (EDS). The accelerating voltage was 200 kV. For the electrochemical experiments a Gamry reference 600 potentiostat and Gamry eQCM 10M were used.

Procedure for the preparation of Cu/C material

Vulcan VXC-72R (500 mg) was activated under vacuum at 120 °C for 18 hours. Then it was impregnated under vacuum with a $Cu(NO_3)_2.3H_2O$ solution (152 mg in 0.2 mL DI water) under vigorous stirring. Afterwards, the $Cu(NO_3)_2$/C material was dried at 100 °C for 18 hours and reduced at 250 °C for 1 h in a 5% H_2/N_2 atmosphere (Ramp 5 °C min^{-1}, flowrate 150 mL min^{-1}).

General procedure for the preparation of Pd-Cu/C QDA

A palladium solution ($Pd(NO_3)_2{\cdot}xH_2O$ Pd≥39% in 50 mL DI water, amounts varies per material) was degassed with nitrogen for >30 minutes, to which 200 mg Cu/C material was directly added, limiting the exposure time to O_2. The

suspension was sonicated for 30 min and agitated for 18 hours to complete the galvanic replacement of Cu by Pd. The Pd-Cu/C was filtered, washed with 100 mL DI water and dried under vacuum at room temperature.

Example: $_{2}$Pd-$_{8}$Cu/C

A palladium solution ($Pd(NO_3)_2 \cdot xH_2O$ Pd≥39%, 10.3 mg in 50 mL DI water) was degassed with nitrogen for >30 minutes, to which 200 mg Cu/C material was directly added, limiting the exposure time to O_2. The suspension was sonicated for 30 min and agitated for 18 hours to complete the galvanic replacement of Cu by Pd. The $_{2}$Pd-$_{8}$Cu/C was filtered, washed with 100 mL DI water and dried under vacuum at room temperature.

General procedure for the preparation of Pd/C control samples

Vulcan VXC-72R (500 mg) was activated under vacuum at 120 °C for 18 hours. Then it was impregnated under vacuum with a $Pd(NO_3)_2 \cdot xH_2O$ solution (Pd≥39%, varying mg in 0.2 mL DI water) under vigorous stirring. Afterwards, the $Pd(NO_3)_2$/C material was dried at 100 °C for 18 hours and reduced at 160 °C for 1 h in a 5% H_2/N_2 atmosphere (Ramp 5 °C min^{-1}, flowrate 150 mL min^{-1}).

Example: $_{2}$Pd/C

Vulcan VXC-72R (500 mg) was activated under vacuum at 120 °C for 18 hours. Then it was impregnated under vacuum with a $Pd(NO_3)_2 \cdot xH_2O$ solution (Pd≥39%, 10.2 mg in 0.2 mL DI water) under vigorous stirring. Afterwards, the $Pd(NO_3)_2$/C material was dried at 100 °C for 18 hours and reduced at 160 °C for 1 h in a 5% H_2/N_2 atmosphere (Ramp 5 °C min^{-1}, flowrate 150 mL min^{-1}).

Electrochemical procedures

Catalyst inks were prepared by suspending the catalysts (3 mg) in an ethanol:water mixture (2.1:0.9 mL) with 30 µL Nafion® (D-521 dispersion 5 wt.% in water/isopropanol) and sonicated for 18 hours.

Formaldehyde oxidation and ECD related reactions were measured in a standard three-electrode system was used with a glassy carbon working electrode (0.5 mm diameter) drop casted 3 times with 10µL of catalyst ink and dried at 50 °C after each drop. A Saturated Calomel Electrode (SCE) and a Pt wire were used as the reference and counter electrodes, respectively. The bath-compositions are depicted in Table S2, and were purged with high purity nitrogen gas (99.999%)

and maintained at 45 °C before the experiments. Cyclic voltammetry (CV) curves were recorded at 50 mV s^{-1}. For all experiments except copper reduction, CV or LSV curves were recorded till a stable signal was observed (for copper reduction this would change the electrode properties, because of copper plating).

For the eQCM experiments, catalysts were spray painted on a 5 MHz Au quartz crystal (Gamry) using an airbrush and catalyst ink prepared by suspending 1 mg catalyst in 1 mL ethanol. The amount of loaded catalyst was determined by using the change in frequency of the quartz crystal before and after loading of the catalyst. The crystal with catalyst was loaded in a QCM flow cell (Gamry), were the catalyst functions as a working electrode. A platinum tube counter electrode and Ag/AgCl reference electrode. The electroless copper deposition was started by introducing the ECD-bath in the chamber. During the experiment a flow of 0.5 mL min^{-1}. The potential was measured using chronopotentiometry at a 0 mA current. The mass change was derived using the equation:

$$\Delta m = \frac{\Delta F A \sqrt{\mu \rho}}{-2F_0^2} \qquad \text{(s4.1)}$$

where ΔF is the frequency change of the quartz crystal, A is the active area of the quartz crystal, μ is the sheer modules, ρ is the density of quartz, F_o is the fundamental frequency of the quartz crystal, and Δm is the mass gain.

Glucose and ethanol oxidation were measured in a in a standard three-electrode system was used with a glassy carbon working electrode (0.3 mm diameter) drop casted 9 times with 1µL of catalyst ink and dried at 50 °C after each drop. A Saturated Calomel Electrode (SCE) and a Pt wire were used as the reference and counter electrodes, respectively. Ethanol oxidation was recorded in a 1.0 M KOH + 1.0 M ethanol solution. Glucose oxidation was recorded in a 0.5 M KOH + 0.5 M glucose solution. Before the experiments, the electrolyte was purged with high purity nitrogen gas (99.999%) and maintained at 25 °C. The CV curves were recorded at 50 mV s^{-1}. CV curves were recorded till a stable signal was observed.

DFT simulations

The density-functional theory (DFT) calculations were performed, with the Vienna ab initio simulation package (VASP), using the Perdew–Burke-Ernzerhof (PBE) exchange-correlation functional. The projector augmented wave (PAW)

method was used to describe the electron-ion interaction. The 4×4 Cu_2O (111) and Pd (111) slabs, each with three atomic layers with a vacuum spacing of at least 20 Å were constructed. The Pd46 cluster with the (310) facet binding the Cu_2O surface were used to model the Pd-Cu_2O QDA. In all the calculations, an energy cutoff of 400 eV was used for the plane-wave expansion of the electronic wave function. The force and energy convergence criterion was set to 0.05 eV/Å and 10-4 eV, respectively.

Supplementary Figures

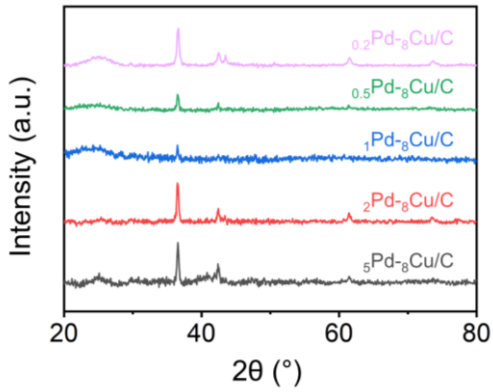

***Figure S4.1**. The XRD spectra of the Pd-Cu_2O QDAs with different palladium loadings.*

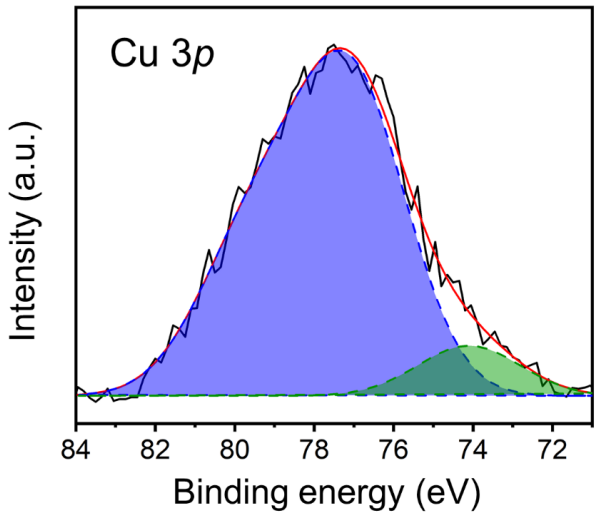

***Figure S4.2**. The Cu 3p XPS spectrum of the $_5$Pd-$_8$Cu/C QDA.*

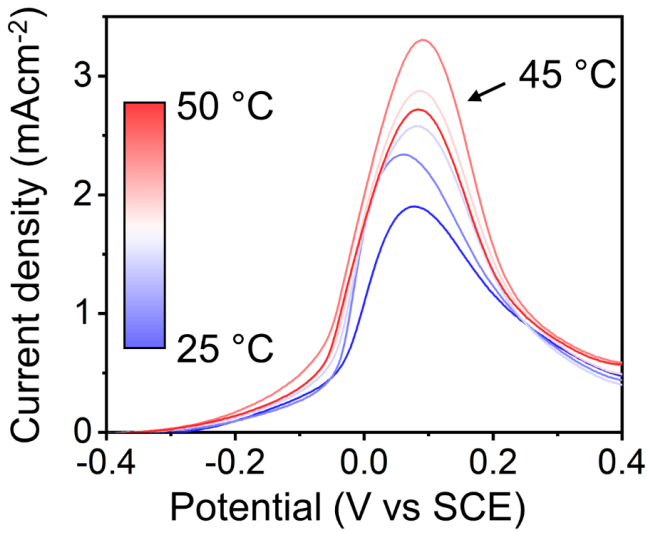

***Figure S4.3.** CV curves showing the dependency of the current density of formaldehyde oxidation on the temperature. The CVs are recorded in a copper-free ECD bath, saturated with N_2 and with a scan rate of 50 mV s^{-1}.*

Supplementary Tables

Table S4.1. The fitting parameters for the XPS spectra and the derived data[a]

Main peak	Fitted peak	Binding energy	Lwid	Gwid	Peak area
Pd3d	Pd^0 $3d_{5/2}$	335.80 eV	0.84	1.25	481
	PdO_x $3d_{5/2}$	337.74 eV	0.84	0.84	3947
	Pd^0 $3d_{3/2}$	341.12 eV	0.84	1.25	321
	PdO_x $3d_{3/2}$	343.06eV	0.84	1.23	2631
Cu2p	CuO $2p_{3/2}$ (1)	933.92 eV	0.14	2.37	3413
	CuO $2p_{3/2}$ (2)	935.29 eV	0.20	3.48	3523
	Cu_2O $2p_{3/2}$	933.44 eV	0.56	3.23	297
	CuO $2p_{3/2}$ (1) sat.	942.46 eV	0.23	4.06	3082
	CuO $2p_{3/2}$ (2) sat.	944.51 eV	0.08	1.34	661
	CuO $2p_{3/2}$ (3) sat.	941.33 eV	0.23	4.06	330
	CuO $2p_{1/2}$	953.92 eV	0	3.65	2818
	Cu_2O $2p_{1/2}$	953.44 eV	0.56	3.23	149
	CuO $2p_{1/2}$ sat	962.65 eV	0	2.86	1634
Cu3p	Cu $3p$	74.10 eV	0	3.05	293
	Voight doublet (split 2.49 eV, ratio 2)	77.05 eV	0	3.30	2916

[a] For the background correction, the Shirley function is used. For peak fitting the Voigt function is used. Specifically for the Cu $3p$ there is also a Voigt doublet used. The binding energy (BE) is peak position in eV. The peak area is calculated by KolXPD. Lwid is the Lorentzian width within the Voigt function. Gwid is the Gaussian width within the function. The split in the Voigt Doublet function is the distance between the two peaks in eV. The ratio in the Voigt doublet is the ratio between the two peak areas. An energy calibration was performed using an Au reference. The Au 4f peak was observed at 83.8 eV (reported 84.0 eV). The offset of -0.2 eV is not taken into account in the values given here.

Table S4.2. The composition of the different ECD baths used in this manuscript

	Conc. in blank-bath	Conc. in formaldehyde-bath	Conc. in copper-bath	Conc. in ECD-bath
$CuSO_4.5H_2O$	-	-	12.48 g L^{-1} (0.05 M)	12.48 g L^{-1} (0.05 M)
HCOH (37% in H_2O)	-	8 mL L^{-1} (0.1 M)	-	8 mL L^{-1} (0.1 M)
EDTA	29.22 g L^{-1} (0.1 M)	29.22 g L^{-1} (0.1 M)	29.22 g L^{-1} (0.1 M)	29.22 g L^{-1} (0.1 M)
2,2'-bipyridyl	20 mg L^{-1}	20 mg L^{-1}	20 mg L^{-1}	20 mg L^{-1}
pH (adjusted with NaOH)	12.4	12.4	12.4	12.4

Table S4.3. Comparison between reported electrocatalysts for ethanol oxidation

Entry	**Material**	**Conditions**	**Peak current (mA mg_{Pd}^{-1})**	**Ref**
Our work	Pd_5-Cu_8/C	1.0 M KOH + 1.0 M ethanol, 50 mV s^{-1}	2833	-
1	Pd-WC/GN	1.0 M KOH + 1.0 M ethanol, 50 mV s^{-1}	2349	[A1]
2	$Pd_{5.0}Sn$/CNT	1.0 M KOH + 1.0 M ethanol, 50 mV s^{-1}	3434	[A2]
3	Pd-Ni/C	0.1 M KOH + 0.5 M ethanol, 50 mV s^{-1}	2010	[A3]
4	PdP_2/rGO	0.5 M KOH + 0.5 M ethanol, 50 mV s^{-1}	1600	[A4]
5	$PdCu_2$-2	1.0 M KOH + 1.0 M ethanol, 50 mV s^{-1}	1630	[A5]
6	$Pd_{21}Cu_{79}$	0.5 M KOH + 0.5 M ethanol, 20 mV s^{-1}	1782	[A6]
7	PdCu/3DGS	1.0 M KOH + 1.0 M ethanol, 50 mV s^{-1}	1140	[A7]
8	Pd-$Cu_{(F)}$/RGO	0.5 M NaOH + 0.5 M ethanol, 20 mV s^{-1}	2416	[A8]
9	Pd_1Fe_1/CNF	1.0 M NaOH + 1.0 M ethanol, 50 mV s^{-1}	2158	[A9]

Additional references

[A1] J. Yang, Y. Xie, R. Wang, B. Jiang, C. Tian, G. Mu, J. Yin, B. Wang, H. Fu, Synergistic Effect of Tungsten Carbide and Palladium on Graphene for Promoted Ethanol Electrooxidation, *ACS Appl. Mater. Interfaces* **2013**, *5*, 6571–6579.

[A2] L. Ning, X. Liu, M. Deng, Z. Huang, A. Zhu, Q. Zhang, Q. Liu, Palladium-based nanocatalysts anchored on CNT with high activity and durability for ethanol electrooxidation, *Electrochim. Acta* **2019**, *297*, 206–214.

[A3] M. D. Obradović, Z. M. Stančić, U. Č. Lačnjevac, V. V. Radmilović, A. Gavrilović-Wohlmuther, V. R. Radmilović, S. Lj. Gojković, Electrochemical oxidation of ethanol on palladium-nickel nanocatalyst in alkaline media, *Appl. Catal. B Environ.* **2016**, *189*, 110–118.

[A4] J. Liu, Z. Luo, J. Li, X. Yu, J. Llorca, D. Nasiou, J. Arbiol, M. Meyns, A. Cabot, Graphene-supported palladium phosphide PdP2 nanocrystals for ethanol electrooxidation, *Appl. Catal. B Environ.* **2019**, *242*, 258–266.

[A5] J. Xue, G. Han, W. Ye, Y. Sang, H. Li, P. Guo, X. S. Zhao, Structural Regulation of PdCu2 Nanoparticles and Their Electrocatalytic Performance for Ethanol Oxidation, *ACS Appl. Mater. Interfaces* **2016**, *8*, 34497–34505.

[A6] J. Yin, S. Shan, M. S. Ng, L. Yang, D. Mott, W. Fang, N. Kang, J. Luo, C.-J. Zhong, Catalytic and Electrocatalytic Oxidation of Ethanol over Palladium-Based Nanoalloy Catalysts, *Langmuir* **2013**, *29*, 9249–9258.

[A7] C. Hu, X. Zhai, Y. Zhao, K. Bian, J. Zhang, L. Qu, H. Zhang, H. Luo, Small-sized PdCu nanocapsules on 3D graphene for high-performance ethanol oxidation, *Nanoscale* **2014**, *6*, 2768–2775.

[A8] J. Zhang, A. Feng, J. Bai, Z. Tan, W. Shao, Y. Yang, W. Hong, Z. Xiao, One-Pot Synthesis of Hierarchical Flower-Like Pd-Cu Alloy Support on Graphene Towards Ethanol Oxidation, *Nanoscale Res. Lett.* **2017**, *12*, 521.

[A9] D. Geng, S. Zhu, M. Chai, Z. Zhang, J. Fan, Q. Xu, Y. Min, Pd x Fe y alloy nanoparticles decorated on carbon nanofibers with improved electrocatalytic activity for ethanol electrooxidation in alkaline media, *New J. Chem.* **2020**, *44*, 5023–5032.

.

Chapter 5
An Anion-Exchange Membrane Fuel Cell Containing Only Abundant and Affordable Materials

We present a unique anion-exchange membrane fuel cell (AEMFC) containing only affordable and abundant materials: NiFe hydrogen oxidation reaction (HOR) and nitrogen-doped carbon oxygen reduction reaction (ORR) electrocatalysts. AEMFCs are an attractive alternative to proton-exchange membrane fuel cells. They can run under alkaline conditions, allowing the use of platinum group metal (PGM) free electrocatalysts. Yet the same alkaline conditions incur an overpotential loss in ORR, and also slow the HOR. This can be solved by using PGM electrodes, but then the original advantage disappears. In contrast, our fuel cell is free of both PGMs as well as Critical Raw Materials (CRMs). Electrochemical studies confirmed that the catalysts are highly active in both HOR and ORR in an alkaline electrolyte. The morphology, composition and chemical states of the electrocatalysts were characterized by different techniques, including SEM, TEM, XPS, XRD and EELS. We then tested the electrocatalysts' performance in a fuel cell device. The cell achieved a maximum power density of 56 mW cm^{-2}, and a limiting current density of 220 mA cm^{-2}. These results are among the best reported to date for a PGM-free and CRM-free anion-exchange membrane fuel cell.

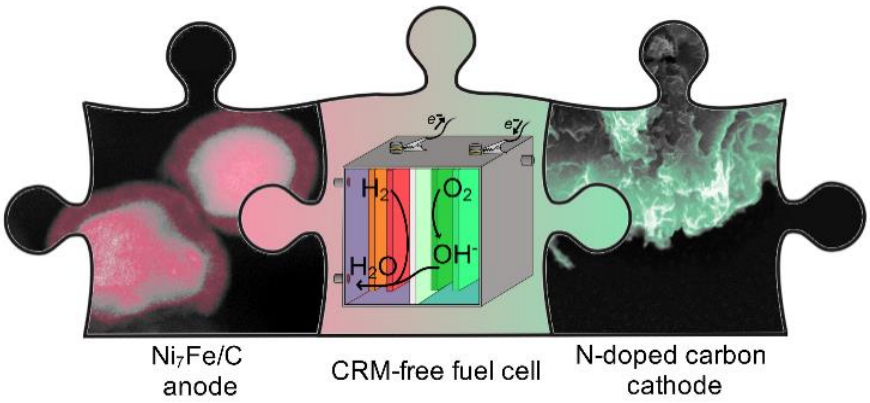

Parts of this chapter have been published as J. Biemolt, J.C. Douglin, R.K. Singh, E.S. Davydova, N. Yan, G. Rothenberg and D.R. Dekel, An Anion-Exchange Membrane Fuel Cell Containing Only Abundant and Affordable Materials, *Energy Technol.* **2021,** 9: 2000909.

Introduction

Sustainable chemistry and sustainable energy are popular buzzwords, yet they require viable technological concepts to become reality. As such, converting hydrogen to electricity using fuel cells is often mentioned as a fossil-free future engine. However, only anion-exchange membrane fuel cells (AEMFCs) can avoid **platinum group metal** (PGM) electrocatalysts, and thus be viable for large-scale application.[1–4] Unlike the proton-exchange membrane fuel cell (PEMFC), AEMFCs operate under alkaline conditions. The combination of the acidic conditions and applied potential in PEMFCs easily dissolve abundant transition metals as their respective cations. Contrarily, the alkaline conditions of AEMFCs generally yield metallic or insoluble hydroxides. This makes AEMFCs suitable for PGM-free catalysts.

Achieving this PGM-free goal, however, is extremely challenging. From all studies showing AEMFC performance data, only 6% are based on platinum-free electrocatalysts and few of those are completely PGM-free.[5,6] This is in stark contrast with the many papers based on the hydrogen oxidation reaction (HOR) and oxygen reduction reaction (ORR) alone. Here, PGM-free catalysts are often reported, yet none use these catalysts in fuel cells. This stems from an overall lack of activity and optimization required in the fuel cell. PGM-free HOR catalysts rarely show high activity and lag far behind PGM-based catalysts. In ORR, sluggish kinetics, higher overpotentials and catalyst stability are the major drawbacks of PGM-free catalysts.

Still, the first to report PGM-free fuel cell performance were Lu *et al.*,[7] who showed in 2008 a Ni-Cr anode and Ag cathode AEMFC with a promising peak power density of 50 mW cm^{-2}. Five years later, two more studies achieved peak

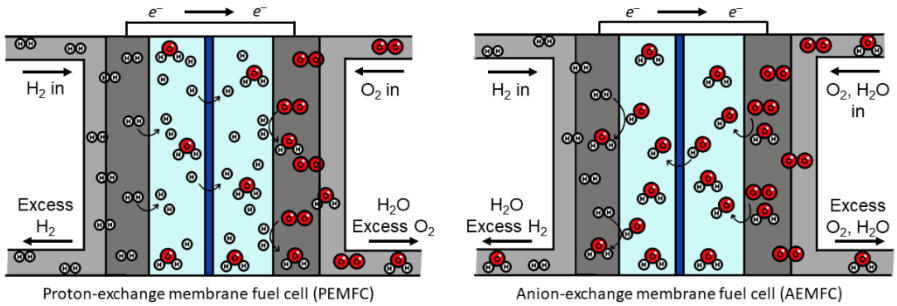

Figure 5.1. *schematic representations of a proton-exchange membrane fuel cell (PEMFC, left) and an anion-exchange membrane fuel cell (AEMFC, right).*

power densities of 76 and 40 mW cm^{-2}, using AEMFCs based on Ni/Ag and NiW/CoPPY-based (anode/cathode) electrocatalysts, respectively.[8,9] Since then, the only report of an AEMFC based on PGM-free electrocatalysts used NiCo/C and Co_3O_4/C, with a peak power density of 22 mW cm^{-2}.[10] While these pioneering studies showed the feasibility of PGM-free electrocatalysts, most still use **critical raw materials** (CRMs) such as cobalt, chromium, and tungsten.[11,12] Critical raw materials are materials of high importance for the economy and have a high risk associated with their supply. These supply risks can range from scarcity, supplier monopolies or geographic locations of the reserves. Considering these factors is highly important as a sudden disruption of supply can paralyze this otherwise sustainable technology. Thus, any large-scale and sustainable deployment of AEMFCs should, ideally, minimise the use of both PGMs and CRMs.[13]

With this in mind, we focused our research on PGM-free and CRM-free electrocatalysts, aiming at demonstrating their feasibility in AEMFC performance tests. The Technion group showed previously that Ni_3Fe-based electrocatalysts are highly active for the HOR in alkaline conditions,[14] and that Ni_3Fe/C HOR electrocatalysts are stable in alkaline media.[15] Elsewhere, we demonstrated the utility of metal-free nitrogen-doped carbon catalysts for the ORR electrodes. In this chapter, we combine a similar Ni_xFe HOR catalyst and the ORR catalyst in a complete fuel cell, presenting an affordable and abundant electrocatalyst system for AEMFCs.

Results and Discussion

For the HOR catalyst, we started from Ni_3Fe/C, which showed a negligible dissolution up to 0.7 V_{RHE}.[15] This catalyst maintained its HOR activity after 1000 cycles to 0.3 V_{RHE}, comparing favourably with Ni_3Mo/C and Ni_3Cu/C.[16,17] We therefore opted for developing nickel-rich NiFe bimetallic HOR electrocatalysts. A nominal Ni_7Fe stoichiometry was chosen to increase the nickel content in the bimetallic nanoparticle, aiming for high HOR activity, while still keeping some iron in the particles for chemical and electrochemical stability. The Ni_7Fe/C anodes were prepared by first mixing the salts of Ni and Fe in a nominal 7:1 molar ratio, followed by wet chemical reduction with sodium borohydride.[14,15] This yields a uniform dispersion of Ni_7Fe/C of size ~10–15 nm. To ensure the high porosity of this catalyst, we used solid ionomeric particles that conduct hydroxide while maintaining the access of oxygen to the catalyst layer.

As the ORR catalyst, we used nitrogen-doped carbon,[18] a family of materials known for their excellent ORR activity in alkaline conditions.[19–22] This material is easily made on a multi-gram scale and can be tailored to specific operating conditions.[23,24] Briefly, the material was prepared by first forming a magnesium-nitrilotriacetic acid metal-organic framework. This was then carbonized, acid washed to remove any MgO and form hierarchical pores, and re-carbonized (see experimental procedures as well as previous chapters).

The Ni/Fe atomic ratio, measured by inductively coupled plasma - atomic emission spectroscopy (ICP-AES), was ca. 8.5, confirming the nickel-rich content. Figure 5.2 shows the physical and chemical characterizations of the Ni_7Fe/C and N-doped carbon electrocatalysts. The scanning transmission electron microscope high-angle annular dark-field imaging (STEM-HAADF) image and the corresponding energy-dispersive X-ray spectroscopy (EDS) elemental maps of Ni_7Fe/C for Ni, Fe, O, and C are shown in Figure 5.2a–e. The particle size of the NiFe alloy is ~10–15 nm, with a fine mixing of the metals. From the single nanoparticle HAADF images, we estimate a uniform oxide layer coating of ~3.6 nm. The oxide content is slightly higher than that reported for Ni_3Fe

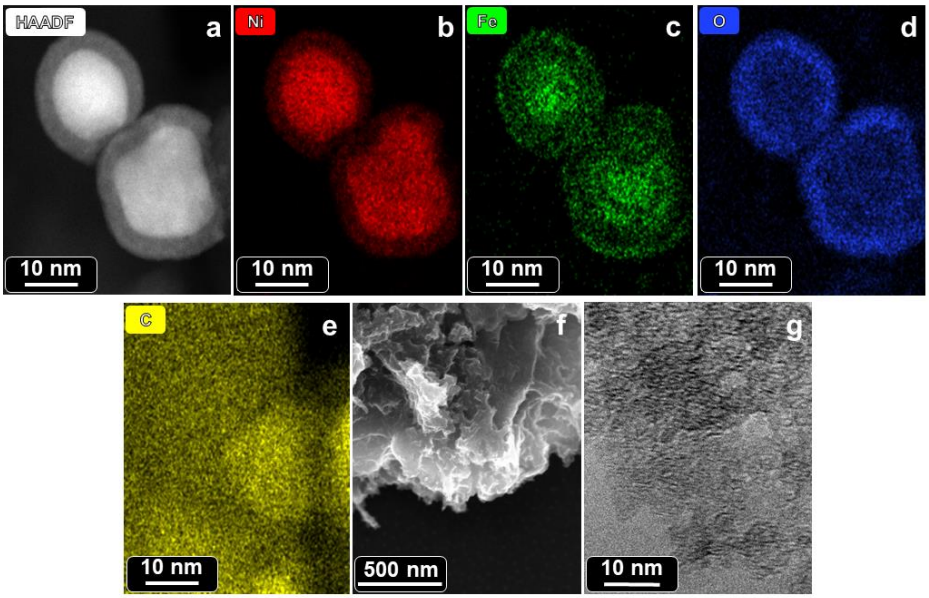

Figure 5.2. *Catalyst characterisation: (a) HAADF image of Ni_7Fe/C; (b–e) STEM-EDS maps of Ni_7Fe/C; (f) SEM of the N-doped carbon; (g) TEM of the N-doped carbon.*

nanoparticles.[14,15] Several studies state that the presence of metal-metal oxide phase is important for alkaline HOR catalysis.[25–27] The core/shell structure shown in the HAADF images also reflects the surface segregation, suggesting that detailed surface analysis, (e.g. by X-ray photoelectron spectroscopy, see below) is useful. Additional morphological data is shown in Figs. 5.3. These observations are supported by cross-analysis using electron energy loss spectroscopy (EELS, see maps and spectra in Figure 5.3). The peak at high energy loss regions at 531 eV, doublet at 708/721 eV, and the doublet at 853/872 eV correspond to O, Fe $L_{2,3}$, and Ni $L_{2,3}$, respectively, due to inner electron transition and suggests that Fe and Ni nanoparticles are at least partially oxidised.[28]

Figure 5.2f shows the SEM image of the N-doped carbon. The flakes are a few microns in diameter, with a macroporous network that enables a fast mass transfer. TEM reveals mesopores within the structure, further expanding the network. The material has a high specific surface area of 1320 m^2g^{-1} and ample pore volume (3.10 cm^3g^{-1} in total, of which 80% comes from mesopores). Its nitrogen content is 4.6 wt%, of which 36% pyridinic, 51% graphitic and 14%

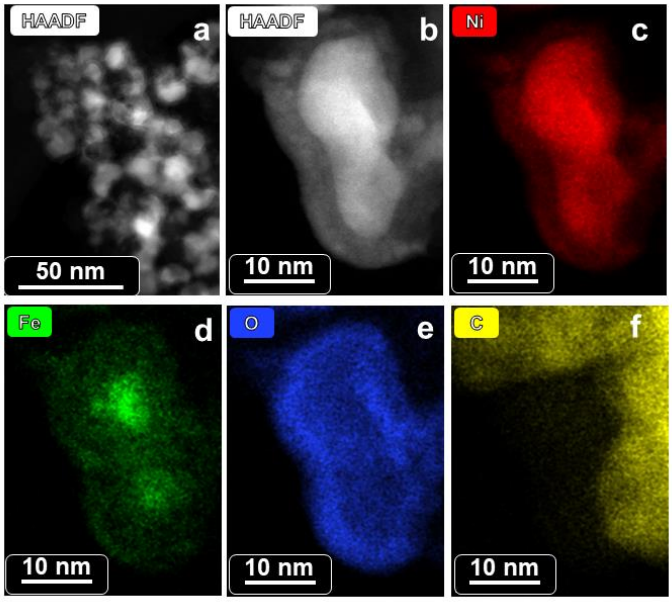

***Figure 5.3**. (a) STEM-HAADF image of the Ni_7Fe/C nanoparticles, (b) High-resolution HAADF image of the Ni_7Fe/C nanoparticles; the corresponding STEM-EDS map of (c) Ni, (d) Fe, (e) O and (f) C.*

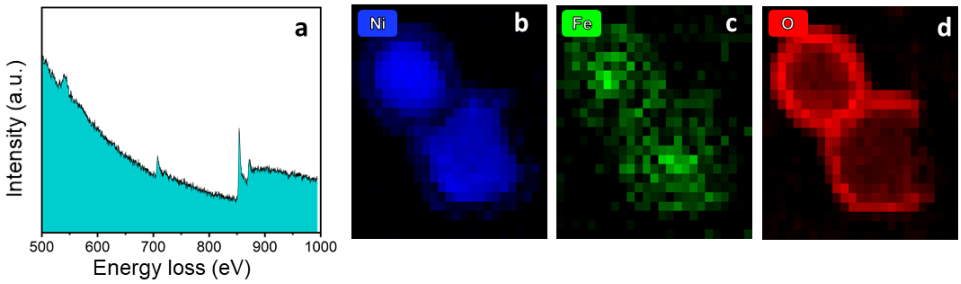

Figure 5.4. *The electron energy loss spectroscopy (EELS) (a) spectrum, (b) Ni map, (c) Fe map and (d) oxygen map for the Ni_7Fe/C electrocatalyst.*

oxidized. A detailed study of the morphology and surface composition of this material is published elsewhere.[18,24]

The X-ray diffraction (XRD) pattern of Ni_7Fe/C, shown in Figure 5.5a, suggests an amorphous phase (similar patterns were reported for Ni_3Fe/C prepared by the same synthesis protocol).[15] We see a dominant peak at 2θ = 45.34°, which is higher than the counterpart of the pure Ni (JCPDS #00-004-0850), Fe (JCPDS #00-006-0696) and Ni-Fe (JCPDS #00-037-0474) phases. This also suggests lattice contraction, in contrast to Ni_3Fe/C, where lattice expansion was observed.[14,15]

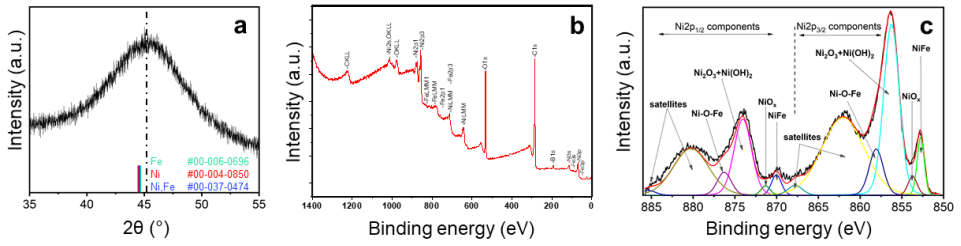

Figure 5.5. *(a) The X-ray diffraction (XRD) pattern of the Ni_7Fe/C electrocatalyst, (b) The X-ray photoelectron spectroscopy (XPS) survey spectrum of the Ni_7Fe/C electrocatalyst. The B1s peak arises from the $NaBH_4$ used in the reduction process forming Ni-B. (c) the X-ray photoelectron spectroscopy (XPS) spectrum on the Ni 2p peak, deconvoluted in its individual components.*

The Ni2p XPS spectrum of Ni_7Fe/C is shown in Figure 5.5c (the full survey spectrum is given Figure 5.5b and Tables 5.1 and 5.2). We see that the Ni:Fe surface atom ratio equals 15.3. The peak at 853.72 eV is at the binding energy close to Ni^0. Since the Ni $2p_{3/2}$ peak position in Ni-Fe alloy is nearly identical to that of Ni^0, this peak relates to a Ni-Fe alloying component.[29] NiO is usually reported at about 854.5 eV, although some references relate this peak to 856.0 eV binding energy.[15] Hence, the peak at 853.72 eV can be attributed to a NiO_x phase, with "x" slightly lower than unity (e.g. NiO with some defects: O-deficiency/vacancies). The peak at 856.2 eV is rather broad as it includes several components. We assign it to Ni_2O_3 + $Ni(OH)_2$. Similarly, the peak at 858.1 eV is assigned to Ni-O-Fe. Elsewhere, the same component was found at a slightly higher binding energy of 858.8 eV.[15] Conversely, $NiFe_2O_4$ gives this peak at about 855.0 eV.[30] Hence, the exact energy position of Ni-O-Fe depends on the composition, $Ni_xFe_yO_z$. Note that the Fe 2p (707, 720 eV doublet) interacts with the Ni LMM structure (706, 712 eV). The Fe concentration is 15 times lower than Ni, perhaps not even as high as C and O. Hence measuring Fe 2p may be challenging. We also see a NiB phase from the XPS spectra of B1s, which is mainly due to the reduction process using $NaBH_4$.[31,32]

We then characterised both the Ni_7Fe/C and N-doped carbon electrocatalysts using rotating disk electrode (RDE) tests (Figure 5.5, see experimental section for details). The HOR polarization curve of Ni_7Fe/C is shown in Figure 5.6a. The corresponding CV in Ar-saturated electrolyte is shown in Figure 5.6b and was integrated in the range of the $Ni(OH)_2$ formation as an in situ method to determine the electrochemically active surface area (ECSA) of Ni with the specific charge density of 514 μC cm^{-2}_{Ni}.[33] The values of exchange current density (i_o) were calculated in the micropolarization potential range applying the equation (5.1)[25,34]

$$i^o = RTi/F\eta \qquad (5.1)$$

where i is the measured current averaged for the range of overpotential values (η) between -5 to 5 mV, T is the temperature of the electrolyte (K), R is gas constant, and F is Faraday constant.

Table 5.1. The atomic % of carbon, oxygen, nickel, iron and boron in the Ni_7Fe/C samples derived from the XPS survey spectrum.

Element	Atomic composition (%)
Carbon (C)	66.96
Oxygen (O)	21.43
Nickel (Ni)	7.48
Iron (Fe)	0.49
Boron (B)[a]	3.65

[a] B is coming from the borohydride reduction process

Table 5.2. Fitting parameters and results of the Ni2p XPS peak of the Ni_7Fe/C electrocatalyst

	Ni-Fe	NiO_x	Ni_2O_3 + $Ni(OH)_2$	Ni-O-Fe	Satellite	Satellite
Ni $2p_{3/2}$	852.75 eV	853.72 eV	856.25 eV	858.07 eV	862.05 eV	867.78 eV
Ni $2p_{1/2}$	870.02 eV	871.32 eV	874.05 eV	876.27 eV	880.25 eV	885.38 eV
Component weight	3.74% (Ni $2p_{3/2}$) 1.86% (Ni $2p_{1/2}$)	1.58% (Ni $2p_{3/2}$) 0.78% (Ni $2p_{1/2}$)	24.18% (Ni $2p_{3/2}$) 12.09% (Ni $2p_{1/2}$)	5.93% (Ni $2p_{3/2}$) 2.96% (Ni $2p_{1/2}$)	29.94% (Ni $2p_{3/2}$) 14.96% (Ni $2p_{1/2}$)	1.32% (Ni $2p_{3/2}$) 0.66% (Ni $2p_{1/2}$)
Total Component weight	5.60%	2.36%	36.27%	8.98%	44.90%	1.98%
Total component weight excluding satellites	10.5%	4.4%	68.3%	16.8%		

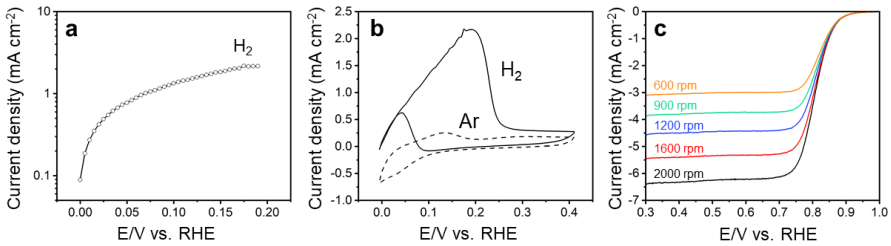

Figure 5.6. *(a) HOR polarization curve of Ni_7Fe/C electrocatalyst, (b) HOR cyclic voltammetry curve for the Ni_7Fe/C electrocatalyst (c) ORR linear sweep voltammetry of the N-doped carbon electrocatalyst. HOR: 1.0 M KOH with 1 mVs^{-1} and 1600 rpm, and ORR: 0.1 M KOH with 10 mVs^{-1}.*

Figure 5.6b shows the HOR CV of Ni_7Fe/C, suggesting a significant increase in current in H_2-saturated solution as compared to CV in an Ar-saturated solution. The specific exchange current ($i_{o,m}$) is calculated by normalizing the i_o by mass of the catalyst. The exchange current density ($j_{o,s}$) is calculated by normalizing i_o to the electrochemical surface area (ECSA) of the Ni (cm^2_{Ni}). The ECSA is calculated by integrating the anodic peak by using the Ni specific charge density of 514 µC cm^{-2}.[14,15,35] These calculations gave a value of 3.90 mA mg^{-1}_{cat}, which is further increased by normalizing with the Ni loading estimated from ICP-AES as 7.9 mA mg^{-1}_{Ni}. The exchange current density ($j_{o,s}$) is estimated to be 0.032 mA cm^{-2}_{Ni}, which is comparable to the Ni-based catalysts reported by Yang *et al.*[25] and higher than the previous reports.[16,17,35–37] Elsewhere, studying analogous Ni-based electrocatalysts, we suggested that the HOR is influenced by both the hydrogen and hydroxide binding energies, and that the HOR activity of Ni_3Fe/C is due to higher OH^-coverage at lower overpotentials.[14] We believe that

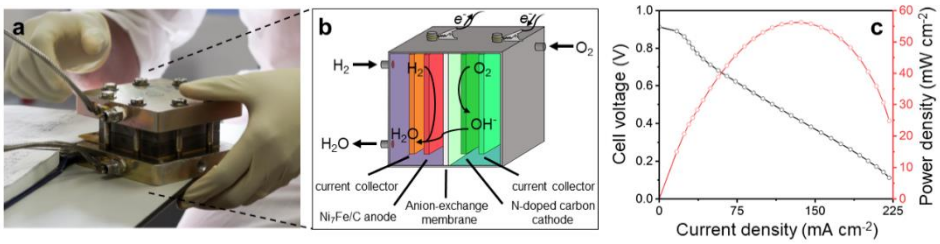

Figure 5.7. *(a) Photo and (b) schematic of the AEMFC setup. (c) Polarization curve of the AEMFC with Ni_7Fe/C anode and N-doped carbon cathode catalysts. T_{cell} = 95 °C, RH of 100%, flow rates of 0.01 lpm of H_2 (2 barg) and 0.2 lpm of O_2 (no back pressure) for anode and cathode, respectively.*

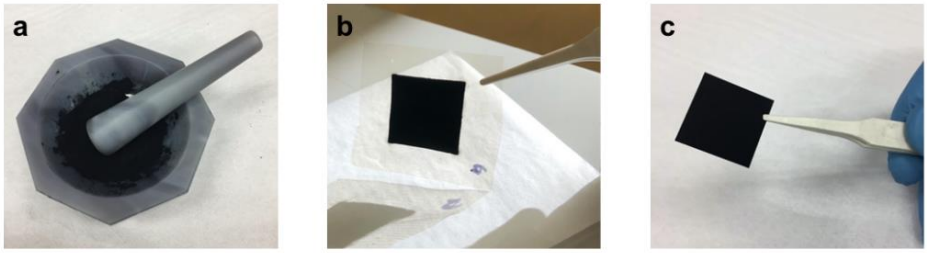

Figure 5.8. *Stages in the preparation of the MEA with a 5 cm² active area: (a) Ionomer and catalyst combined in a mortar and ground with a pestle to create catalyst slurry, (b) Ni_7Fe/C catalyst slurry coated onto anode side of A-201 membrane to create anode CCM loaded to 3.0 $mg_{Ni_7Fe}cm^{-2}$, and (c) N-doped-C catalyst slurry coated onto Toray TGP-H-060 GDL to create cathode GDE loaded to 0.7 $mg_{N\text{-}doped\text{-}C}cm^{-2}$.*

a similar case applies to this Ni_7Fe/C catalyst.

Figure 5.6c shows the linear sweep voltammetry (LSV) curve of the N-doped carbon ORR electrocatalyst measured at different potential is 0.91 V_{RHE} and the halfwave potential is 0.81 V_{RHE}. Previously, we established that the current in this potential range comes from the oxygen reduction reaction, by performing a similar measurement in N_2-saturated electrolyte.[24] The combination of the above-mentioned nitrogen active sites and pore structure also yields a high electron transfer number of 3.64, indicating an almost full reduction of O_2 to H_2O. The corresponding Koutecký-Levich calculations and a table comparing this N-doped carbon to other metal-free ORR catalysts are available elsewhere.[18,24]

Finally, we tested the two electrocatalysts in an AEMFC setup. A 5 cm² electrochemical cell was assembled by pressing a Ni_7Fe/C electrocatalyst-coated membrane anode onto an N-doped carbon electro-catalyst gas diffusion electrode cathode (see photo and schematic in Figure 5.7, as well as electrode preparation photos in Figure 5.8). Figure 5.7c shows the resulting polarization curve of the cell. This cell shows promising performance with a maximum power density of 56 mW cm^{-2} at a current density of 138 mA cm^{-2}. In particular, the cell achieved a limiting current density higher than 200 mA cm^{-2}. This remarkable current density value is the highest reported to date, twice as high as the limiting current densities reported for AEMFCs using non CRM-free electrocatalysts in both the anode and the cathode (see Table 5.3).

Table 5.3. Comparison of the completely PGM-free electrocatalyst AEMFCs in the literature operated with H_2-O_2 depicting where CRM-free electrocatalysts were used in the electrodes.

Anode (AN) catalyst	CRM -free	Cathode (CA) catalyst	CRM -free	AN loading (mg cm^{-2})	CA loading (mg cm^{-2})	Peak power density (mW cm^{-2})	Limiting current density (mA cm^{-2})	Ref
Ni_7Fe /C	**Yes**	**N-doped-C**	**Yes**	**3**	**0.7**	**56**	**224**	**This work**
Ni/C	Yes	Ag	Yes	5	0.5	76	120	[9]
Cr-Ni	No	Ag	Yes	5	1	50	105	[7]
Ni-W	No	Co_{PPy}/C	No	17.5	2	40	120	[8]
NiCo/ C	No	Co_3O_4/C	No	5	3	22	48	[10]

Conclusion

We have built a completely PGM-free and CRM-free anion-exchange membrane fuel cell using Ni_7Fe/C and N-doped carbon electrocatalysts. The cell achieved a maximum power density of 56 mW cm^{-2} at a current density of 138 mA cm^{-2}, which is among the highest value reported to date for CRM-free electrocatalyst systems. We believe that CRM-free fuel cells are the only viable option for a large-scale, long-term and sustainable energy transition. However, such a transition also requires solutions using known concepts and techniques, limiting the need for new production lines and methods. Our electrocatalysts fit these criteria, with straightforward and scalable preparation protocols. As such, we hope that the publication of these results will inspire others in developing sustainable and long-term solutions for the energy transition challenge problems facing our future.

References

[1] B. P. Setzler, Z. Zhuang, J. A. Wittkopf, Y. Yan, Activity targets for nanostructured platinum-group-metal-free catalysts in hydroxide exchange membrane fuel cells, *Nat. Nanotechnol.* **2016**, *11*, 1020–1025.

[2] E. Agel, J. Bouet, J. F. Fauvarque, Characterization and use of anionic membranes for alkaline fuel cells, *J. Power Sources* **2001**, *101*, 267–274.

[3] J. R. Varcoe, P. Atanassov, D. R. Dekel, A. M. Herring, M. A. Hickner, Paul. A. Kohl, A. R. Kucernak, W. E. Mustain, K. Nijmeijer, K. Scott, T. Xu, L. Zhuang, Anion-exchange membranes in electrochemical energy systems, *Energy Env. Sci* **2014**, *7*, 3135–3191.

[4] S. Gottesfeld, D. R. Dekel, M. Page, C. Bae, Y. Yan, P. Zelenay, Y. S. Kim, Anion exchange membrane fuel cells: Current status and remaining challenges, *J. Power Sources* **2018**, *375*, 170–184.

[5] D. R. Dekel, Review of cell performance in anion exchange membrane fuel cells, *J. Power Sources* **2018**, *375*, 158–169.

[6] X. Peng, V. Kashyap, B. Ng, S. Kurungot, L. Wang, J. Varcoe, W. Mustain, High-Performing PGM-Free AEMFC Cathodes from Carbon-Supported Cobalt Ferrite Nanoparticles, *Catalysts* **2019**, *9*, 264.

[7] S. Lu, J. Pan, A. Huang, L. Zhuang, J. Lu, Alkaline polymer electrolyte fuel cells completely free from noble metal catalysts, *Proc. Natl. Acad. Sci. U. S. A.* **2008**, *105*, 20611–20614.

[8] Q. Hu, G. Li, J. Pan, L. Tan, J. Lu, L. Zhuang, Alkaline polymer electrolyte fuel cell with Ni-based anode and Co-based cathode, *Int. J. Hydrog. Energy* **2013**, *38*, 16264–16268.

[9] S. Gu, W. Sheng, R. Cai, S. M. Alia, S. Song, K. O. Jensen, Y. Yan, An efficient Ag–ionomer interface for hydroxide exchange membrane fuel cells, *Chem Commun* **2013**, *49*, 131–133.

[10] V. Men Truong, J. Richard Tolchard, J. Svendby, M. Manikandan, H. A. Miller, S. Sunde, H. Yang, D. R. Dekel, A. Oyarce Barnett, Platinum and Platinum Group Metal-Free Catalysts for Anion Exchange Membrane Fuel Cells, *Energies* **2020**, *13*, 582.

[11] A. Chapman, J. Arendorf, T. Castella, P. Thompson, P. Willis, L. T. Espinoza, S. Klug, E. Wichman, *Study on Critical Raw Materials at EU Level - Final Report*, European Commision, **2013**.

[12] S. M. Fortier, N. T. Nassar, G. W. Lederer, J. Brainard, J. Gambogi, E. A. McCullough, *Draft Critical Mineral List—Summary of Methodology and Background Information—U.S. Geological Survey Technical Input Document in Response to Secretarial Order No. 3359*, U.S. Geological Survey, Reston, VA, **2018**.

[13] T. Asefa, X. Huang, Heteroatom-Doped Carbon Materials for Electrocatalysis, *Chem. - Eur. J.* **2017**, *23*, 10703–10713.

[14] E. Davydova, J. Zaffran, K. Dhaka, M. Toroker, D. Dekel, Hydrogen Oxidation on Ni-Based Electrocatalysts: The Effect of Metal Doping, *Catalysts* **2018**, *8*, 454.

[15] E. S. Davydova, F. D. Speck, M. T. Y. Paul, D. R. Dekel, S. Cherevko, Stability Limits of Ni-Based Hydrogen Oxidation Electrocatalysts for Anion Exchange Membrane Fuel Cells, *ACS Catal.* **2019**, *9*, 6837–6845.

[16] S. Kabir, K. Lemire, K. Artyushkova, A. Roy, M. Odgaard, D. Schlueter, A. Oshchepkov, A. Bonnefont, E. Savinova, D. C. Sabarirajan, P. Mandal, E. J. Crumlin, I. V. Zenyuk, P. Atanassov, A. Serov, Platinum group metal-free NiMo hydrogen oxidation catalysts: high performance and durability in alkaline exchange membrane fuel cells, *J. Mater. Chem. A* **2017**, *5*, 24433–24443.

[17] A. G. Oshchepkov, P. A. Simonov, O. V. Cherstiouk, R. R. Nazmutdinov, D. V. Glukhov, V. I. Zaikovskii, T. Yu. Kardash, R. I. Kvon, A. Bonnefont, A. N. Simonov, V. N. Parmon, E. R. Savinova, On the Effect of Cu on the Activity of Carbon Supported Ni Nanoparticles for Hydrogen Electrode Reactions in Alkaline Medium, *Top. Catal.* **2015**, *58*, 1181–1192.

[18] D. Eisenberg, W. Stroek, N. J. Geels, C. S. Sandu, A. Heller, N. Yan, G. Rothenberg, A Simple Synthesis of an N-Doped Carbon ORR Catalyst: Hierarchical Micro/Meso/Macro Porosity and Graphitic Shells, *Chem. – Eur. J.* **2016**, *22*, 501–505.

[19] J. Zhang, Z. Zhao, Z. Xia, L. Dai, A metal-free bifunctional electrocatalyst for oxygen reduction and oxygen evolution reactions, *Nat. Nanotechnol.* **2015**, *10*, 444–452.

[20] H. Jiang, J. Gu, X. Zheng, M. Liu, X. Qiu, L. Wang, W. Li, Z. Chen, X. Ji, J. Li, Defect-rich and ultrathin N doped carbon nanosheets as advanced trifunctional metal-free electrocatalysts for the ORR, OER and HER, *Energy Environ. Sci.* **2019**, *12*, 322–333.

[21] J. Tang, J. Liu, C. Li, Y. Li, M. O. Tade, S. Dai, Y. Yamauchi, Synthesis of Nitrogen-Doped Mesoporous Carbon Spheres with Extra-Large Pores through Assembly of Diblock Copolymer Micelles, *Angew. Chem. Int. Ed.* **2015**, *54*, 588–593.

[22] D. Guo, R. Shibuya, C. Akiba, S. Saji, T. Kondo, J. Nakamura, Active sites of nitrogen-doped carbon materials for oxygen reduction reaction clarified using model catalysts, *Science* **2016**, *351*, 361–365.

[23] J. Biemolt, G. Rothenberg, N. Yan, Understanding the roles of amorphous domains and oxygen-containing groups of nitrogen-doped carbon in oxygen reduction catalysis: toward superior activity, *Inorg. Chem. Front.* **2020**, *7*, 177–185.

[24] D. Eisenberg, P. Prinsen, N. J. Geels, W. Stroek, N. Yan, B. Hua, J.-L. Luo, G. Rothenberg, The evolution of hierarchical porosity in self-templated nitrogen-doped carbons and its effect on oxygen reduction electrocatalysis, *RSC Adv* **2016**, *6*, 80398–80407.

[25] F. Yang, X. Bao, P. Li, X. Wang, G. Cheng, S. Chen, W. Luo, Boosting Hydrogen Oxidation Activity of Ni in Alkaline Media through Oxygen-Vacancy-Rich CeO_2/Ni Heterostructures, *Angew. Chem. Int. Ed.* **2019**, *58*, 14179–14183.

[26] Y. Yang, X. Sun, G. Han, X. Liu, X. Zhang, Y. Sun, M. Zhang, Z. Cao, Y. Sun, Enhanced Electrocatalytic Hydrogen Oxidation on Ni/NiO/C Derived from a Nickel-Based Metal–Organic Framework, *Angew. Chem. Int. Ed.* **2019**, *58*, 10644–10649.

[27] A. G. Oshchepkov, A. Bonnefont, V. A. Saveleva, V. Papaefthimiou, S. Zafeiratos, S. N. Pronkin, V. N. Parmon, E. R. Savinova, Exploring the Influence of the Nickel Oxide Species on the Kinetics of Hydrogen Electrode Reactions in Alkaline Media, *Top. Catal.* **2016**, *59*, 1319–1331.

[28] R. H. Manso, P. Acharya, S. Deng, C. C. Crane, B. Reinhart, S. Lee, X. Tong, D. Nykypanchuk, J. Zhu, Y. Zhu, L. F. Greenlee, J. Chen, Controlling the 3-D morphology of Ni–Fe-based nanocatalysts for the oxygen evolution reaction, *Nanoscale* **2019**, *11*, 8170–8184.

[29] Y. Nagai, M. Senda, T. Toshima, XPS Investigations of Ni-Fe Alloy and Fe Films, *Jpn. J. Appl. Phys.* **1987**, *26*, L1131.

[30] L. Marchetti, F. Miserque, S. Perrin, M. Pijolat, XPS study of Ni-base alloys oxide films formed in primary conditions of pressurized water reactor, *Surf. Interface Anal.* **2015**, *47*, 632–642.

[31] J. Legrand, S. Gota, M.-J. Guittet, C. Petit, Synthesis and XPS Characterization of Nickel Boride Nanoparticles, *Langmuir* **2002**, *18*, 4131–4137.

[32] Y. Chen, L. Liu, Y. Wang, H. Kim, Preparation of porous PVDF-NiB capsules as catalytic adsorbents for hydrogen generation from sodium borohydride, *Fuel Process. Technol.* **2011**, *92*, 1368–1373.

[33] A. Roy, M. R. Talarposhti, S. J. Normile, I. V Zenyuk, V. De Andrade, K. Artyushkova, A. Serov, P. Atanassov, Nickel–copper supported on a carbon black hydrogen oxidation catalyst integrated into an anion-exchange membrane fuel cell, *Sustain. Energy Fuels* **2018**, *2*, 2268–2275.

[34] J. Durst, A. Siebel, C. Simon, F. Hasché, J. Herranz, H. A. Gasteiger, New insights into the electrochemical hydrogen oxidation and evolution reaction mechanism, *Energy Env. Sci* **2014**, *7*, 2255–2260.

[35] Z. Zhuang, S. A. Giles, J. Zheng, G. R. Jenness, S. Caratzoulas, D. G. Vlachos, Y. Yan, Nickel supported on nitrogen-doped carbon nanotubes as hydrogen oxidation reaction catalyst in alkaline electrolyte, *Nat. Commun.* **2016**, *7*, 10141.

[36] A. Roy, M. R. Talarposhti, S. J. Normile, I. V. Zenyuk, V. De Andrade, K. Artyushkova, A. Serov, P. Atanassov, Nickel–copper supported on a carbon black hydrogen oxidation catalyst integrated into an anion-exchange membrane fuel cell, *Sustain. Energy Fuels* **2018**, *2*, 2268–2275.

[37] W. Sheng, A. P. Bivens, M. Myint, Z. Zhuang, R. V. Forest, Q. Fang, J. G. Chen, Y. Yan, Non-precious metal electrocatalysts with high activity for hydrogen oxidation reaction in alkaline electrolytes, *Energy Env. Sci* **2014**, *7*, 1719–1724.

Experimental

Materials characterization

The inductively coupled plasma-atomic emission spectroscopy (ICP-AES) was performed with high-resolution ICP-OES spectrometer PlasmaQuant PQ9000, Analytik Jena, Germany, to estimate the composition of NiFe. The sample (in 2 replicates) was extracted with boiling Aqua Regia for 2 h in the 100 mL Erlenmyer flask (Pyrex). After cooling, the extract was transferred to a polypropylene flask and filled up to 20 mL with deionized water. The sample was filtered (0.45 μm filter Millex) prior to measurement. For physicochemical characterization of the catalysts, high-resolution transmission electron microscopy (HRTEM) images were obtained on FEI Titan 80-300 kV operated at 200 kV. The Titan is equipped with a monochromator for sub-eV energy resolution (80-300kV), an (image) aberration corrector, a high-resolution energy filter for sub-eV electron energy loss spectra (EELS) and energy-filtered TEM, a high resolution scanning transmission electron microscope (STEM) system, including high-angle annular dark-field imaging (HAADF), energy-dispersive X-ray spectroscopy (EDS) system for local chemical analysis and a 2Kx2K slow-scan CCD. Powders of the catalysts were dispersed in ethanol (2 mg catalyst per 10 ml) in an ultrasonic bath for 30 min and spray-casted on to a Cu grid coated with holey carbon (300 mesh, Agar Scientific), and left to dry on the TEM grids at room temperature for 24 h in a vacuum oven. The particle sizes were measured directly from the STEM images, which were collected at 200 kV. X-ray diffraction (XRD) data were collected using Rigaku Smartlab diffractometer with Cu X-ray source (λ = 0.15406 nm). The diffractograms spectra were recorded on Rigaku at medium resolution parallel beam geometry at a tube current of 150 mA, and a tube voltage of 45 kV in $\theta/2\theta$ scan mode with a scan rate of 1° min^{-1} in 0.01° steps in a range of diffraction angles from 10 to 80°. Phases were identified via matching with the International Centre for Diffraction Data (ICDD) PDF4+ (2017) database and the Inorganic Crystal Structure (ICSD) database. Crystallite sizes of the metallic nanoparticles were estimated using Scherrer's equation. X-ray photoelectron spectroscopy (XPS) measurements were performed in UHV (2.5×10-10 Torr base pressure) using either 5600 Multi-Technique System (PHI, USA) or Axis Ultra DLD (Kratos Analytical). The samples were irradiated with an Al Kα monochromated source (1486.6 eV), and the outcoming electrons were analyzed by a spherical capacitor analyzer using a slit aperture of 0.8 mm. Survey spectra were registered in a wide energy range (0 through 1400 eV) at a low resolution. Pass energy of 160 eV was

used for survey scans. The region scans were conducted at pass energy of 20 eV using a step size of 0.1 eV. Utility multiplex spectra were taken for different peaks in a low energy range window at an intermediate (utility) resolution. Atomic concentration was calculated for all the elements present. AC calculation accuracy was ±2, ±5, ±10 and ±20% for atomic concentrations around 50%, 20%, 5% and 1%, respectively. The measured spectra were analyzed using XPS peak software and a Lorentzian-Gaussian line shape was used for each component. The background is "integrated" with Gaussian-Lorentzian curve shape using 90% Gaussian.

Material synthesis

The bimetallic Ni_7Fe/C carbon-supported electrocatalyst was synthesized via a chemical reduction method at 0 °C, using sodium borohydride as the reducing agent.[15] 100 mg of the VXCMAX22 (Cabot, the BET surface area ca. 1500 m^2g^{-1}) carbon black was suspended in 15 ml of isopropanol (HPLC Plus GC, 99.9%, Sigma-Aldrich) in the ultrasonic bath (XUBA3, Grant Instruments). Then, the carbon suspension was mixed with 25 ml aqueous solutions containing 3.97 mmol (944 mg) of $NiCl_2{\cdot}6H_2O$ (99.3%, Alfa Aesar) and 0.567 mmol (113 mg) of $FeCl_2{\cdot}4H_2O$ (99.95%, Sigma Aldrich). The intended weight ratio of nickel to carbon was 0.7/0.3, whereas the atomic ratio of Ni/Fe was 7/1. The mixture was then cooled down in an ice bath and de-aerated by flowing Ar (99.999%, Maxima). An ice-cold solution containing 621 mg of $NaBH_4$ (99.99%, Sigma Aldrich) in 25 ml of 0.01 M KOH (AR, BioLab) was used as the reducing agent. The reduction of the metal precursors was carried out in a three-neck round bottle flask by dropping $NaBH_4$ solution into the precursors mixture while stirring. The precipitates were separated and rinsed by milli-Q H_2O (18.2 MΩ cm) in a centrifuge (Eppendorf 5804) five times at 10,000 rpm for 10 min and then two times in isopropanol. The sample was placed in the glove box and then dried under the vacuum line while heating in a mantle at ca. 80–90 °C for 1 h. The catalyst was stored and handled in the glove box.

The nitrogen-doped carbon catalyst was synthesized following the published procedure by Eisenberg *et al.*[18] In short, the carbon precursor was prepared by dissolving 120 mmol (22.937 g) nitrilotriacatic acid (99%, Alfa Aesar A11936) in 200 mL DI water. After heating the solution to 85 °C, 120 mmol (11.657 g) basic magnesium carbonate (Mg; 99%, <0.02% Fe, Strem 93-1220) was added, turning the solution yellow after 5 minutes. Then precipitation was

initiated by removing the heat and adding 1500 mL ethanol (97%), which was chilled in an ice-bath for further crystallization. The off-white precursor was collected and carbonized at 900 °C (ramp 5 °C min^{-1}, 1 h dwell time) in an inert (N_2, 99.999%, 150 mL min^{-1}) atmosphere. The MgO-N-doped carbon was washed twice with an aqueous 1000 mL citric acid solution (0.5 M, citric acid monohydrate, 99.5%, Fisher scientific B.V.), washed with 3000 mL DI water and dried at 120 °C overnight. A further graphitization at 1000 °C (ramp 10 °C min^{-1}, 1 h dwell time) in an inert atmosphere (N_2, 99.999%, 150 mL min^{-1}) yields the final N-doped carbon electrocatalyst.

Electrochemical Characterization

For the *ex-situ* HOR electrochemical characterization, the inks of the Ni_7Fe/C electrocatalysts were prepared by dispersing 10 mg of the catalyst in 2 ml of isopropanol/water mixture (3/1 in volume). Nafion suspension (10 wt% in H_2O, ρ=1.05 g ml^{-1}, Sigma Aldrich) was added to the catalyst ink to obtain the Nafion/catalyst weight ratio of 1/4. The suspension was drop-casted on glassy carbon (GC) RDE to form a catalyst layer with the loading of 250 μg_{cat} cm^{-2}. The electrode was dried in the glove box for about 1 h, and then a droplet of hot milli-Q water was applied of the tip of the RDE to avoid direct contact with the air while being mounted on the rotating shaft of the RDE rotator. Electrochemical measurements were carried out at 25 °C in 0.1 M KOH using WaveDriver 20 Bipotentiostat/Galvanostat (Pine Research) in a three-electrode electrochemical cell with separated compartments. A GC electrode (0.196 cm^{-2} geometrical surface area, Pine) embedded in a Teflon tip was used in this study as the working electrode. Hg/HgO/4.2 M KOH was used as the reference electrode, and a Pt foil or wire served as the counter electrode. All the potentials in this work are presented versus reversible hydrogen electrode potential (RHE). Hydrogen gas (99.999%) was used for the HOR experiments, and Ar (99.999%) purity was used as the inert gas. The following electrochemical protocol was elaborated for the catalyst characterization. Before immersing the RDE working electrode into the electrolyte, it was purged with H_2 (flow 0–500 ml min^{-1}) until the open circuit potential had stabilized. The potential was then scanned repeatedly (up to 5 cycles) in the potential range between 0 V and 0.4 V at a sweep rate of 1 mV sec^{-1} while rotating the electrode at an angular velocity of 1600 rpm, from which the HOR kinetics was inferred. Afterward, the gas flow was changed to Ar until the open circuit potential was stabilized, and then the potential was swept in the potential range between 0 V and 0.4 V at a rate of 1 mV sec^{-1}.

For the *ex-situ* ORR electrochemical characterization, the inks of the N-doped carbon electrocatalysts were prepared by suspending 1 mg N-doped carbon in 1 mL ethanol. 10 µL of a Nafion® suspension (D-521 dispersion 5 wt.% in water/isopropanol) was added to the carbon ink and the ink was sonicated overnight to form a homogeneous suspension. The rotating disk electrode (RDE) working electrode tip (glassy carbon disk 0.196 cm^{-2}, pine research) was polished with diamond polishing film before the measurements. The catalyst film was prepared on the working electrode tip by dropcasting 6 × 6 µL catalyst ink and drying between casts (loading of ±0.185 $mg_{N\text{-doped carbon}}cm^{-2}$). The electrochemical experiments were performed in a 3-electrode glass cell, using a Gamry Instruments Reference 600 potentiostat. The experiments were performed in a 0.1 M KOH electrolyte at 25 °C. A graphite rod was used as a counter electrode and a saturated calomel electrode (SCE) was used as a reference electrode, separated from the electrolyte with a luggin capillary. Oxygen was bubbled through the electrolyte for at least 30 minutes and then used as a gas blanket. The electrolyte resistance was measured prior to the experiments and 95% of this value was used in a positive correction factor in an automatic iR drop correction. Before the linear sweep voltammetry experiments, cyclic voltammograms were recorded between 0.3 to 1.0 V vs RHE till no changes were observed. The linear sweep voltammetry was measured between 0.3 to 1.0 V at 2000, 1600, 1200, 900 and 600 rpm with a rate of 10 mV sec^{-1}. Potentials were reported vs RHE by adding 1.006 V (pH = 13) to the measured SCE potential.

Procedure for Fuel Cell Experiments

For in-situ electrochemical characterizations, an operando AEMFC test was carried out. The membrane electrode assembly for the test was prepared by pressing an electrocatalyst coated membrane anode to an electrocatalyst gas diffusion cathode electrode. For the anode, the catalyst ink was prepared by adding 214 µL of Tokuyama AS-4 anion exchange ionomer (AEI) resin to 214 mg of Ni_7Fe/C in a mortar, to arrive at an AEI: catalyst mass ratio of 50:50. 1 mL of Milli-Q®, ultrapure water was added to mixture and ground with a pestle for 3 minutes to ensure proper coating of the AEI onto the catalyst surface (Figure 5.7). Next, 2 mL of ≥ 99.7% Isopropyl alcohol (IPA) was added to the mixture and ground for an additional 10 minutes resulting in a homogeneous catalyst slurry. After grinding, 20 mL of additional IPA was added to the mortar and mixed into the catalyst slurry to reduce the viscosity and ultimately transfer it to a 50 mL LDPE vial. The ink was sonicated for 1 h in an ice-cooled ultrasonic bath and

sprayed onto a square 4 cm x 4 cm piece of Tokuyama A-201 AEM using an Iwata HP-TH Professional Airbrush with 1.5 bar 99.999% N_2 spray pressure. The entire spraying operation was performed in a fume hood under a constant Argon stream without additional heat to prevent oxidation of the metals in the catalyst layer. The active area was sprayed to a metal loading of 3.0 $mg_{NiFe}cm^{-2}$. After spraying, the anode CCM was stored under N_2 atmosphere in a glovebox until time for use.

For the cathode gas diffusion electrode, the catalyst ink was prepared by adding 75 mg of the TMA functionalized Fumatech AEI powder to a mortar and grinding for 3 min. 175 mg of N-doped carbon was added to arrive at an AEI: catalyst mass ratio of 30:70. 1 mL of Milli-Q®, ultrapure water was added to wet the AEI, catalyst mixture after which it was ground with a pestle for 3 minutes to ensure proper coating of the AEI onto the catalyst surface. 2 mL of ≥ 99.7% Isopropyl alcohol (IPA) was added to the mixture and ground for an additional 10 minutes resulting in a homogeneous catalyst slurry. After grinding, 20 mL of additional IPA was added to the mortar and mixed into the catalyst slurry to reduce the viscosity and ultimately transfer it to a 50 mL LDPE vial. The ink was sonicated for 1 hr in an ice-cooled ultrasonic bath and sprayed onto a square 5 cm^2 piece of Toray TGP-H-060 with 5% PTFE wetproofing, GDL using an Iwata HP-TH Professional Airbrush with 1.5 bar 99.999% N_2 spray pressure. The Airbrush was held at a distance of 2-3 cm away and swept side to side across the GDL area to ensure proper coverage. After each spray sequence, the GDL was dried on a hot plate at 160°C for 5 sec until a metal loading of 0.7 $mg_{N\text{-}doped\ carbon}cm^{-2}$ was attained.

The fuel cell was assembled in situ by covering the anode catalyst layer with a 5 cm^2 piece of GDL-CT woven carbon cloth with a stable microporous layer. Before cell testing, the anode CCM was immersed in a solution of 3 mL, aqueous 1 M KOH combined with 20 mg of $NaBH_4$ for 1 hour. The cathode GDE was separately immersed in aqueous 1 M KOH for 1 hour, with the solution changed every 20 minutes. The soaking process ensured complete exchange to hydroxide ions before assembling the fuel cell. After removing the CCM and GDE from their respective solutions, a laboratory cloth was used to remove excess liquid from the active area surfaces. PTFE gaskets of 406 μm and 127 μm thickness were used on the anode and cathode sides of the asymmetrical fuel cell, respectively, to arrive at a calculated pinch value of 40%. The MEA was secured in a 5 cm^2 Scribner Associates fuel cell hardware between two single serpentine graphite flow-fields. During MEA assembly, the fuel and reactant entry and exit ports were closed to

prevent oxidation of the NiFe and (bi)carbonate build-up. The eight bolts were tightened in a cross pattern at room temperature to 4.5 Nm torque. The AEMFC was tested in an 850E Scribner Associates Fuel Cell Test Station at 95°C with 99.999% O_2 fed to the cathode (0.2 slm, 0 barg, dew point 95°C) and 99.999% H_2 (0.1 slm, 2.0 barg, 95°C) fed to the anode.

Summary

Since their invention, printed circuit boards (PCBs) are a staple of our society. Without them, many of our tools cannot function and daily routines come to a grinding halt. A robust manufacturing method supplies these PCBs, but it is complex and wasteful. PCBs start as fully copper laminated boards and most of the waste stems from selectively etching the track. The inherent copper waste from this selective etching is overshadowed by the polymer waste used for the design transfer. This polymer is not included in the final product and is disposed as waste.

To increase the sustainability of the PCB industry, we describe two strategies in **chapter 1**. The low initial cost (low CAPEX) waste treatment strategy is an immediate solution, but requires high operating costs (high OPEX). For this strategy the main pollutants are water-soluble organics. These are difficult to treat with the traditional microbiological treatment and thus need new treatment options. Ideally, this would be a continuous process that immediately converts pollutants in harmless by-products. Checking the boxes of sustainability, we propose the Electro-Fenton process for this waste water treatment problem. This process is based on the electrochemical reduction of oxygen into hydrogen peroxide. However, there is no traditional catalyst for running this reaction with good selectivity and low overpotential. Thus, research in these hydrogen peroxide selective ORR electrodes is necessary.

As the first step in this investigation, we studied a nitrogen-doped carbon ORR catalyst. N-doped carbons consist of two different phases, amorphous and graphitic, with different characteristics. We hypothesized that changing the phase distributions or surface functionalities can promote H_2O_2-selective ORR. In **Chapter 2**, we describe a selective oxidation procedure to both oxidize the carbon surface and selectively remove amorphous N-doped carbon domains (See Figure S1). There is a positive correlation between amorphous N-doped carbon domain removal and the ORR onset potential and electron transfer number. Thus, graphitic N-doped carbon domains are better for ORR. However, this domains favours the full oxygen reduction reaction to H_2O, not the partial

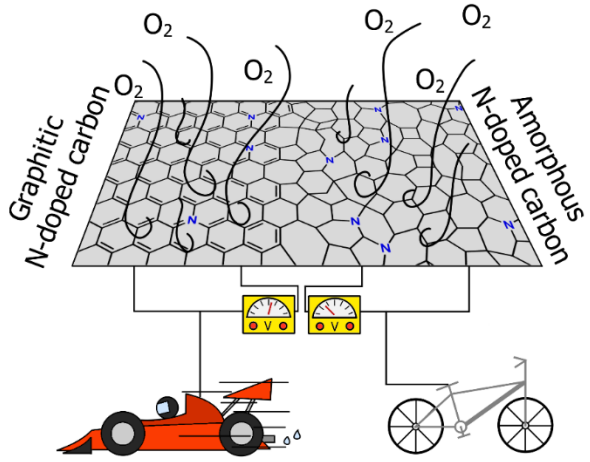

Figure S1. *Graphical abstract of Chapter 2 depicting the two different N-doped carbon domains.*

reduction to H_2O_2. We did see a favourable H_2O_2 selectivity for N-doped carbons with oxygen containing functional groups, which led us to further study N-doped carbons and functional groups.

We then synthesized a new type of mesoporous N-doped carbon in **Chapter 3**. Here the mesoporous would help adsorb organic pollutants, bringing them closer to the surface and ORR active sites (see Figure S2). We found that a combination of an acidic electrolyte, manganese doping and the nitrogen moieties gave high H_2O_2 selectivity. We further used methylene blue as a model pollutant and monitored its adsorption on the mesoporous N-doped carbon. The

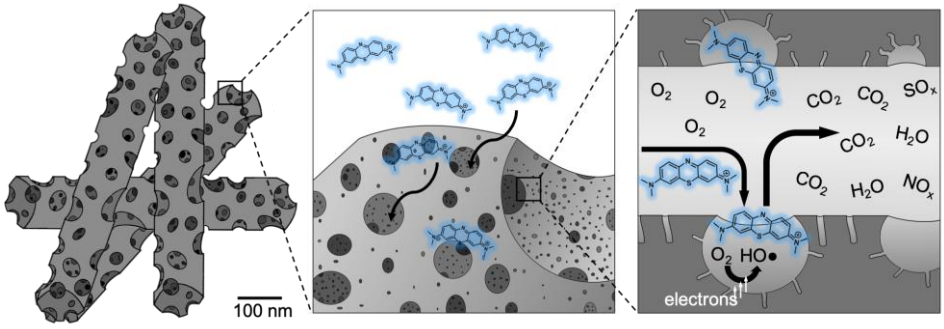

Figure S2. *Graphical abstract of Chapter 3 depicting the adsorption of methylene blue in the mesoporous N-doped carbon and its mineralization via ORR.*

mesopores played a key role in this adsorption as a similar surface area microporous carbon removed less methylene blue. We also demonstrated that methylene blue was removed during ORR operation, via UV-Vis spectroscopy. The two combined chapters show that N-doped carbons are viable catalysts for Electro-Fenton type applications.

The second strategy to minimize the environmental impact of the PCB industry described in chapter 1 is waste prevention. This ideal solution has low operating costs (low OPEX, even saving money on raw materials), but takes an overhaul of the PCB production process (high CAPEX). As the design transfer steps are the most wasteful, replacing the subtractive approach by an additive approach diminish waste. The additive alternative, electroless copper deposition, is a technique that chemically plates copper at places activated by an initiator. This technique is already used in the PCB industry, but has some downsides hindering its application for direct PCB manufacturing. One of these is the costly palladium-based initiator. We opted to minimize the amount of palladium in initiators by developing bimetallic structures with enhanced electronic configurations.

Chapter 4 describes our research into copper and palladium bimetallic structures and the special characteristic at the copper-palladium interface. We developed a simple synthesis for the growth of cuprous oxide and palladium quantum dots, from a native copper nanoparticle. This ensured the formation of

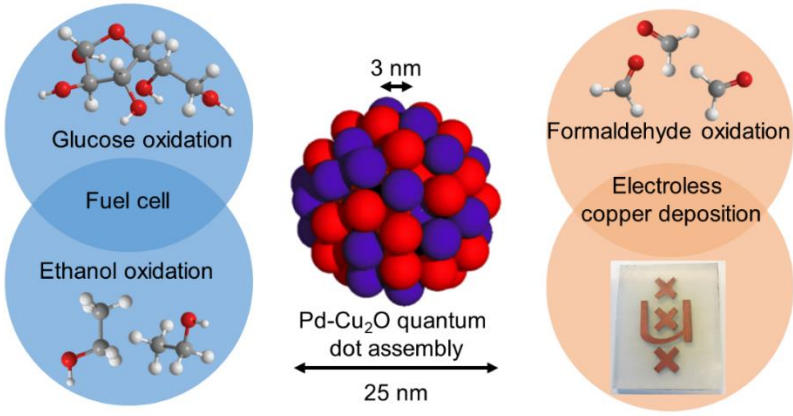

Figure S3. *Graphical abstract of Chapter 4 showing the palladium/cuprous oxide quantum dot assembly and its possible applications.*

a quantum dot assembly (see Figure S3). The assemblies showed excellent electro-oxidation activities of small organics (glucose, ethanol and formaldehyde). Further study of the formaldehyde electrooxidation (the catalytic step in electroless copper deposition) showed an increased activity of the quantum dot assemblies over 'traditional' palladium catalysts. We showed that the cuprous oxide and palladium quantum dot assembly did initiate electroless copper deposition, with deposition rates higher than the 'traditional' palladium catalysts.

Since pollution is much bigger than just the waste from the PCB industry, we stepped back and looked at the bigger picture in **Chapter 5**. In a collaboration with the Technion, Israel Institute for Technology, we combined the two principles of the previous chapters into fuel cell system (See Figure S5). A N-doped carbon was used as the oxygen reduction electrocatalyst, based on our findings in chapter 2 and 3. As the hydrogen oxidation catalyst, a nickel-iron alloy was used, exhibiting some characteristics of bimetallic systems described in chapter 4. In an anion-exchange membrane fuel cell, the combination of the two materials gives a complete platinum-group metal free and critical raw material free system. CRM-free systems are rarely reported, but we believe that they are the only viable option for large-scale operation. The fuel cell reached a maximum power density of 56 mW cm^{-2}, and a limiting current density of 220 mA cm^{-2}. Those results are among the best reported to date for a PGM-free and CRM-free anion-exchange membrane fuel cell.

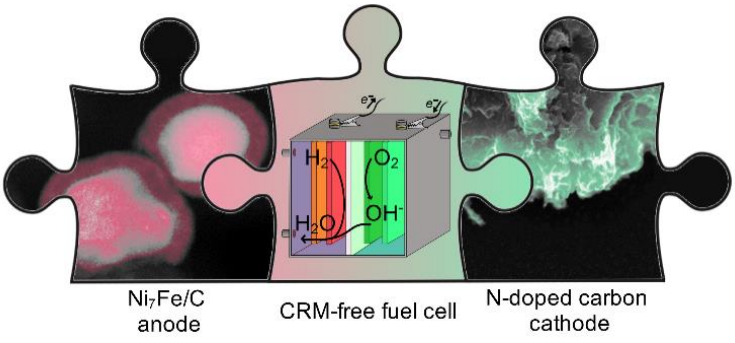

Figure S4. *Graphical abstract of Chapter 5 showing the workings of the anion-exchange fuel cell and the SEM images of the electrode materials.*

Samenvatting

Sinds hun ontdekking hebben printplaten een vast plekje in onze maatschappij. Zonder ze kan veel van ons gereedschap niet werken en komt onze dagelijkse routine tot een stilstand. Een robuuste fabricage methode maakt deze printplaten, maar de methode is complex en verspillend. Printplaten beginnen met een volledige laag koper op de ondergrond en het meeste afval komt van het selectief verwijderen van het ongewilde koper. Het koper afval van dit proces is zelfs overschaduwd door het polymeer afval wat nodig is om het koper patroon over te zetten.

Om de duurzaamheid van de printplaat industrie te verhogen, benoemen wij twee strategieën in **Hoofdstuk 1**. De afval verwerking strategie is een snelle oplossing met lage initiële kosten, maar heeft hoge kosten om te draaien. In deze strategie is het grootste probleem wateroplosbare organische afvalstoffen. Deze kunnen slecht omgezet worden door de traditionele microbiologische procedures en hebben dus nieuwe opties nodig. In de ideale wereld is het nieuwe proces continue en zet gelijk de afvalstoffen omzet in ongevaarlijke moleculen. Wij dragen de duurzame optie van de electrische-Fenton reactie aan als een oplossing voor het afval probleem. Dit proces is gebaseerd op de elektrochemische reductie van zuurstof in waterstof peroxide. Maar, op dit moment zijn er geen traditionele katalysatoren voor deze reactie met een goede selectiviteit voor waterstof peroxide en een lage over potentiaal. Dus, onderzoek naar deze waterstof peroxide ORR elektrodes is hard nodig.

Als de eerste stap in dit onderzoek bestuderen wij een ORR katalysator gebaseerd op stikstof gedoopt koolstof. Stikstof gedoopte koolstoffen bevatten twee verschillende fases, amorf en grafitisch, met elk verschillende eigenschappen. We dachten dat het veranderen van de verhouding tussen deze fases en oppervlakte groepen de waterstof peroxide selectiviteit in ORR kan beïnvloeden. In **Hoofdstuk 2** beschrijven we een selectieve oxidatie procedure om zowel het koolstof oppervlak te oxideren als het amorfe koolstof domein te verwijderen (zie Figuur S1). Er is een positieve correlatie tussen het verwijderen van het amorfe koolstof domein, de ORR onset potentiaal en het aantal

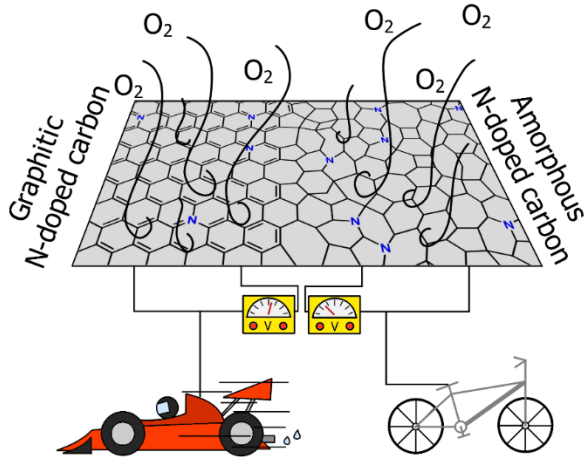

Figuur S1. *Grafische samenvatting van Hoofdstuk 2 wat de twee verschillende stikstof gedoopte koolstof domeinen laat zien.*

elektronen per reactie. Dus de grafitische koolstof domeinen zijn beter voor ORR. Maar dit domain prefereert niet de reductie van zuurstof naar waterstof peroxide maar naar water. We zagen een preferentie voor het maken van waterstof peroxide voor stikstof gedoopte koolstoffen met zuurstof houdende oppervlakte groepen, wat ons aanstuurde tot verder onderzoek naar stikstof gedoopte koolstoffen en hun oppervlakte groepen.

Toen zijn we een nieuw soort mesoporeus stikstof gedoopt koolstof gaan maken in **Hoofdstuk 3**. Hier zouden de mesoporiën helpen met het adsorberen van de organische afvalstoffen, waardoor ze dichterbij het oppervlak komen en daarmee dichter bij de ORR actieve plekken (zie Figuur S2). We ondervonden dat een combinatie van zuur elektrolyt, mangaan doping en de stikstof groepen een goede selectiviteit gaf naar H_2O_2. We gebruikten ook methyleen blauw als een voorbeeld afvalstof en bekeken de opname ervan in de mesoporeuse stikstof gedoopte koolstof. De mesoporiën speelde een belangrijke rol in de adsorptie, sinds een koolstof met een vergelijkbaar oppervlak minder methyleen blauw opnam. We demonstreerde ook dat methyleen blauw werd verwijderd tijdens ORR, via UV-Vis spectroscopie. De twee gecombineerde hoofdstukken laten zien dat stikstof gedoopte koolstoffen rendabele katalysatoren zijn voor electrische-Fenton type applicaties.

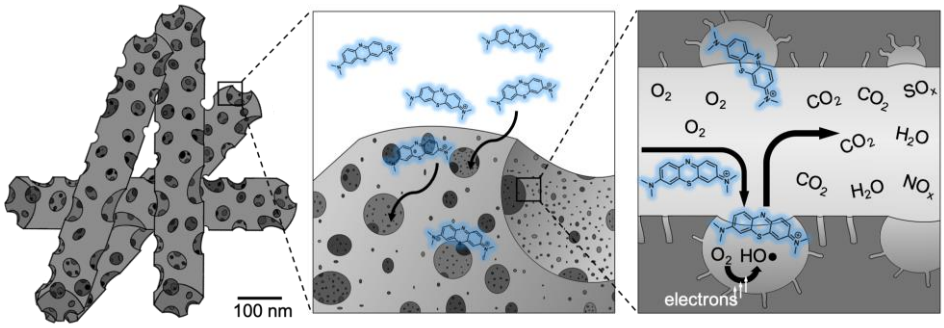

Figuur S2. *Grafische samenvatting van Hoofdstuk 3 wat de adsorptie van methyleen blauw in de mesoporeuse stikstof gedoopte koolstof laat zien en de mineralisatie via ORR.*

De tweede strategie beschreven in Hoofdstuk 1 om de milieu schade van de printplaat industrie te verminderen is afval preventie. Deze ideale oplossing heeft een lage operationele koste (lage OPEX, en bespaart zelfs geld in de vorm van grondstoffen), maar heeft een totale revisie van de printplaat productie proces nodig (hoge CAPEX). Sinds de overdracht van het patroon het meeste afval produceert, is het vervangen van deze subtractieve stappen door additieve stappen een mogelijkheid om de hoeveelheid afval te verminderen. Het additieve alternatief, chemisch verkoperen, is een techniek wat koper afzet op plekken die geactiveerd zijn door een initiator. Deze techniek wordt al gebruikt door de printplaat industrie, maar heeft een paar nadelen voor het direct produceren van printplaten. Een van deze nadelen is het gebruik van een dure palladium initiator. Wij opperden het verminderen van de hoeveelheid palladium in de initiator via het maken van bimetallische structuren met verhoogde elektronische configuratie.

Hoofdstuk 4 beschrijft ons onderzoek naar koper en palladium bimetallische structuren en de speciale eigenschappen op het raakpunt tussen koper en palladium. Wij ontwikkelden een simpele synthese voor het groeien van koper(I)oxide en palladium quantum dots uit een koper nanodeeltje. Dit verzekerde de formatie van een quantum dot assemblage (Zie Figuur S3). Deze assemblages hebben een excellente activiteit voor de elektrische oxidatie van kleine organische moleculen (methanol, glucose en formaldehyde). Verder onderzoek naar de formaldehyde oxidatie (de gekatalyseerde stap van chemisch verkoperen) liet een verhoogde activiteit zien van de quantum dot assemblages

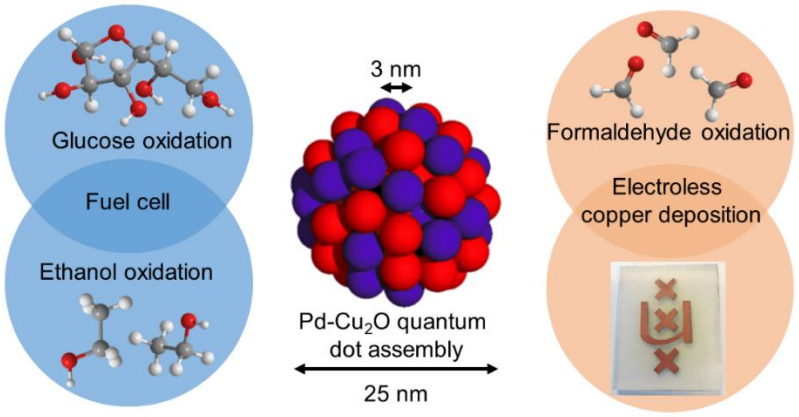

Figuur S3. *Grafische samenvatting van Hoofdstuk 4 met de palladium-koper(I)oxide quantum dot assemblages en de mogelijke applicaties.*

ten opzichte van 'traditionele' palladium katalysatoren. Wij lieten zien dat de koper(I)oxide en palladium quantum dot assemblages ook daadwerkelijk chemisch verkoperen initiëren, met afzet snelheden hoger dan de 'traditionele' palladium katalysatoren.

Omdat vervuiling veel groter is dan de het afval van de printplaat industrie, namen we een stap terug en bekeken het grotere geheel in **Hoofdstuk 5**. In een samenwerking met het Technion, Israel Institure for technology, combineerden we de twee principes van de eerdere hoofdstukken in een brandstofcel (Zie Figuur S4). Een stikstof gedoopte koolstof was gebruikt als de zuurstof reductie katalysator, gebaseerd op onze bevindingen in Hoofdstuk 2 & 3. Een nikkelijzer legering werd gebruikt als de waterstof katalysator, wat karaktertrekken heeft van de bimetallische systemen beschreven in Hoofdstuk 4. De combinatie van de twee materialen geeft een platina groep vrij en kritische grondstof vrij anion uitwisselend membraan brandstofcel. Kritische grondstofvrije systemen worden nauwelijks gerapporteerd, maar wij geloven dat dit de enige optie is voor grootschalige inzet. De brandstofcel haalde een maximale vermogensdichtheid van 56 mW cm^{-2} en een limiterende spanningsdichtheid van 220 mA cm^{-2}. Deze resultaten zijn rondom de beste tot nu toe gerapporteerd voor platina groep vrije en kritische grondstof vrije anion uitwisselend membraan brandstofcel.

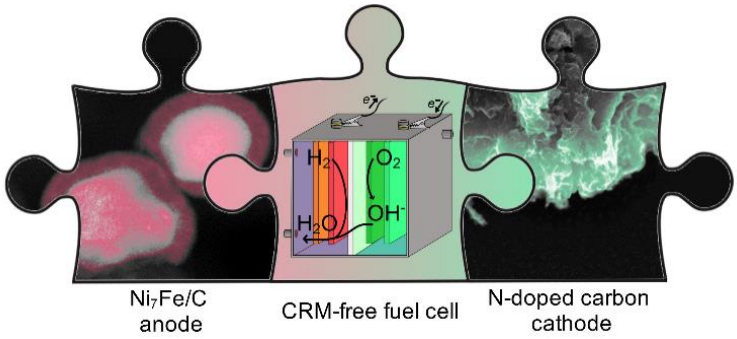

Figuur S4. *Grafische samenvatting van Hoofdstuk 5 met de werking van de anion uitwisselend membraan brandstofcel en de SEM foto's van de elektrode materialen.*

List of Publications

1. Metal-Free One-Pot α-Carboxylation of Primary Alcohols. **Org. Biomol. Chem.** DOI: 10.1039/C6OB01813K.
2. Boosting the Supercapacitance of Nitrogen-Doped Carbon by Tuning Surface Functionalities. **ChemSusChem** DOI: 0.1002/cssc.201700902
3. Advances in Palladium-Catalyzed Cascade Cyclizations. **Adv. Synth. Catal**. DOI: 10.1002/adsc.201800526
4. Efficient Oxygen Reduction to H_2O_2 in Highly Porous Manganese and Nitrogen Co-Doped Carbon Nanorods Enabling Electro-Degradation of Bulk Organics. **Carbon** DOI: 10.1016/j.carbon.2019.09.034
5. Understanding the Roles of Amorphous Domains and Oxygen-Containing Groups of Nitrogen-Doped Carbon in Oxygen Reduction Catalysis: Toward Superior Activity. **Inorg. Chem. Front**. DOI: 10.1039/C9QI00983C
6. Beyond Lithium-Based Batteries. **Materials**, DOI: 10.3390/ma13020425
7. Assembling Palladium and Cuprous Oxide Nanoclusters into Single Quantum Dots for the Electrocatalytic Oxidation of Formaldehyde, Ethanol, and Glucose. **ACS Appl. Nano Mater.** DOI: 10.1021/acsanm.0c02162
8. Nano-Garden Cultivation" for Electrocatalysis: Controlled Synthesis of Nature-Inspired Hierarchical Nanostructures. **J. Mater. Chem. A** DOI: 10.1039/D0TA00870B
9. An Anion-Exchange Membrane Fuel Cell Containing Only Abundant and Affordable Materials. **Ener. Tech.** DOI: 10.1002/ente.202000909
10. A membrane-free flow electrolyzer operating at high current density using earth-abundant catalysts for water splitting. **Nat. Commun.** DOI: 10.1038/s41467-021-24284-5

11. A High-Temperature Anion-Exchange Membrane Fuel Cell with a Critical Raw Material-free Cathode. **Chem. Eng. J. Adv.** DOI: 10.1016/j.ceja.2021.100153

Authors' contributions

Chapter 1. The Tools that Define Us and the Need for Sustainability	
J. Biemolt	Written the text
G. Rothenberg	Revised the text and suggested additional content
N. Yan	Revised the text and suggested additional content

Chapter 2. Treating Organic Pollutants – Influence of Nitrogen-Doped Carbon Morphology and Surface on ORR	
J. Biemolt	Performed the experiments, written the manuscript
G. Rothenberg	Revised the text, suggested additional content (both experimentally and written)
N. Yan	Revised the text, suggested additional content (both experimentally and written)

Chapter 3. Treating Organic Pollutants – Electrochemical H_2O_2 Generation via a Nitrogen-Doped Carbon	
J. Biemolt	Performed the experiments, written the manuscript
K. van der Veen	Performed initial experiments where research was based on
N.J. Geels	Performed Nitrogen adsorption experiments and provided expertise within this area
G. Rothenberg	Revised the text, suggested additional content (both experimentally and written)
N. Yan	Revised the text, suggested additional content (both experimentally and written)

Chapter 4. Waste Prevention – a Palladium and Cuprous Oxide Nanocluster Assembly for Electroless Copper Deposition	
J. Biemolt	Devised experimental plan, performed eQCM experiments (10% of experimental work), written the manuscript

D. van Noordenne	Material synthesis (30% of the experimental work)
J. Lui	Performed DFT caluclations
E. Antonetti	performed experiments formaldehyde oxidation (30% of the experimental work)
M. Leconte	performed experiments ethanol and glucose oxidation (30% of the experimental work)
S. van Vliet	Performed XPS measurements and provided expertise within this area
R. Bliem	Performed XPS measurements and provided expertise within this area
G. Rothenberg	Revised the text, suggested additional content (both experimentally and written)
X.-Z Fu	Provided expertise for DFT
N. Yan	Revised the text, suggested additional content (both experimentally and written)

Chapter 5. An Anion-Exchange Membrane Fuel Cell Containing Only Abundant and Affordable Materials

J. Biemolt	Prepared and performed experiments on the N-doped carbon catalyst, co-written manuscript
J.C. Douglin	Prepared and performed experiments on the NiFe catalyst and the fuel cell, co-written manuscript
R.K. Singh	Prepared and performed experiments on the NiFe catalyst and the fuel cell
E.S. Davydova	Initial experiments for the NiFe catalyst
N. Yan	Revised the text, suggested additional content (both experimentally and written)
G. Rothenberg	Revised the text, suggested additional content (both experimentally and written)
D.R. Dekel	Revised the text, suggested additional content (both experimentally and written)

Acknowledgements

So this is it. Spending four years on research and finishing, writing this very last section after sending the thesis for approval to the promotors a mere few minutes ago. What a time. In a sense, the PhD already feels like an entire lifetime. The stress, the joy, the difficult moments and the families you build along the way. This is difficult about academia as after growing a bond, goodbyes are often within a year. Saying these goodbyes is really not my strong suit. Still, I am grateful for everyone that joined me along this journey, that included the two darkest years of my life. Many of the people below carried me along the way, when my own foundation crumbled down. This is the first thank you to all of you, the first out of many.

First of all, I thank my promoters. **Gadi**, it all started with a MSc project, where you connected me with David and electrochemistry. In the past years, there are many thing I directly and indirectly learned from you. Every so often I find myself giving feedback to peers which you gave me years ago. Thank you for all your help and the opportunity. **Ning**, we did not have so much contact during my Master's, but you still had enough confidence to hire me as your first PhD student. While we did not always see eye to eye, your thought processes and scientific ideas helped build this thesis. I hope that as a first PhD student, I achieved what you were hoping for. Thank you very much for the opportunity and supervision.

Another important group to thank is my thesis committee. **Prof. Bob van der Zwaan, Prof. Bas de Bruin, prof. Sander Woutersen, Prof. Jan van Maarseveen, Prof. Xian-Zhu Fu** and **Prof. Evgeny Pidko**. Some of you have taught me different fundamental aspects of chemistry in my Bachelor or Masters. Others, I have seen regularly on conferences or even collaborated with. Thank you all for your time reading this thesis and your support during the defense.

Amanda, you joined the group in the final stages of my PhD. Still, there were many moments that you taught me about electrochemistry. I see in you a determination to achieve great things, a motivation that inspired me in the final year. Thank you for all the scientific discussions.

While not part of my PhD, there are two people that helped me in gaining this PhD. **Gydo**, in my second year of the bachelor you taught me the practical course for organic chemistry. You never got rid of me, with me joining you for a second year bachelor project, my main bachelor project and a master project. Thank you for lighting the 'PhD flame' in me and teaching me the importance of music on the lab. **David**, as my master thesis supervisor, you taught me many things about science. You helped me with a first co-author paper and helped me understand how the scientific community worked. You also helped me with my foundation in electrochemistry. Thank you for the fun and inspirational time during the project.

Roland, Stefan, John, Ramesh, Elena, Dario and **Jianwen**. Every single one of you helped with parts of this thesis. When I started, collaboration was not a big focus in my PhD, but all of you showed its importance. Even now, I still collaborate with some of you, with amazing results and papers. Thank you all for the hard work and time you put in the projects.

Nothing can be achieved without some very important members of a research group. Technician might even be the wrong word, mentors and councilors might actually be closer. **Marjo** every single time you speak about adsorption, I am amazed of how little I know about it. You are a strong scientist and a woman who stood strong in a male dominated environment. You have all my respect and my deepest gratitude. **Paul**, you helped me with many of the small problems in the lab. I also enjoyed our conversations outside of science, although work related. The stories about your holidays, from your past or when you just returned from them, and discussions about the world brought many new perspectives. Thank you so much. Lastly, **Norbert**, there are so many times you helped me. Building equipment, doing certain experiments, ordering strange items on my behalf. I can extend this list so far, that it would be a thesis on its own. More importantly, you helped me on a personal level. In stressful moments, you would listen to what I had to say and share your own stories. Everything you told about Nora, Dana, Pelle and Quirine always gave a feeling of joy and that things can be good. Thank you so much for this, it is something I will forever carry with me.

No research group is complete without some experienced Post-Docs, which have one of the toughest jobs. **Kamilla**, you started around the time I finished my Master project and were there in the first few months of my PhD. We often had to share equipment, which luckily worked out in the end. Thank you for the scientific talks and the fun moments during breaks. **Sang-Ho**, I still remembered the first day you walked in and got to know the directness of our group. You were someone that I could often discuss ideas with. From these discussion, I felt a bond. I hope all your dreams are coming true, our 'one-shot wonder' basketball player. **Sheetal**, in a sense you were my first direct colleague. The first person I had to suddenly share my 'own' electrochemical equipment with. Never change and continue chasing what you desire. **Layla**, we met when I was asked to go lunch with you and a few others, to see if you were a fit for our group. You immediately showed your energy (although you later admitted that you were very tired that day), which was a perfect fit. I enjoyed some of the passionate discussion during breaks, where you were not afraid to hide your opinion. Thank you. **Ishan**, I still remember the presentation you gave in a group meeting before you joined. I did almost forgot about it, when suddenly I was informed that you were about to join the group, I think almost a year later. Our discussions could go on endlessly and your enthusiasm for science could fill hours. Thank you very much for these moments and the times you shared food with us. **Johan**, I enjoyed the small moment and the coffee breaks. The plants you brought to the office and the scientific talks we shared. Thank you.

Then we have all my fellow PhD students, the people you share blood, sweat and tears with. **Yuan**, I still remember the early mornings, arriving in a well-lit seemingly empty office. Then suddenly your head popped up from behind the computer screen, giving me a small scare and a good laugh. I was honored when you asked me to be your paranymph, although I can say your other paranymph did a much better job than me. Thank you and I hope you found the happiness you deserves. **Wei**, I always felt like you were willing to talk, but were stopped by the language barrier. I have a deep respect for everything you achieved and tried to achieve. Your accomplishments while I was just starting my PhD pushed me forward. Thank you for the few moments we shared and I hope you reach your goal of becoming a professor. **Yiwen**, we did not talk often and I never got a good grasp on your personality. After you left, I learned more

about what kind of person you are. You are a great person, never let someone tell you otherwise. I wish you all the best. **Andreea**, our friendship has been a time of ups and downs. I saw you stress about the PhD, but also your determination to continue forward. I enjoyed the time at breaks, barbeques and borrels, some of the evenings we worked till late and your willingness to do activities outside of work. Thank you for our few trips, such as walking through Flevopark in the snow or going to Tessel. **Maria**, you started the PhD when I was finishing my Masters. You were always a happy note in the group, bringing positive energy. Although sometimes this was a bit quenched by the many problems with the six-flow. You were someone that brought the group together, something that is so important. Thank you for the times I could discuss some of my difficulties. **Thierry**, we were always able to discuss the strangest questions in science and research. Your different view always intellectually challenged me. You 3d printed many lab supplies and even setups (cough, cough, bubblecounter), which helped many people in the group. Your legacy remains in the HCSC group and thank you for the many moments you took the time to help people out. **Ilse**, the person I met even before the Bachelor. We spent a long time together, survived the Bachelor and Master together. Although you always were a bit faster, finishing both the Master and PhD before me. I always enjoyed your outlook to research, which is vastly different then my own and many others. This is something good, just believe in yourself, how others do and achieve things is not important. Thank you for the best moments you gave me, I still treasure those. **Eric**, we started the PhD around the same time, giving me someone that went through the same hardship at the same time. Your stories about your different hobbies are legendary and trips. Although those hobbies did make helping you move more difficult, with the amount of boxes filled with attributes for your hobbies. Thanks for the many good talks, both about adventures and science. **Pieter**, my first true colleague, being another PhD student hired by Ning. How many times did we sit together discussing the difficulties of our projects, different directions we can take and how to make a good research plan. You also became a bridge to many other people at the first floor, with whom I started to create bonds with. You are a great scientist and we will definitely see each other in a few years at your defense. Thank you for all the support and the new things you brought. **Connor**, the vegan British Master student, a honorary title you

had to share with Nathan for a while. You evolved into the vegan British PhD student, the first of Amanda's line. I have seen you grow and make your own way. I still miss the times you joined the D&D sessions, bringing a complete different view on the game than the others in the group. Stay true to yourself, even if the occasional vegan or Brexit joke comes along. You are a genuine good person, with a big heart. Thank you for the interesting discussions, life questions and many laughs we shared. **Martijn**, I enjoyed our conversations about your adventures and your new views on life. We both aspired to become better versions of ourselves, although both for different reasons. Don't ever give up, you are way better than you think. Having discussions with a PhDer in his last year is difficult, but believe me I made more dumb mistakes in my first two years of the PhD. Thank you very much for everything. **Fran**, we met when you did your master project, shaking the autoclaves for materials we will never mention again. You were one of the first people that I was able to be fully open with. I could share things that I did not dare to share with that many people. Luckily, you were also always up to go out for some drinks, pool or bowling. You are a true friend and emphatic person, never lose that quality. Thank you very much for dragging me through some of my harsher times. **Pim**, although you only joined in my final year, I felt we connected scientifically. Maybe it's because we both worked with Eelco Ruijter and did some organic chemistry. Thank you for grounding me while I was the senior PhDer on the lab, telling me that some of my idea were shit. **Zheng-Wei**, the entire Corona work schedule and the fact you only partially worked in our group did not help us getting to know each other. But I still got a vibe from you that you are a great person. Try to open up to the members of our group, they can be great friends. Thank you for every smile and wave when we passed each other in the corridors, not many people take their time for these minor but important interactions. **Noë**, where to begin. You were put under my supervision to start a small project, as practice for a small project before your main project started. And what a horrible few small projects I choose for you. I am so sorry for the kilometers you had to make between the UV-Vis and the potentiostat. I enjoyed the many talks about the scouts, the activities you wanted to do with the kids and the late night shifts we worked together. Your new PhD with Ning and Avantium will work out great, I am sure of that. Thank you for all the good moments.

Of course as a PhD student, there is a small army of bachelor and master students that helped me with this thesis. These sometimes hidden people all had a crucial role to play. **Jeen**, as my first student, you had a rough time. I thought of a project, that seemed doomed from the get go. Still you showed a level beyond an average bachelor student and even laid the foundation for the projects of several master students. You even returned later as a Master student, showing that I failed to scare you off. Thank you for your trust in me. **Tess**, we worked together on your literature thesis. You showed me how well you have to prepare a literature study before you start writing. Our weekly meetings might have felt like a chore, but I do feel that we put a nice study together. Thank you for your hard work. **Yi-An**, I can still remember that you were shocked to find out that your supervisor was younger then you. Don't ever falter, keep that chin up, you can do it. Thank you for all the experience in supervising you brought me. **Dylan**, you continued on Jeen's findings and you were the first student that truly started working on my PhD project. Though job, as the PhDer will thus focus even more on you. You made so many catalysts that we later had to use other master students to fully characterize and test everything. You are also part of the D&D group, a group of friends. Although you are sometimes the more silent person, it is not the same if you are not there. Your PhD in Delft is a perfect fit for you and I felt a bit proud when I heard you were hired there. Thank you for all the work, the laughs and the discussions as a fellow DM. **Rianne and Jelle**, as my first group of one month students, you also were a learning experience for me. Thank you for all your patience with me. **Peter**, after a project with Ilse, you continued the literature study of Tess. A difficult task in which you had to update and improve upon something that was already written. Still you did a great job and our combined efforts yielded a nice review. We also stayed in contact outside of the university, with your characters with the strangest backgrounds always being a joy to behold during the D&D sessions. You are also still connected to Dylan, joining him in Delft for a PhD. Never split the twins. Still you are a great individual, and while we sometimes make jokes at your expense, you take them like a champ. Thank you for all the great moments and now please roll for initiative. **Manon**, you joined my project to finish part of Dylan's work. I hope you enjoyed your time here in Amsterdam, although it was a bit short. Thank you for all the work you did. **Elise**, you also continued the work of Dylan,

and did arguably the most important part of that work. Thank you for all your time. **Emma and Casper**, first of all I have to apologize. The two of you started a few months after my darkest moments started. I think that the both of you can do some amazing work in science, especially since the both of you did so much work in the project. Thank you, and again sorry. **Sem**, as my last student, you had both the blessing and the curse of working under a last year PhD student. There were so many things that I wanted to teach you, so many things I learned over the years. I enjoyed the frequent talks we could have, even the small talks about little things such as our weekends or the plans for them. I hope you can find a PhD somewhere, you have shown me that you are ready for one. Thank you for being you and for being the greatest last student a PhDer can hope for.

There are also a few students that I co-supervised. These students did not directly contribute to this thesis but contributed to my personal growth. **Duane**, not even sure if I can say I supervised you. Noë was the main person here, before Fran took the both of you over. Still, you can be a bright student. Thank you for all the insights. **Jeffrey**, during your interview I felt your connection with science. No wonder thus that you were able to start in our group. Your stories about Akzo are amazing. You asked me if you are good for a PhD, I answered that I had to see a bit more of you. Now I know, you can definitely do a PhD. Thank you for the conversations. **Emma**, the conversations that we had put me on the path to recovery. How many insights you gave me, how to handle feelings and how to convey them. Although I am a closed person, I immediately felt a connection and a freedom to share my inner demons. I am not sure how you do this, but more people see the same qualities in you. You made me realize why writing this acknowledgement section is so difficult, it is a goodbye to a home I found after losing my home. There are not enough words to thank you for everything you have done for me.

Some indirect colleagues also made the time during the PhD more fun. **Xander, Felix, Eva, Pim, Marie, Lotte, Wojciech, Tom, Johan, Zohar, Sander** and **Lukas**, the awesome people for homogeneous catalysis. Some of you took me into the group at Schiermonnikoog, while I was alone at the CAIA course. Others I know from my Bachelor or Master. Thank you all for the fun discussions, talks and moments. **Lars**, my main contact of the 'new' Flowchem group. Get

your own CO_2 cylinder, stop stealing ours and come by more often for a friendly talk. **Tristan**, bit of a strange place to put you here but no time like the present to discuss the newest member of the D&D group. Thanks for joining the group and keeping up with a group that already knew each other before hand.

Last but not least I have to thank my **family**. The people that stay with you no matter what. Als ik jullie allemaal afzonderlijk zou moeten benoemen en hoeveel jullie voor me betekenen zou dit dankwoord in lengte verdubbelen (en het is al zo lang). Daarom moet het maar even kleiner, jullie weten hopelijk allemaal hoeveel jullie voor me betekenen, ook al heb ik soms moeite om contact met jullie op te nemen. Dank jullie allemaal voor de steun en de lessen die jullie me hebben geleerd door het leven. Still there are three that require to be taken out. **Sander**, as my little brother, you always felt like you were in my shadow. It makes me chuckle just thinking about it, as I always felt like I was in yours. Your ability to connect with people, lead them and have a fun time with them is something that inspires me. Your headstrong motivation to do things your own way is something I believe in. Whatever happens, I know you will find your own way through life. No questions asked. Thank you for the amazing childhood and the things we shared together. **Mom and Dad**, to keep it equal I will address the both of you at the same time. You are the people that shaped the best parts of me. You supported me… you inspired me. There are so many good attributes that I inherited from the both of you. I know the often say the curse of the Biemolt or the de Jager family, but there are so many good things the both of you gave me. I know you both are scared sometimes, thinking back about situations of mine and Sander's childhood. Both of us have achieved so many things, so you can't say something went wrong with your parental skills. While writing this I feel at a loss of words to express my gratitude towards you. The amount of times I could fall back onto the both of you, the amount of times you pulled me up when I was down. Thank you so much, and I will try and keep thanking you throughout my life.

Now with a heavy heart I write this final paragraph. Thank you very much dear reader, the fact that you read this paragraph means a lot to me. Like I said, I am bad with goodbyes and things that are ending. I want to say I final thank you to all these people and the many more people that I

did not name here, but met during my PhD. Everyone, no matter how small, helped me become the person that I am today. This also accumulates in this inspiring personal quote that I want to share with you, although it might be controversial. 'I am not proud of all of the choices I have made in my life, but I am proud of the person I am. I am not ashamed of who I am.' (Monica Lewinsky – Interview with John Oliver 2019). I think everyone should remember this quote, as it is something important to be able to say about yourself. Making mistakes is easy, living with them is the hard part. I also spoke a few times in this acknowledgements about the dark two years during the PhD. It is always darkest before the light. But that time was filled with great people, so many lights, so many bonds and so many friends. Instead of this being a goodbye, I invite everyone willing to join me, as I make sail for the dawn 'till the darkness has gone.

Thank you all